INGENIUS
Revista de Ciencia y Tecnología

INGENIUS

José Trinidad Holguín Momaca, MSc, Centro de Investigación en Materiales Avanzados, México.

Juan Manuel Alvarado Orozco, PhD, Centro de Ingeniería y Desarrollo Industrial, México.

Arnaldo Jélvez Caamaño, PhD, Universidad del BIOBIO, Chile.

Javier Murillo, PhD, Centro Internacional Franco Argentino de Ciencias de la Información y de Sistemas, Argentina.

Lucas Daniel Terissi, PhD, Universidad Nacional de Rosario, Argentina.

Rene Vinicio Sanchez Loja, MSc, Universidad Politécnica Salesiana, Ecuador.

Freddy Leonardo Bueno Palomeque, MSc, Universidad Politécnica Salesiana, Ecuador.

Diego Cabrera Mendieta, MSc, Universidad Politécnica Salesiana, Ecuador.

Edwuin Jesus Carrasquero, PhD, Universidad Técnica de Machala, Ecuador.

Carlos Mauricio Carrillo Rosero, MSc, Universidad Técnica de Ambato, Ecuador.

Diego Carrion Galarza, MSc, Universidad Politécnica Salesiana, Ecuador.

Carmen Celi Sanchez, MSc, Universidad Politécnica Salesiana, Ecuador.

Diego Chacon Troya, MSc, Universidad Politécnica Salesiana, Ecuador.

Paul Chasi, MSc, Universidad Politécnica Salesiana, Ecuador.

Juan Chica, MSc, Universidad Politécnica Salesiana, Ecuador.

Diego Marcelo Cordero Guzmán, MSc, Universidad Católica de Cuenca, Ecuador.

Luis Javier Cruz, PhD, Universidad Pontificia Bolivariana, Medellin, Colombia.

Fabricio Esteban Espinoza Molina, MSc, Universidad Politécnica Salesiana, Ecuador.

Jorge Fajardo Seminario, MSc, Universidad Politécnica Salesiana, Ecuador.

Patricia Fernandez Morales, PhD, Universidad Pontificia Bolivariana, Medellin, Colombia.

Marcelo Flores Vazquez, MSc, Universidad Politécnica Salesiana, Ecuador.

Carlos Flores Vázquez, MSc, Universidad Católica de Cuenca, Ecuador.

Carlos Franco Cardona, PhD, Universidad Nacional de Colombia, Colombia.

Cristian García García, MSc, Universidad Politécnica Salesiana, Ecuador.

Teonila García Zapata, PhD, Universidad Nacional Mayor de San Marcos, Perú.

Luis Garzón Mñoz, PhD, Universidad Politécnica Salesiana, Ecuador.

Natalia Gonzalez Alvarez, MSc, Universidad Politécnica Salesiana, Ecuador.

Ernesto Granado, PhD, Universidad Simón Bolívar, Venezuela.

Adriana del Pilar Guaman, MSc, Universidad Politécnica Salesiana, Ecuador.

Juan Inga Ortega, MSc, Universidad Politécnica Salesiana, Ecuador.

Esteban Inga Ortega, PhD, Universidad Politécnica Salesiana, Ecuador.

Paola Ingavélez, MSc, Universidad Politécnica Salesiana, Ecuador.

Cesar Isaza Roldan, PhD, Universidad Pontificia Bolivariana.

Nelson Jara Cobos, MSc, Universidad Politécnica Salesiana, Ecuador.

Ruben Jerves, MSc, Universidad Politécnica Salesiana, Ecuador.

Victor Ramon Leal, PhD, Investigador de PDVSA, Venezuela

Gabriel Leon, MSc, Universidad Politécnica Salesiana, Ecuador.

Edilberto Llanes, PhD, Universidad Internacional SEK, Ecuador.

Luis López, MSc, Universidad Politécnica Salesiana, Ecuador.

Carlos Mafla Yépez, MSc, Universidad Técnica del Norte, Ecuador.

Hader Martínez, PhD, Universidad Pontificia Bolivariana, Medellin, Colombia

Javier Martínez, PhD, Instituto Nacional de Eficiencia Energética y Energías Renovables, Ecuador.

Alex Mayorga, MSc, Universidad Técnica de Ambato, Ecuador.

Jimmy Molina, MSc, Universidad Técnica de Machala, Ecuador.

Andres Montero, PhD, Universidad de Cuenca, Ecuador.

Vicente Morales, MSc, Universidad Tecnica de Ambato, Ecuador.

Fabián Morales, MSc, Universidad Técnica de Ambato, Ecuador.

Diego Morales, MSc, Ministerio de Electricidad y Energías Renovables del Ecuador.

Yoandrys Morales Tamayo, PhD, Universidad Técnica de Cotopaxi, Cotopaxi

Olena Leonidivna Naidiuk, MSc, Universidad Politécnica Salesiana, Ecuador.

Oscar Naranjo, MSc, Universidad del Azuay, Ecuador.

Paul Narvaez, MSc, Universidad Politécnica Salesiana, Ecuador.

Hernán Navas Olmedo, MSc, Universidad Técnica de Cotopaxi, Ecuador.

Cesar Nieto, PhD, Universidad Pontificia Bolivariana, Medellin, Colombia

Fabio Obando, MSc, Universidad Politécnica Salesiana, Ecuador.

Luis Ortiz Fernandez, MSc, Universidade Federal de Rio Grande del Norte, Brasil

Pablo Parra, MSc, Universidad Politécnica Salesiana, Ecuador.

Paulo Peña Toro, PhD, Ministerio de Productividad, Ecuador.

Patsy Prieto Velez, MSc, Universidad Politécnica Salesiana, Ecuador.

Diego Quinde Falconi, MSc, Universidad Politécnica Salesiana, Ecuador.

Diana Quintana Espinoza, MSc, Universidad Politécnica Salesiana, Ecuador.

William Quitiaquez Sarzosa, MSc, Universidad Politécnica Salesiana, Ecuador.

Flavio Quizhpi Palomeque, MSc, Universidad Politécnica Salesiana, Ecuador.

Washington Ramirez Montalvan, MSc, Universidad Politécnica Salesiana, Ecuador.

Fran Reinoso Avecillas, MSc, Universidad Politécnica Salesiana, Ecuador.

Néstor Rivera Campoverde, MSc, Universidad Politécnica Salesiana, Ecuador.

Jorge Romero Contreras, MSc, Universidad de Carabobo, Venezuela

Fabian Saenz Enderica, MSc, Universidad de las Fuerzas Armadas, ESPE, Ecuador.

Luisa Salazar Gil, PhD, Universidad Simón Bolivar, Venezuela

Gustavo Salgado Enríquez, Msc, Universidad Central del Ecuador., Ecuador.

Juan Carlos Santillán Lima, MSc, Universidad Nacional de Chimborazo

Jonnathan Santos Benítez, MSc, Universidad Politécnica Salesiana, Ecuador.

Andrés Sarmiento Cajamarca, MSc, Universidad Federal de Santa Catarina, Brasil

Luis Serpa Andrade, MSc, Universidad Politécnica Salesiana, Ecuador.

Cristian Timbi Sisalima, MSc, Universidad Politécnica Salesiana, Ecuador.

Milton Tipan Simbaña, MSc, Universidad Politécnica Salesiana, Ecuador.

Paul Torres Jara, MSc, Universidad Politécnica Salesiana, Ecuador.

Rodrigo Tufiño Cárdenas, MSc, Universidad Politécnica Salesiana, Ecuador.

Fernando Urgiles Ortíz, MSc, Universidad Politécnica Salesiana, Ecuador.

Juan Valladolid Quitoisaca, MSc, Universidad Politécnica Salesiana, Ecuador.

Efrén Vázquez Silva, PhD, Universidad Politécnica Salesiana, Ecuador.

Julio Verdugo, MSc, Universidad Politécnica Salesiana, Ecuador.

Mary Vergara Paredes, PhD, Universidad de los Andes, Merida, Venezuela

Jennifer Yepez Alulema, MSc, Universidad Politécnica Salesiana, Ecuador.

Julio Zambrano Abad, MSc, Universidad Politécnica Salesiana, Ecuador.

Patricia Zapata Molina, MSc, Universidad Politécnica Salesiana, Ecuador.

The administration of the journal is done through the following parameters:

The journal uses the academic anti-plagiarism system

The articles have an identification code (Digital Object Identifier)

The editorial process is managed through the Open Journal System

It is an open access publication (Open Access) licensed Creative Commons

The articles of the present edition can be consulted in
http://revistas.ups.edu.ec/index.php/ingenius

INGENIUS Journal, is indexed in the following Databases and scientific information systems:

SELECTIVE DATABASES

REVIEWS EVALUATION PLATFORMS

SELECTIVE DIRECTORIES

SELECTIVE SERIAL LIBRARY

SCIENTIFIC LITERATURE SEARCHERS OPEN ACCESS

OTHER BIBLIOGRAPHICAL DATABASES

CATALOG OF INTERNATIONAL UNIVERSITY LIBRARIES

UNIVERSITÄT PASSAU
Fakultät für Informatik und Mathematik

BSB Bayerische StaatsBibliothek
Information in erster Linie

Deutsches Museum

Hochschule Rosenheim
University of Applied Sciences

HOCHSCHULE LANDSHUT
HOCHSCHULE FÜR ANGEWANDTE WISSENSCHAFTEN

HOCHSCHULE FÜR ANGEWANDTE WISSENSCHAFTEN MÜNCHEN

HOCHSCHULE WEIHENSTEPHAN-TRIESDORF
UNIVERSITY OF APPLIED SCIENCES

TUM Technische Universität München

Universität der Bundeswehr München

LMU LUDWIG-MAXIMILIANS-UNIVERSITÄT MÜNCHEN

Technische Hochschule Ingolstadt

Hochschule Augsburg
University of Applied Sciences

Hochschule Kempten
University of Applied Sciences

HNU HOCHSCHULE NEU-ULM UNIVERSITY OF APPLIED SCIENCES

OTH OSTBAYERISCHE TECHNISCHE HOCHSCHULE REGENSBURG

Ostbayerische Technische Hochschule Amberg-Weiden

Staatliche Bibliothek Neuburg an der Donau

Staatliche Bibliothek Regensburg

STAATS- UND STADTBIBLIOTHEK AUGSBURG

GEORG-SIMON-OHM HOCHSCHULE NÜRNBERG

Universitätsbibliothek Augsburg UBA

KATHOLISCHE UNIVERSITÄT EICHSTÄTT–INGOLSTADT

UR Universität Regensburg

HOCHSCHULE ANSBACH

COBURG UNIVERSITY of applied sciences and arts

hochschule hof University of Applied Sciences

HOCHSCHULE MERSEBURG (FH) University of Applied Sciences

ThULB THÜRINGER UNIVERSITÄTS- UND LANDESBIBLIOTHEK JENA

EZB Elektronische Zeitschriftenbibliothek

OTTO-FRIEDRICH-UNIVERSITÄT BAMBERG

UNIVERSITÄT BAMBERG

UNIVERSITÄT BAYREUTH

FAU FRIEDRICH-ALEXANDER UNIVERSITÄT ERLANGEN-NÜRNBERG

Bauhaus-Universität Weimar

UB WÜ

Freie Universität Berlin

FHE FACHHOCHSCHULE ERFURT UNIVERSITY OF APPLIED SCIENCES

h² Hochschule Magdeburg • Stendal

htw Hochschule für Technik und Wirtschaft Berlin University of Applied Sciences

UB Braunschweig

STIFTUNG • TIERÄRZTLICHE HOCHSCHULE HANNOVER 1778

GOTTFRIED WILHELM LEIBNIZ BIBLIOTHEK NIEDERSÄCHSISCHE LANDESBIBLIOTHEK

Dear readers:

The year 2020 has brought us a severe pandemic derived from the COVID-19. Until now we had thought that this situation we are living, was rather, the script of a science fiction movie. However, as we have been able to prove often, sometimes (more than we would like to admit), reality surpasses fiction; and that is what has happened and is happening in these complicated months.

The COVID-19 pandemic has led us to extreme situations: collapse of health systems, confinement at home to avoid the spreading of the virus, switching from face-to-face to virtual teaching, shutdown of producing companies, closing of borders, etc.

This paralysis caused by the confinement has revealed what is and what is not necessary for the functioning of a society. Overall, this medical crisis, with its social and economic impacts, has revealed that there are many dispensable things, and other that are absolutely essential. The health systems have been overwhelmed in many countries, the action of security bodies was not able to guarantee the security of people; Governments had to take difficult measures.

Ultimately, this virus has challenged the whole planet, with greater or lesser intensity, but we have learned much from this situation. We have learned to appreciate the professionalism and vocation of the health personnel. We have learned to adapt. We have learned to perform our professional activities through videoconference, to the extent possible. We have learned that the security of our society is based on strict confinement measures. We have learned to «stay at home», without being able to hug and interact with our most loved ones, friends and colleagues. We have learned that a virus, such as many we face every day, can pose a serious threat to humanity. And this is where an additional aspect we have learned comes in.

We have learned to need and demand R+D to overcome this crisis. Practically from the start of the pandemic, collaboration and research was requested in different ambits. From the first day, work was already under way in the development, in the months to come, of a possible vaccine that prevents this pandemic. From the health system it was requested support to the technological, corporate and university sectors, with ideas and developments for manufacturing improvised respirators, protection systems, disinfection systems, action protocols, etc.

All this has a common denominator: investment in R+D. Without R+D (and transfer) we are condemned to not evolving and not being able to face other situations that the future may bring.

The commitment of INGENIUS with science, technology and the generation of innovative ideas, has always been very strong. Along these months INGENIUS has continued its activity which is, definitely, making available to the society the knowledge in the ambit of science, technology and engineering that enable developing technologic solutions in moments of crisis, and contribute to the sustainable development of our society. It is true that R+D is absolutely necessary, but it is similarly true that the technology transfer is also important, because it enables to apply R+D in products and services useful and necessary for our society. Perhaps we still do not know what is not necessary, but what has become evident, is what we certainly need: investment in research, development and transfer to the society and there, INGENIUS reaffirms once again its strong commitment to the service of the international scientific community.

Rafael Antonio Balart Gimeno, PhD

EDITOR IN CHIEF

TABLE OF CONTENTS

RESISTANCE EFFECT ESTIMATION IN THE SHORT CIRCUIT CURRENT THROUGH A SENSITIVITY ANALYSIS

ESTIMACIÓN DEL EFECTO DE LA RESISTENCIA EN LA CORRIENTE DE CORTOCIRCUITO MEDIANTE UN ANÁLISIS DE SENSIBILIDAD

Moronta R. José A.[1,*], Rocco Claudio M.[2]

Abstract

The assessment of the current in an electrical power system (EPS) after a fault, is generally termed short-circuit analysis. The magnitude of those currents is used for dimensioning the protection equipment of the EPS. Short-circuit analysis assumes that the electrical resistances of the components can be neglected, since they do not significantly affect the magnitude of the short-circuit currents. This work quantifies the effect of the electrical resistance of the elements of the EPS on the magnitude of the short-circuit current, by means of sensitivity (SA) and uncertainty (UA) analyses. The SA is based on the variance decomposition of an output variable, and can quantify the main effects (importance) and the interactions of the variables considered. On the other hand, The UA allows assessing how the variations in the variables considered affect the output. The proposed approach is illustrated on two networks from the literature, considering three-phase and single-phase faults. The results of such proposed approach numerically show that the effects due to taking into account the electrical resistance are indeed negligible, when compared to the rest of variables considered in the short-circuit analysis. This result coincides with the assumptions reported in the literature for the calculation of the fault currents.

Keywords: Short circuit current, electrical resistance, sensitivity analysis.

Resumen

El cálculo de los valores de corriente que fluyen en un sistema eléctrico de potencia (SEP) posterior a una falla, se denomina análisis de falla o de cortocircuito. Los valores de la corriente de cortocircuito son empleados para el dimensionamiento de los equipos de protección del SEP. Los análisis de cortocircuito tienen como una de sus premisas despreciar la resistencia eléctrica de los elementos del sistema, pues esta no afecta en mayor medida las magnitudes de las corrientes de cortocircuito. En este trabajo se propone cuantificar el efecto de la resistencia eléctrica de los elementos del SEP en la magnitud de la corriente de cortocircuito, mediante un análisis de sensibilidad (AS) e incertidumbre (AI). El AS se basa en la descomposición de la varianza de una variable de salida y puede cuantificar los efectos principales (importancia) y las interacciones de las variables consideradas. Por otro lado, el AI permite evaluar cómo las variaciones en las variables consideradas afectan la salida. La propuesta se ilustra sobre dos redes de la literatura, considerando fallas trifásica y monofásica. El resultado de nuestra propuesta muestra numéricamente que los efectos debidos a considerar la resistencia eléctrica son de hecho insignificantes, en comparación con el resto de los factores que intervienen en el análisis de cortocircuito. El resultado coincide con las premisas de cálculo de las corrientes de falla supuestas en la literatura.

Palabras clave: corriente de cortocircuito, resistencia eléctrica, análisis de sensibilidad.

[1,*]Departamento de Tecnología Industrial, Universidad Simón Bolívar, Venezuela.
Corresponding author: ✉: jmoronta@usb.ve. ⬥ https://orcid.org/0000-0002-8836-6255
[2]Facultad de Ingeniería, Universidad Central de Venezuela, Venezuela ⬥ https://orcid.org/0000-0002-8022-0446

1. Introduction

The short circuit studies are analyses that are used to determine the magnitude of the electrical currents that go through the electrical power systems (EPS), during a fault. Afterwards, such magnitudes are utilized to specify or validate the characteristics of the components of the system, such as breakers, buses, among others [1].

Short circuit studies in the EPS generally assume that the electrical resistance of the elements of the system is negligible, and exclusively consider their electrical reactance for calculating the magnitude of the short circuit current. According to [2], for most calculations of short circuit currents in medium and high voltage, and in some cases in low voltage, when the reactances are «much greater» than the resistances, is sufficiently accurate and simpler neglecting the resistances and considering only the reactances. Note that the rule is not specific, only suggests when the reactance is much greater than the resistance.

The same assumption for calculating the short circuit currents is made in the standard [3], where it is indicated that the calculation is much simpler, but with a loss of accuracy if the resistances are neglected, when the reactance/resistance (X/R) ratio is greater than 3.33.

The literature related to the analyses of EPS suggest similar procedures, regarding the possibility of neglecting the resistance of the elements. For example, it is indicated in [1] that it is possible to neglect the resistances in the fault study, because «it is not likely that they significantly influence in the level of the fault current».

A group of assumptions is presented in [4] for short circuit calculation, where it is suggested to neglect all the resistances of the elements (generators, transformers and transmission lines) to simplify the calculation.

Other works [5, 6], establish 5 % as a maximum error in the value of the short circuit current, if the resistance of the elements of the system is neglected. This suggestion is derived from the general expression to determine the fault current, see equation (1):

$$|I_{cc}| = \frac{|V_{fault}|}{|R_{fault} + jX_{fault}|} = \frac{|V_{fault}|}{X_{fault} \times \sqrt{1 + \left(\frac{R_{fault}}{X_{fault}}\right)^2}} \tag{1}$$

Where:

I_{cc} = Short circuit current (A)
V_{fault} = Pre-fault voltage (V)
R_{fault} = Resistance at the fault point (Ω)
X_{fault} = Reactance at the fault point (Ω)

Where R_{fault} and X_{fault} correspond to the equivalent Thevenin impedance at the fault point. When the ratio (X/R) is greater than 4, the error made by neglecting the resistance is smaller than 4 %. This is valid except for distribution or industrial systems where this ratio is smaller than 4 [6].

In power systems, the value of the resistance of the elements is usually very small compared to the value of their reactance. This consideration is the reason in which standards and authors are based for neglecting the resistances and their influence in the determination of the fault currents. In real power systems, the ratio X/R between the reactance and the resistance at the fault point is usually of an order between 15 and 120 times [7].

The references agree that the electrical resistance may be neglected in short circuit analyses, but there is no consensus regarding their effect in the magnitude of the short circuit currents.

In this work, the sensitivity analysis (SA) is used to quantify the effect of varying the resistance in the value of the short circuit current, for two networks in the literature. In addition, it is defined the relationship of these variations with the remaining parameters that enable determining the short circuit current (voltage and electrical reactance of the elements). The analysis is based on the use of the theory of SA and UA, and as a result of these analyses the same conclusion presented in the literature is directly reached, but from a different perspective.

The structure of the work is as follows: the first section presents some fundamental definitions associated to the sensitivity analysis; the second describes the procedure for determining the uncertainty associated to the short circuit current and the test electrical power systems; the third presents and discusses the results obtained and, finally, the fourth presents conclusions and future works.

1.1. Sensitivity and uncertainty analyses

According to [8], the uncertainty analysis (UA) is defined as the study of the amount of uncertainty contributed to the output of a model, by the different sources of uncertainty in the input. On the other hand, the sensitivity analysis (SA) evaluates the importance of the input variables of a model. Such importance is measured as a function of how much variability in the output of the model is due to the variability in the input variables. In this case, the uncertainty in the input variables is modeled through distribution functions with known parameters.

According to [8], the steps to carry out the SA/UA approach are defined as:

- Establish the objective of analysis, and accordingly define the form of the outputs of the model.

- Decide which input factors will be included in the analysis.

- Choose a probability distribution function for each of the input factors.

- Choose a method for SA, according to the characteristics of the problem under study.

- Generate the sample of the input factors. The sample is generated according to the specifications of the known parameters and the selected size of the sample.

- Evaluate the sample generated in the model and produce the corresponding outputs, which contain the values according to the form specified in step 1.

- Analyze the outputs of the model, determine the sensitivity indices (importance) and establish the conclusions.

The methods of SA can be classified according to the output of their measures: quantitative or qualitative, local (they do not allow varying all factors simultaneously) or global (they allow varying all factors simultaneously) and dependent or independent of the model [9].

Given a model $Y = F(X_1, X_2, X_3, \ldots, X_n)$ where Y is its output and X_i represent the input variables modeled as random variables (i.e., its uncertainty is modeled as a probability density function (pdf)), the variance $V(Y)$ of the output Y may be described as in equation (2) [8]:

$$V(Y) = \sum_i V_i + \sum_i \sum_{j>i} V_{ij} + \sum_i \sum_{j>i} \sum_{l>j} V_{ijl} + \cdots V_{12\ldots k} \tag{2}$$

Where:

$V_i = V(E(YlX_i))$ is the main effect (or of first order) due to x_i

$V_{ij} = V(E(YlX_i, X_j)) - V_i - V_j$ is the second order effect due to the interaction between x_i and x_j, and so forth.

The main sensitivity (S_i) and total (S_{Ti}) effects, may be defined as given in equations (3) and (4), respectively, according to [8]:

$$S_i = \frac{V_i(E_{-i}(Y|X_i))}{V(Y)} \tag{3}$$

$$S_{Ti} = \frac{E_{-i}(V_i(Y|X_{-i}))}{V(Y)} \tag{4}$$

Where:

$X_{-i} = (x_1, x_2, \ldots x_{i-1}, x_{i+1}, \ldots, x_k)$ and $E_{-i}(Y \mid X_i)$

is the expected value of Y conditioned to x_i, and, therefore, is only a function of x_i.

The main index S_i is the fraction of the variance $V(Y)$ of the output that can be attributed to x_i only, while S_{Ti} corresponds to the fraction of $V(Y)$ that can be attributed to x_i, including all its interactions with the other input variables.

The main index S_i is the measure employed to determine the input variables that mainly affect the output uncertainty, while S_{Ti} is utilized to identify the subset of not influential input variables, i.e., those variables that can be fixed at any value in their uncertainty range, and they do not significantly affect the variance of the output [10].

The estimates of S_i y S_{Ti} are approximated: 1) assuming (statistical) independence between the input variables; 2) using particular sampling techniques to generate samples of the input variables; and 3) evaluating the group of samples obtained in 2) from the model under study [8].

There are different techniques for sensitivity analysis based on the decomposition of the variance; several of these techniques are mentioned in [10]. These techniques differ with respect to their computational complexity, as well as in the effects that they evaluate (main and/or total). Among these techniques, it should be mentioned: Sobol [11] that enables evaluating the main and total effects, and EFAST (Extended Fourier Amplitude Sensitivity Test) [12], an extension of FAST (Fourier Amplitude Sensitivity Test) [13], that also evaluates the main and total effects (S_i and S_{Ti}), but with less computational complexity than the Sobol method.

2. Methodology

The following approach is proposed to estimate the effect of the electrical resistance of the elements (input variables of the model) on the short circuit current (output of the model):

A uniform distribution $U[0-1, 2 \times valor\ base]$ is assumed for the input variables (pre-fault voltage, resistance and impedance of the elements of the power system). The distribution is asymmetrical and enables quantifying the effect of neglecting (values close to zero) the resistance of the elements of the power system.

After the evaluation of the described procedure (SA), a Monte Carlo simulation [14] is carried out considering only the variables of interest (electrical resistance of the elements). The Monte Carlo simulation is a method employed to evaluate the propagation of uncertainty through the generation of random variables. In this way, the propagation of the uncertainty is quantified at the output of the model, i.e., the vari-

ation of the magnitude of the short circuit current is quantified.

The short circuit calculation and the SA/UA were carried out in the R free software [15]; specifically, the algorithms from the Sensitivity library were utilized for the SA.

2.1. Test electrical systems

2.1.1. Test power system 1 (TPS1)

The power system employed [16] is a nonmeshed network with two sources, as shown in Figure 1. It is constituted by an external system, two transmission lines, one transformer and one generator. It is assumed a solid three-phase to ground fault in $k3$.
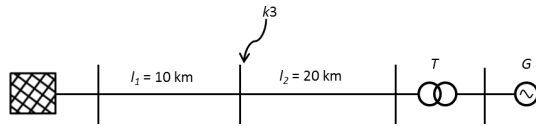
Figure 1. Radial test power system (TPS1)

The elements of the radial test power system 1 (TPS1) are modeled; the values are shown in Table 1. These values represent the input variables of the model of SA.

Table 1. Impedance of the elements of the test power system 1 (TPS1)

N.º	Variable	Value
1	Pre-fault voltage	110 kV
2	Resistance external system	0,605 Ω
3	Reactance external system	6,050 Ω
4	Resistance line 1	1,930 Ω
5	Reactance line 1	3,860 Ω
6	Resistance generator	8,879 Ω
7	Reactance generator	126,762 Ω
8	Resistance transformer	2,710 Ω
9	Reactance transformer	53,171 Ω
10	Resistance line 2	2,440 Ω
11	Reactance line 2	7,440 Ω

2.1.2. Test power system 2 (TPS2)

The meshed electrical network taken from [16], for which it is assumed a solid one-phase to ground fault in $k1$ (see Figure 2). The values of the elements are shown in Table 2, which are the input factors for the sensitivity analysis.
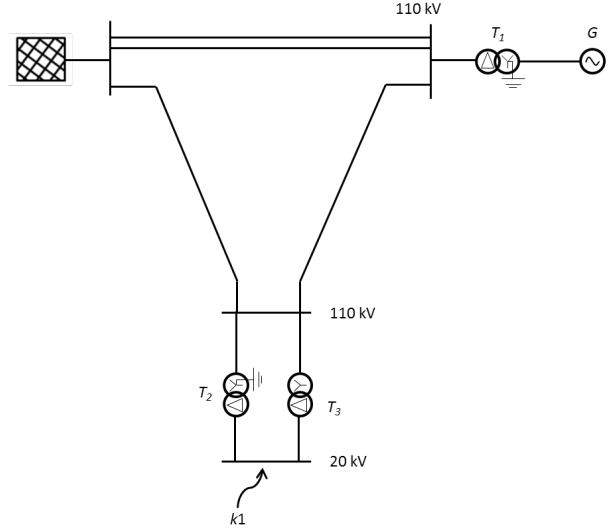
Figure 2. Meshed test power system (TPS2)

Since it is a one-phase fault, it is solved using the method of the sequence networks [1], and the elements should be modeled with their corresponding values of positive, negative and zero sequence. In order words, the parameters that take part in the SA are increased by 3. For example, for a line there will be a resistance of positive, negative and zero sequence.

Table 2. Impedance of the elements of the test power system 2 (TPS2)

N.º	Variable	Value	Nº	Variable	Value
1	Pre-fault voltage	20 kV	24	Resist. Line 3_0	0,161 Ω
2	Resist. External System _0	0,030 Ω	25	React. Line 3_0	0,648 Ω
3	React. External System_0	0,300 Ω	26	Resist. Line 3_+	0,061 Ω
4	Resist. External System_+	0,020 Ω	27	React. Line 3_+	0,199 Ω
5	React. External System_+	0,200 Ω	28	Resist. Line 3_-	0,061 Ω
6	Resist. External System_-	0,020 Ω	29	React. Line 3_-	0,199 Ω
7	React. External System_-	0,200 Ω	30	Resist. Transf. 1_0	0,147 Ω
8	Resist. Generator_+	0,224 Ω	31	React. Transf. 1_0	2,746 Ω
9	React. Generator_+	3,200 Ω	32	Resist. Transf. 1_+	0,147 Ω
10	Resist. Generator_-	0,224 Ω	33	React. Transf. 1_+	2,746 Ω
11	React. Generator_-	4,800 Ω	34	Resist. Transf. 1_-	0,147 Ω
12	Resist. Line 1_0	0,084 Ω	35	React. Transf. 1_-	2,746 Ω
13	React. Line 1_0	0,374 Ω	36	Resist. Transf. 2_0	0,027 Ω
14	Resist. Line 1_+	0,016 Ω	37	React. Transf. 2_0	0,761 Ω
15	React. Line 1_+	0,064 Ω	38	Resist. Transf. 2_+	0,027 Ω
16	Resist. Line 1_-	0,016 Ω	39	React. Transf. 2_+	0,761 Ω
17	React. Line 1_-	0,064 Ω	40	Resist. Transf. 2_-	0,027 Ω
18	Resist. Line 2_0	0,161 Ω	41	React. Transf. 2_-	0,761 Ω
19	React. Line 2_0	0,648 Ω	42	Resist. Transf. 3_+	0,027 Ω
20	Resist. Line 2_+	0,061 Ω	43	React. Transf. 3_+	0,761 Ω
21	React. Line 2_+	0,199 Ω	44	Resist. Transf. 3_-	0,027 Ω
22	Resist. Line 2_-	0,061 Ω	45	React. Transf. 3_-	0,761 Ω
23	React. Line 2_-	0,199 Ω			

Note: The symbols +, -, 0 indicate the values of positive, negative and zero sequence, respectively.

3. Results

3.1. Test power system 1 (TPS1)

Figure 3 shows the sensitivity indices of first order (S_i) (white part of the bars) and total (S_{Ti}) (complete bar, white and gray parts) for the TPS1. The variables that most affect the short circuit current are, in order of importance: the pre-fault voltage ($S_1 = 0.456$), the reactance of the external system ($S_3 = 0.252$) and the reactance of line 1 ($S_5 = 0.108$). The remaining factors, including the resistance of the elements, have very small values of importance S_{Ti}, and consequently their effects may be considered negligible.
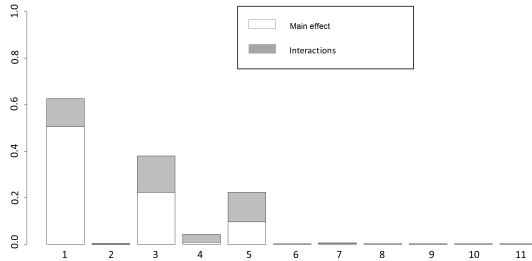
Figure 3. Main (S_i) and total (S_{Ti}) effects of the input variables in the short circuit current of the TPS1

As it was mentioned, the pre-fault voltage has a very high importance (0.456); due to this, it is subsequently fixed as a constant in the model, in order to

only evaluate the effects of the reactances and resistances of the elements; likewise very small effects were obtained for the resistances.

For comparison purposes, all the main effects of the resistances and the main effects of the less important reactances were grouped (see Figure 4), keeping constant the pre-fault voltage. The sum of the main effect of the resistances is negligible compared to the main effect of the reactances, in this system and, for this particular fault, the most important variable is the reactance of the external system.
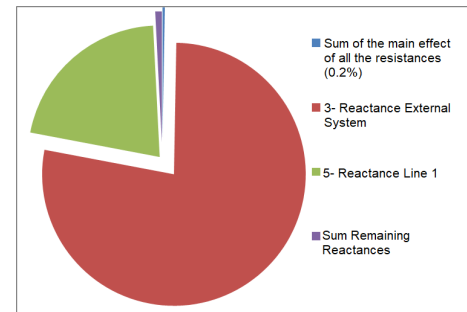
Figure 4. Main effects of the reactances and sum of the main effects of the resistances.

After evaluating the SA, and only considering the resistances of the elements, the evaluation of the Monte Carlo method [14] is carried out, to obtain the approx-

imate probability distribution of the short circuit current for 5000 evaluations. The short circuit current for the values of Table 1 is 7196 A, which corresponds to the normalized value of 1 unit, in the approximate histogram of the short circuit current presented in Figure 5. The minimum and maximum values obtained for the short circuit current were 0.995 and 1.031, respectively. The average value of this distribution is 1.022, and the shape of the distribution is asymmetrical, with a bias to the upper end.

Distribution of the short circuit current (TPS1)
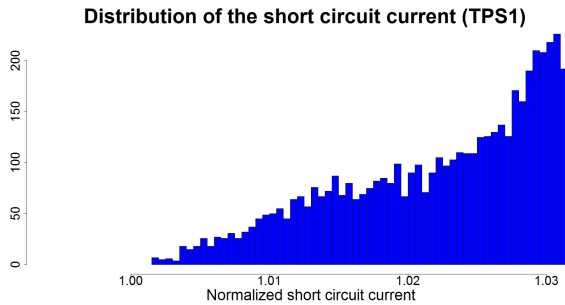
Figure 5. Approximate histogram of the short circuit current (TPS1)

The literature refers to the X/R ratio to neglect the electrical resistance in the short circuit calculations. For this reason, Figure 6 shows the short circuit current normalized for the values of X/R obtained in the Monte Carlo simulation. The values of the X/R ratio vary from approximately 4 to 400; considering this wide range, the normalized short circuit current does not exhibit variations achieving at least 4 %.

Normalized short circuit current vs. X/R ratio
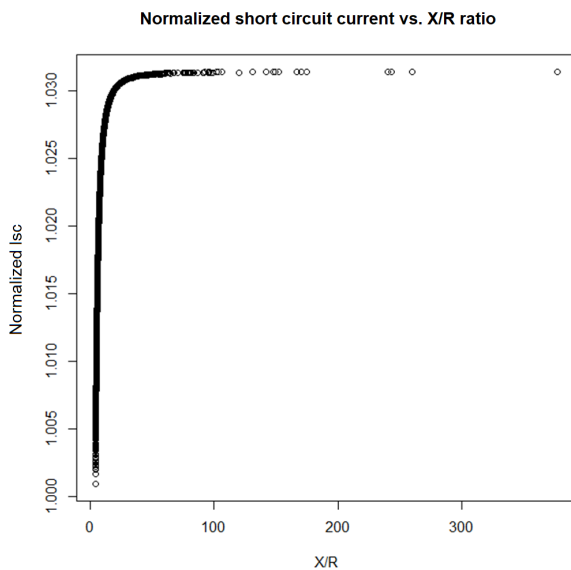
Figure 6. Short circuit current normalized for the values of X/R (TPS1).

3.2. Test power system 2 (TPS2)

The results obtained for the meshed power system TPS2 are similar to those obtained for the TPS1. The pre-fault voltage turns out to be the most important variable (see Figure 7). In this system, there is more uncertainty of superior order associated to the interaction of variables (S_{Ti} - S_i), which is due to the fact that the system is meshed, and various equivalent impedances (successive sums and products) should be calculated to obtain the short circuit equivalent impedance.
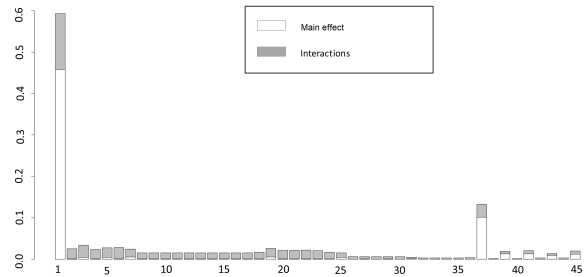
Figure 7. Main (S_i) and total (S_{Ti}) effects of the input variables in the short circuit current of the TPS2.

The numbers of the variables (x-axis) of Figure 7, are in accordance with the numbering of Table 2. Note that the variable 37 (zero sequence reactance of transformer 2) appears as the second most important variable, even though with a very small contribution.

Figure 8 shows a comparison of the sum of the total indices of the resistances and of the reactances of the system TPS2, considering constant the pre-fault voltage; the percentage represented by the index of the sum of the resistances is slightly smaller than 7 %.
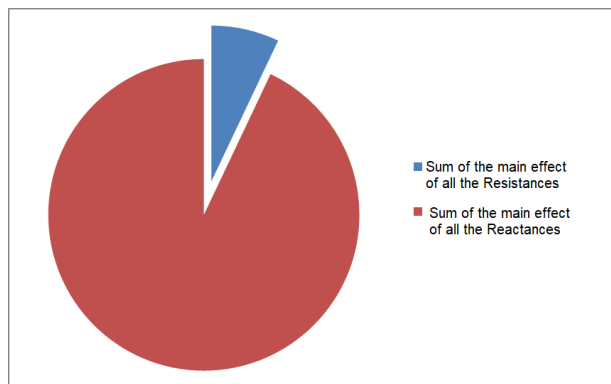
Figure 8. Sum of the main effects of the resistances and reactances of the TPS2

Figure 9 shows the approximate histogram for the short circuit current, obtained using the Monte Carlo technique disturbing only the resistances of the elements of the system TPS2. For the values in Table 2 this current is 13679 A, which corresponds to the

normalized value of 1 unit, in the histogram of Figure 9. The minimum and maximum values obtained for the short circuit current were 0.9999 and 1.0037, respectively. Note that carrying out variations in the resistances, the effect on the short circuit current is negligible. This distribution is more symmetrical than the one in the previous example, and has an average value of 1.002.
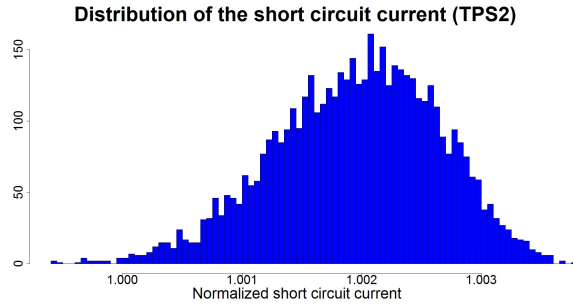
Figure 9. Approximate histogram of the short circuit current (TPS2)

Figure 10 shows the short circuit current normalized for the values of X/R obtained in the Monte Carlo simulation, for the TPS2 system. In this case the variation is much smaller, since the normalized short circuit current does not exhibit variations achieving 1 %.
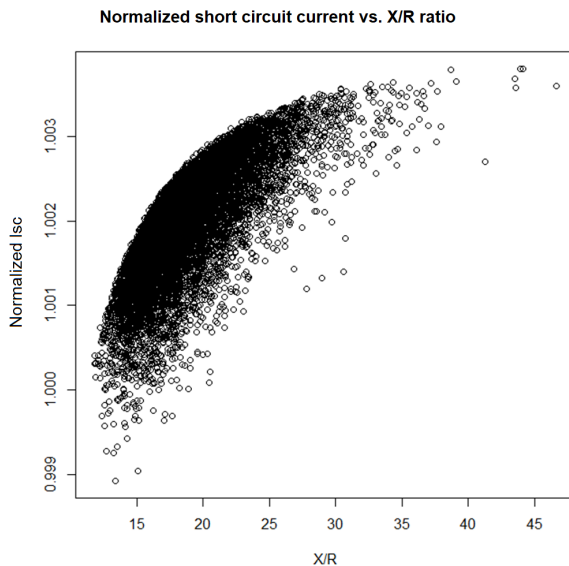
Figure 10. Short circuit current normalized for the values of X/R (TPS2)

4. Conclusions

In this work, it is estimated the uncertainty of the short circuit current due to the electrical resistance of the elements, through an approach of sensitivity and uncertainty. This analysis can be applied to any other power system with any location and/or type of fault.

For the two cases under consideration, the results are in accordance with what is suggested by different authors: it is possible to neglect the resistance of the elements, whenever their reactance is much greater than their resistance (X/R ratio). The variation of the magnitude of the short circuit current in the two cases evaluated does not exceed 4 %, which coincides with the value of 4-5 % reported in some consulted works [5, 6].

This analysis not only considers the uncertainty in the short circuit current, due to the uncertainty in the resistances and reactances, but also enables quantifying the total variation, i.e., the percentage due to the uncertainty of the resistances of the components of the EPS. In these two cases, the effect of the resistance of the elements is approximately 7 % (in the test power system 2 (TPS2)); the rest is associated to the reactances, if the value of the pre-fault voltage is considered constant, for the sensitivity analysis carried out.

The results obtained in these two systems, could be extrapolated to real power systems in medium or high voltage, because in such systems the reactance is usually much greater than the resistance (X≫R). As a future work, it is intended to establish ratios and/or critical values between the reactance/resistance factor (X/R) at the fault point of the system, and the main indices (S_i) of the uncertainty of the short circuit current.

References

[1] J. Grainger and W. Stevenson, *Análisis de Sistemas de Potencia.* Mc Graw Hill, 1996. [Online]. Available: https://bit.ly/3bsZqDF

[2] IEEE, *IEEE Recommended Practice for Electric Power Distribution for Industrial Plants*, 1994. [Online]. Available: https://doi.org/10.1109/IEEESTD.1994.121642

[3] IEC, *IEC Short-circuit currents in three-phase A. C. systems: Part 0: Calculation of currents / Part 4: Examples for the calculation of short-circuit currents,*, 2016. [Online]. Available: https://bit.ly/2WUfBEF

[4] J. Glover and M. Sarma, *Sistemas de potencia: análisis y diseño.* International Thomson Editores, 2003. [Online]. Available: https://bit.ly/2WOIW3s

[5] R. Gil Bernal, *Estudios en sistema de potencia*, 2000. [Online]. Available: https://bit.ly/2Z27ZD4

[6] F. M. González-Longatt, *Cortocircuito simétrico*, 2007. [Online]. Available: https://bit.ly/3dGVpgn

[7] IEEE, *IEEE Application Guide for AC High-Voltage Circuit Breakers > 1000 Vac Rated on a Symmetrical Current Basis*, 2017. [Online]. Available: https://doi.org/10.1109/IEEESTD.2017.7906465

[8] A. Saltelli, S. Tarantola, F. Campolongo, and M. Ratto, *Sensitivity analysis in practice.* John Wiley and Sons, Ltd, 2013. [Online]. Available: https://bit.ly/2LD6oM5

[9] V. Schwieger, "Variance-based sensitivity analysis for model evaluation in engineering surveys," *INGEO 2004 and FIG Regional central and Eastern European conference on engineering surveying, Bratislava, Slovakia*, 01 2004. [Online]. Available: https://bit.ly/3cw8IQy

[10] S. Tarantola, "Variance-based methods for sensitivity analysis," *Int. Conf. on Sensitivity Analysis of Model Output. Joint Research Center of the European Commission*, 2002. [Online]. Available: https://bit.ly/2y3Rzim

[11] I. M. Sobol, "Sensitivity estimates for nonlinear mathematical models," *Mathematical modelling and computational experiments*, vol. 1, no. 4, pp. 407–414, 1993. [Online]. Available: https://bit.ly/2Lq0M7F

[12] A. Saltelli, S. Tarantola, and K. P. S. Chan, "A quantitative model-independent method for global sensitivity analysis of model output," *Technometrics*, vol. 41, no. 1, pp. 39–56, 2012. [Online]. Available: https://bit.ly/2Z28H2P

[13] R. I. Cukier, C. M. Fortuin, K. E. Shuler, A. G. Petschek, and J. H. Schaibly, "Study of the sensitivity of coupled reaction systems to uncertainties in rate coefficients. i theory," *The Journal of Chemical Physics*, vol. 59, no. 8, pp. 3873–3878, 1973. [Online]. Available: https://doi.org/10.1063/1.1680571

[14] M. G. Morgan and M. Henrion, "Uncertainty: A guide to dealing with uncertainty in quantitative risk and policy analysis," 1990. [Online]. Available: https://bit.ly/2YZpJ1D

[15] The R Development Core Team, *R: A language and environment for statistical computing*, 2013. [Online]. Available: https://bit.ly/3dMHNQV

[16] M. Eremia and M. Shahidehpour, *Handbook of Electrical Power System Dynamics: Modeling, Stability, and Control.* John Wiley and Sons, 2013. [Online]. Available: http://doi.org/10.1002/9781118516072

Moisture in Concrete Aggregates and its relation to the Dielectric Constant

Humedad y su relación con la espectroscopía dieléctrica en agregados de concreto

Franco Abanto[1,*], Pedro Rotta[1], Luis LaMadrid[1], Juan Soto[1], Gerson La Rosa[1],

José Manrique[1], Gaby Ruiz[1], William Ipanaque[1]

Abstract

Measurement of moisture content (CH) of concrete aggregates (AOC) in the manufactury of ready mixed concrete is one of the currently challenges in the building industry since affect to the final properties of concret. At present, the methods for measurement of CH in AOC are invasive and destructive. This paper presents a novel sensing technique using dielectric espectroscopy (ED), a method that using the propagation of microwaves on the material allows the correlation of its dielectric constant (CD) and its CH. In this research is used this method in AOC. Three diferents peruvian quarries (Moyobamba, Sol sol y Cerro Mocho) have been used. The results shows that the sensor at the frequency of 1.5GHz is capable of detecting the CH in AOC with linear regression of $R^2 = 95\%$. In conclusion, is available using the ED as a online and no invasive sensing method of CH in AOC for using in the building industry.

Keywords: moisture contentent, microwaves, dielectric spectroscopy, dielectric contant, concrete aggregates.

Resumen

Medir el contenido de humedad (CH) de los agregados de concreto (ADC) en la fabricación de concreto premezclado es uno de los retos actuales en la industria de la construcción porque afecta a las propiedades finales del concreto. Actualmente los métodos que se utilizan para medir el CH en ADC son invasivos y destructivos. Este artículo presenta una técnica moderna basada en espectroscopía dieléctrica (ED), un método que al propagar microondas en el material correlaciona su constante dieléctrica (CD) y su CH. En esta investigación se ha utilizado este método en ADC. Tres diferentes canteras peruanas de ADC (Moyobamba, Sol-Sol y Cerro Mocho) han sido utilizadas. Los resultados demuestran que el sensor a una frecuencia de 1.5 GHz es capaz de detectar el CH en ADC con una regresión lineal de $R^2 = 95\%$. En conclusión, se puede utilizar la ED como un método de sensado no invasivo y en línea de CH en ADC para ser utilizado en la industria de la construcción.

Palabras clave: contenido de humedad, microondas, espectroscopía dieléctrica, constante dieléctrica, agregados de concreto

1. Introduction

The moisture content (MC) of a material is a parameter that many industrial sectors seek to control in their processes, because it impacts the final characteristics of the product. In the construction industry, the MC of the concrete is important since it defines the mechanical properties and the useful life of a civil project [1]. Studies have been carried out to analyze the durability and resistance in concrete structures measuring the MC [2], and also in concrete test tubes [3]. No research studies have been conducted about systems for measuring the MC of the AOC online, during the mixing process in the plant. Authors in [4–6] show different techniques to perform the measurement of the MC of materials. In the present paper it is utilized a methodology based on dielectric spectroscopy, which has been tested in soil [7], wool [8], paper [9], fabric [10], flour [11], wood [12–14].

There are various methods for measuring the MC of materials, which are classified in direct and indirect. In the direct methods the MC is obtained without correlating with other variables. These are the thermogravimetric and chemical methods. The thermogravimetric method is not selective [15, 16], the effective measuring range varies from 0.5 % to 99.9 % for the MC, and its precision is 0.5 % of the total mass. In contrast, the chemical method [17–19] is selective, it has a precision of 0.0001 % and a measuring range from 0.00001 to 99.9 % of MC.

The indirect methods require a prior calibration to obtain the MC using direct methods. The indirect methods are classified in passive and active. The former utilize elements such as variable resistances or capacitances to determine the MC, which is by nature an invasive control. The active are those that emit electromagnetic waves to determine the characteristics of the medium, thus guaranteeing and online control and the integrity of the sample by not being invasive nor destructive.

The results of different research works in [20–23] in the field of active methods, demonstrate that there is a relationship between the MC and the relative permittivity (ε') or dielectric constant (DC) [24] of a material.

The indirect methods use techniques such as the DS, which seeks to measure the DC of the material, and is also utilized for other purposes such as characterizing materials. Another indirect technique is the use of hyperspectral images, which has had good success in bioengineering [25] and in agroindustry [26–29].

Authors show applications with DS oriented to the agriculture, with the purpose of estimating the quality of their products [30–41], which include applications in seeds, wheat, grains, nuts, fruits of oil palm and bananas.

This paper describes theoretical concepts of the DS and its relationship with the MC [6]. An application is presented that uses the DS to seek for the correlation between the MC and the DC of AOC with different quarries, and verifying the possibility of this new method in this industry.

1.1. Description of the electromagnetic waves

Electromagnetic fields refers to the group of fields of electric and magnetic forces produced by electric charges and currents in movement through the vacuum or any type of matter. When an electromagnetic field propagates in the space it is called propagation of electromagnetic waves.

The propagation of electromagnetic waves is based on the solution of Maxwell's equations.

$$\nabla \times \overline{E} = \overline{M} - \frac{\partial \overline{B}}{\partial t} \ (Faraday's\ law) \tag{1}$$

$$\nabla \times \overline{H} = \overline{J} - \frac{\partial \overline{D}}{\partial t} \ (Ampere's\ law) \tag{2}$$

$$V.\overline{D} = \rho \ (Gauss's\ law) \tag{3}$$

$$V.\overline{H} = 0 \ (Gauss's\ law) \tag{4}$$

Where:

E is the electric field [V/m]
H the magnetic field [A/m]
M is the density of magnetic current [V/m^2]
J is the density of electric current [A/m^2]
B is the density of magnetic flux [Wb/m^2]
D is the density of electric flux [Coul/m^2]
ρ is the density of charge [Coul/m^3]

In order to solve Maxwell's equations it is supposed propagation in free space and, besides, a sinusoidal and harmonic time-dependent field that propagates in the z-axis and is polarized in the x-axis.

By using these assumptions and combining the given equations, it is generated the second orden equation, known as homogeneous Helmholtz vector equation for E.

$$\nabla^2 E + k^2 E = 0 \tag{5}$$

where k is the wave number, which for a lossless medium is expressed as:

$$k = \omega\sqrt{\varepsilon_0\mu_0} = \frac{\omega}{c_0} = \frac{2\pi}{\lambda}\left(\frac{rad}{min}\right) \tag{6}$$

where:

ω is the angular frequency of propagation
ε_0 is the vacuum permittivity
μ_0 is the vacuum permability

Solving (5) yields:

$$\overline{E}(z,t) = \overline{a_x}\varepsilon_0 cos(\omega t - kz) \tag{7}$$

which takes the phasor value:

$$\overline{\varepsilon}(z) = \overline{a_x}\varepsilon_0 e^{-jkz} \tag{8}$$

The following expression can be used to give the phasor vector in sinusoidal form:

$$\overline{E}(z,t) = Re\{\overline{\varepsilon}(z)e^{j\omega t}\} \tag{9}$$

Figure 1 shows the propagation of the electric field in free space, where the given hypotheses have been been taken into account.
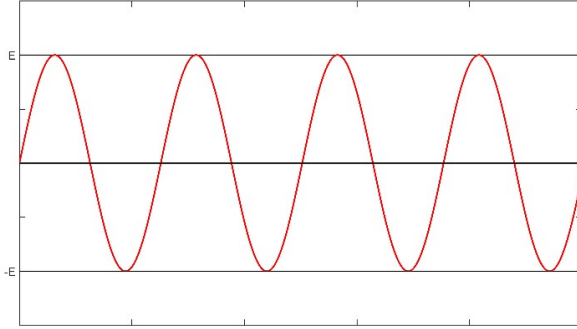
Figure 1. Representation of an electromagnetic wave that travels in free space [11].

1.2. Propagation of the waves in a medium with losses

The hypotheses defined in the preceding sub-section consider the propagation of electromagnetic waves in the vacuum. These are now extended to materials with losses, i.e., conventional materials.

According to their behavior in front of fields, the materials are classified in good conductors, when they allow electric fields pass through them, or as dielectrics, when they store electric energy inside and form polar molecular bonds that are known as electric dipoles. In general, a material has a conducting part and a dielectric part. Their behavior is determined by means of the complex permittivity of the material, which is defined as:

$$\varepsilon_c = \varepsilon' - j\varepsilon'' \tag{10}$$

Where ε' is the dielectric constant of the material, that measures the amount of formed dipolar moments and represents the energy stored in the material, and ε'' is the constant of losses that represents the energy that is not stored in the material, but that is somehow propagated or reflected, which is represented as:

$$\varepsilon'' = \varepsilon_r'' + \frac{\sigma}{\omega} \tag{11}$$

Where σ is the conductivity of the material such that:

$$\overline{J} = \sigma\overline{E} \tag{12}$$

It is obtained an equivalent conductivity that represents all the losses in the medium.

$$\sigma_{eq} = \omega\varepsilon'' \tag{13}$$

The «tangent of losses» is a measure of the power losses in the medium, and is defined as.

$$tan\,\delta = \frac{\varepsilon''}{\varepsilon'} = \frac{\omega\varepsilon'' + \sigma}{\omega\varepsilon'} \tag{14}$$

Therefore, the solution of Maxwell's equations through the homogeneous Helmholtz vector equation for E takes the form:

$$\triangledown^2\overrightarrow{E} + k_c^2\overrightarrow{E} = 0 \tag{15}$$

$$k_c = \omega\sqrt{\varepsilon_c\mu}(m^{-1}) \tag{16}$$

where k_c is the complex wave number, i.e., that takes the complex value of the permittivity of the medium, which behaves in phasor mode when taking a sinusoidal electric field. Besides, the vacuum permittivity is expressed as a real value, since it will have no losses:

$$\varepsilon_0 = 8.854 \times 10^{-12}\frac{F}{m}$$

Therefore, this form of behavior of the materials makes the electromagnetic waves to attenuate at the moment of hitting them; part of the energy will be stored in the polar bonds and part will leave as energy losses. As a result, the concept of propagation constant is defined as:

$$y = \alpha + j\beta = j\omega\sqrt{\mu\varepsilon'}\left(1 + \frac{\sigma}{j\omega\varepsilon}\right)^{\frac{1}{2}} \tag{17}$$

Using the definition of tangential loss:

$$y = \alpha + j\beta = j\omega\sqrt{\mu\varepsilon'}\left(1 - j\frac{\varepsilon''}{\varepsilon'}\right)^{\frac{1}{2}} \tag{18}$$

Where α is the constant of attenuation and β is the constant of phase.

Then, the primary solution given in vacuum is written as:

$$\overline{E}(z,t) = \overline{a_x}\varepsilon_0 cos(\omega t - \beta z) \tag{19}$$

which takes the phasor value:

$$\overline{\varepsilon}(z) = \overline{a_x}\varepsilon_0 e^{-j\beta z} \tag{20}$$

where:

$$\overline{E}(z,t) = Re\{\overline{\varepsilon}(z)e^{j\omega t}\} \qquad (21)$$

Figure 2 shows the representation of this attenuation of an electric field that hits a material with losses.
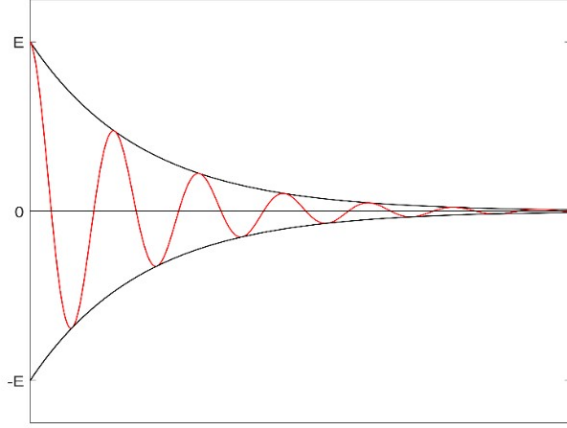
Figure 2. Representation of an electric field that travels in a medium with losses [11].

The energy lost at the moment of the propagation on the material is called this way, because it is stored in the material forming polar bonds; part of this energy is reflected from the material and part goes through it, according to the value of its conductivity. This is seen in Figure 3. It is observed an incident electric field (in green) that collides in the medium (blue lines), and part of it is reflected (in red) and part is propagated by the field (in orange).

All this is quatified in the complex permittivity.

In all this analysis it is assumed that the material is isotropic, i.e., that the dipolar moments or that the polar bonds occur in the direction of the electric field; this does not occur in anisotropic materials, but this analysis is not taken into account in this research, because isotropic AOC have been considered.

The reflected part of the field can be related with respect to the incident field by means of the reflection coefficient Γ, which relates the reflected wave and the incident wave of the field

$$\Gamma = \frac{E_r}{E_i} \qquad (22)$$
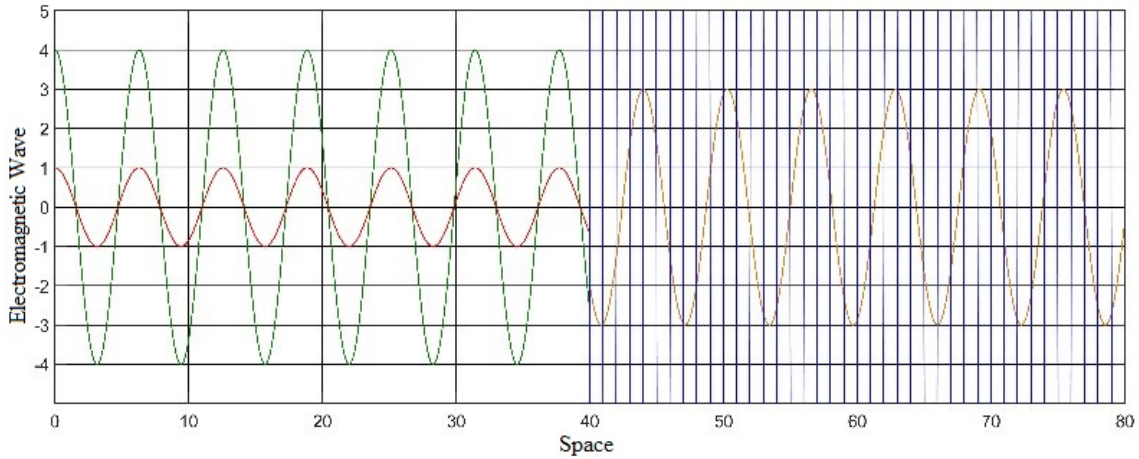
Figure 3. Behavior of the propagation of an electromagnetic wave in front of a change of medium [11].

Replacing the equation of the wave to express it in terms of the electric field, yields:

$$E_r(z) = \Gamma E_0 e^{y_1 z} \alpha_x \qquad (23)$$

The equation of the magnetic field of the propagated and reflected wave is directed in the direction orthogonal to the electric field:

$$H_r(z) = \Gamma \frac{E_0}{n_1} e^{y_1 z}(-a_y) \qquad (24)$$

It is possible to measure the electric field that hits a material, the propagated field and the reflected field, in accordance with the equations given in the theory.

With all this it can be assumed that it is possible to deduce the values of DC that will take the material when analyzing the relationship between these quantities.

1.3. Dielectric properties of the molecule of water

The water is a dielectric, i.e., it contains in its structure polar molecules that form dipolar moments when being in contact with an electric field, and thus a greater amount of water will result in a greater measured DC.

A dry material will have a behavior established according to its molecular structure, and will be normally homogeneous if this structure remains unalter-

able when subject to a temperature increase or when mixed with water. The AOC, due to their shape and properties, have a homogeneous structure. Therefore, their dielectric constant will remain unalterable when moistened. However, a higher moisture will increase the dipolar moment of the mixture due to the water present, which will produce a change in the DC of such mixture due to the increase in water. Therefore, the DC of the mixture will be related with the MC of the AOC, and if the MC and the DC of the mixture can be measured, it will be possible to determine a correlation between them for future prediction and use as a sensing system.

2. Methodology

It was seen in the previous section that it is possible to correlate the value of the MC of the AOC with the DC of the mixture, because the quantity of dipolar moments will increase according to its MC. In addition, it has been theoretically seen that it is possible to determine the DC of the mixture using Maxwell's equations and their solution for media with losses. This section presents the experimental methodology which was followed to determine such correlation.

It should be noted that the field emmited is the field that collides with the material, and the propagated field is the one that goes through the material.

2.1. Materials

The DC uses frequencies in the microwave range for the propagation of the electromagnetic fields; therefore, two aperture antennas are utilized to emit and receive the incident and propagated fields, respectively (see Figure 4).
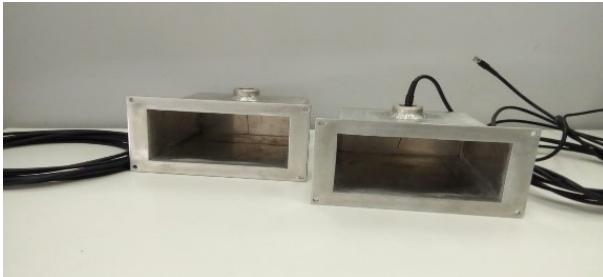
Figure 4. Aperture antennas utilized in MC measuring tests.

A system for analyzing vector signals has been also utilized to emit the electromagnetic field, as it is seen in Figure 5. The phase and amplitude variation of the signal is analyzed, to further determine the DC.

Figure 5. Wavetester equipment for analyzing vector signals.

The analyzer of vector signals utilizes a software for data detection.

A sensing platform has been also constructed to carry out the experimentation, on which the AOC has been placed to measure its DC and its MC. Other utilized materials include: scales, measuring containers, drying oven, etc.

The sample is placed between the receiver and trasnmitting antennas, where it is measured the effect on the AOC of the wave propagating in free space between the two antennas.

2.2. Experimentation

Three Peruvian quarries of AOC have been utilized to perform the calibration of the system: Cerro Mocho, Moyobamba and Sol-Sol. To determine the correlation between MC and DC it has been proceeded the following way:

An initial mass (m_0) has been defined as the total mass of AOC provided by the quarry. Then a thermogravimetric drying has been carried out to obtain the value of dry mass (m_s), i.e., without MC. This value of m_s has been divided into 4, and each of theses samples has been named sampling dry mass and have been numbered from 1 to 4 (m_{smx}), where the subscript x corresponds to the number of the subsample. Then the sample m_{sm1} is selected and placed on the sensing platform, the electromagnetic field is emitted on the material, and with the help of the signal analyzer the value of the DC for m_{sm1} is measured. This value of DC corresponds to the value of 0 % of MC. The mass of water (m_{H_2O}) corresponding to 0.5 % m_{sm1} is added to m_{sm1}, and the same procedure is carried out for measuring its DC. Then 0.5 % m_{sm1} is added again and the DC is measured, which corresponds to 1 % of its MC. This procedure is repeated until reaching 10 % of MC

$$m_{h2O} = 0.005 \times m_{sm1} \tag{25}$$

It should be clarified that the following relationships are met in the experimentation:

$$m_{sm1} = m_{sm2} = m_{sm3} = m_{sm4} \qquad (26)$$

$$m_{sm1} + m_{sm2} + m_{sm3} + m_{sm4} = m_s \qquad (27)$$

The distance between antennas was 23 cm, the thickness of the sample was established in 40 mm, and the frequency of emission of the electromagnetic field was 1.5 GHz.

m_{sm1} and m_{sm2} were utilized to make the curves of correlation, and m_{sm3} and m_{sm4} to validate the results. It should be remarked that, at all times, the DC of the mixture of the moistened AOC is measured.

3. Results

With the values of DC *vs.* MC obtained for each quarry, the calibration curve is fitted by means of linear regression models. In this fit the MC is set as the dependent variable, and the DC as the independent variable with different effects: linear, quadratic, cubic and of fourth order.

The «Stepwise Forward» method was applied for selecting the linear regressiong model, to determine which of the effects of the DC better fits with the MC. This classical method for the selection of variables initiates with an empty model, and in each iteration evaluates incorporating some of the defined effects of the dielectric constant: linear, quadratic, cubic and of fourth order. It is decided to incorporate some of the aforementioned effects if it meets the defined significance level: P Value smaller than 0.05. The «Stepwise Forward» method finalizes when no more effects can be incorporated, because they do not meet the significance level. In order to evaluate the level of significance of the effects, a hypothesis test with «T-Student» is carried out. In this test it is verified if the estimated coefficient of the effect is equal or different than zero.

$$H_0 : b_i = 0 \qquad (28)$$

$$H_1 : b_i \neq 0 \qquad (29)$$

If the null hypothesis is rejected ($b_i \neq 0$), the effect is significant.

In hypothesis contrasting, it is calculated the relationship between the estimated coefficient of the effect (b_i) and its standard deviation (S_{b_i}), and it is compared with the critical t for a confidence level of 95 % ($\alpha = 0,05$).

$$\frac{b_i}{S_{bi}} > j_{N-1}^{\alpha/2} \qquad (30)$$

If the relationship is met, the null hypothesis is rejected. In this condition it is met that the «P value» is smaller than 0.05.

In fitting the regression model it was also found necessary to apply the Cochrane-Orcutt iterative procedure, to correct the autocorrelation present in the data. This autocorrelation is the result of sequentially adding the variation of the moisture, and with this correction the estimation of the parameters is improved.

The results of the tests are presented in the following.

3.1. Cerro Mocho quarry

The model was selected by means of «Stepwise Forward», where it is obtained

$$(CH \%) = -7.372 + 3.206 \times CD \qquad (31)$$

In this model, the linear effect of the dielectric coefficient with respect to the expected value of moisture results significant. Table 1 shows the results of the hypothesis contrasting, where the «P value» of the linear effect is smaller than 0.05. It was obtained a linear regression model of $R^2 = 95.8057$ % and a standard error of 0.382134.

Table 1. Significance of the effect of the variables

Parameter	Estimated value	Standard error	T-Student	P Value
Constant	7.37238	0.378829	19.461	0.000
Dielectric_const	3.2059	0.0740563	43.29	0.000

Figure 6 shows the relationship between the dielectric constant and the moisture; Figure 7 shows the relationship between real and predicted values of moisture.
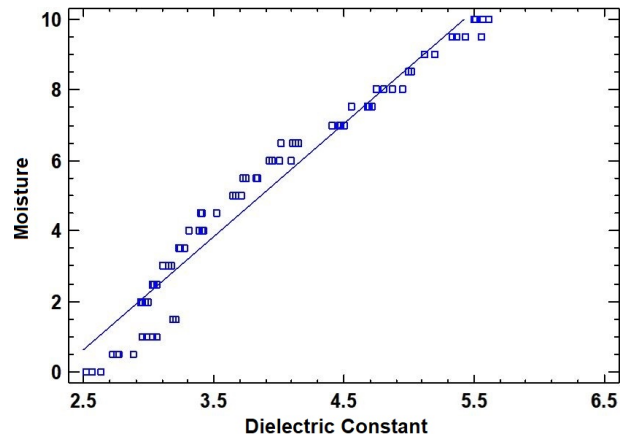
Figure 6. Plot of the fitted model.
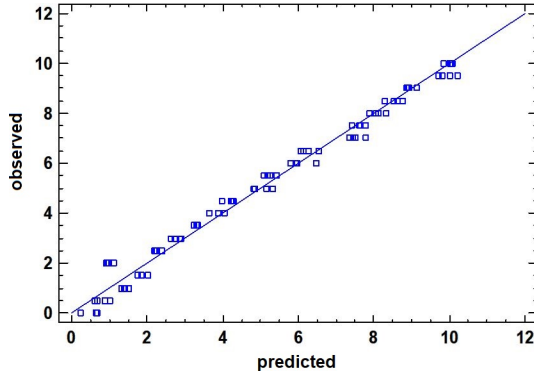
Figure 7. Graphical relationship between observed and predicted values of moisture.

Figure 9. Graphical relationship between observed and predicted values of moisture.

3.2. Moyobamba quarry

The model was selected by means of «Stepwise Forward», where the linear, quadratic and cubic effects of the dielectric constant with respect to the expected value of moisture are significant

$$(CH \%) = 38.55 + 18.15 \times CD - 2.52 \times CD^2 + 0.13 \times CD^3$$

Table 2 shows the results of the hypothesis contrasting, where the «P value» of the effects is smaller than 0.05.

Table 2. Significance of the effect of the variables

Parameter	Estimated value	Standard error	T-Student	P Value
Constant	38.55	1.93216	19.9518	0.000
Dielectric_const	18.1473	1.045	17.3657	0.000
Dielectric_const2	2.52011	0.18239	13.8172	0.000
Dielectric_const3	0.1253	0.0102973	12.1681	0.000

It was obtained a linear regression model of $R^2 =$ 99.5097 % and a standard error of 0.201714.

Figure 8. Plot of the fitted model.

Figure 8 shows the relationship between the dielectric constant and the moisture; Figure 9 indicates the relationship between real and predicted values of moisture.

3.3. Sol-Sol quarry

The model was selected by means of «Stepwise Forward».

$$(CH \%) = -15.5262 + 7.26581 \times CD - 0.506717 \times CD^2 \quad (32)$$

Where the linear and quadratic effects of the dielectric constant with respect to the value of moisture resulted significant. Table 3 shows that the «P value» of the effects is smaller than 0.05.

Table 3. Significance of the effect of the variables

Parameter	Estimated value	Standard error	T-Student	Valor P
Constant	-15.5262	0.875589	17.7323	0.000
Dielectric_const	7.26581	0.41318	17.5869	0.000
Dielectric_const2	0.506717	0.0477948	10.6011	0.000

It was obtained a linear regression model of $R^2 =$ 97.1325 % and a standard error of 0.297068.

Figure 10 shows the relationship between the dielectric constant and the moisture, while Figure 11 shows the relationship between real and predicted values of moisture.
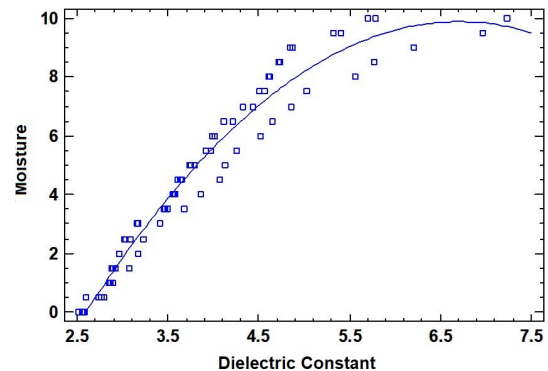
Figure 10. Plot of the fitted model.
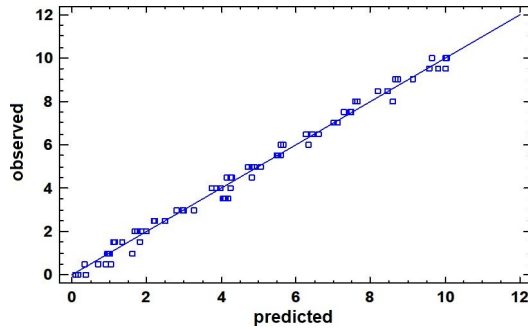
Figure 11. Graphical relationship between observed and predicted values of moisture.

4. Discussion of results

From the results obtained in the previous section, it is interesting to see that in the frequency of 1.5 GHz, the linear regression correlations maintain an $R^2>95$ %, as seen in Table 4.

Table 4. Comparison of results

Cantera	R^2	Error estándar
Cerro Mocho	95.8057	0.382134
Moyobamba	99.5097	0.201714
Sol-Sol	97.1325	0.297068

It can be also seen that there is a direct relationship between the MC and the DC, i.e., a greater MC results in a larger value of DC.

Comparing the equations for predicting the MC, it can be observed that, depending on the origin of the AOC, it is defined its calibration curve, which can vary between linear, quadratic or cubic; hence, for practical purposes, the AOC should be first calibrated according to a specific quarry before carrying out the measurement and this curve cannot be used for another quarry, since the values of DC differ between quarries. This was expected because the DC depends on the molecular properties and on the energy storage capacity, which means that each AOC has a different structure at a molecular level.

5. Conclusions

The measurement of MC with devices that utilize microwaves has advantages over invasive methods, because they do not damage the material. The measurement of the DC with this methodology analyzes internally the behavior of the material to define its DC, since it studies the dipolar moments formed when electromagnetic fields are induced in the material. It can be used in the presence of vapors or in dirty environments, while the AOC is not molecularly changed, since these do not interfere with the microwave signals. Therefore, the DS enables the measurement of a broad

range of materials, whether they are solids, gases or liquids.

The measurement is carried out without contact with the material. The method is not invasive nor destructive. The meaurement is carried out in real time and online with the process.

It is interesting to observe the relationship found by different authors. In [17] the author defines a linear or polynomial relationship. The parameters that influence the calculation of the dielectric constant, and the relationship between the moisture content and the temperature are shown.

It has been verified that with the methodology based in DS at 1.5 GHz, linear correlation values of high precision ($R^2>95$ %) are obtained for each of the quarries. The system has been validated in a horizontal conveyor with fine aggregate and antennas arranged vertically.

The results obtained show the relationship between the MC and the DC in AOC, and it has been observed a variation in the calibration curve between different quarries.

This sensing system exhibits a high potential to be used for measuring the MC in AOC, in the process of concrete production.

Acknowledgements

References

[1] J. B. Hasted and M. A. Shah, "Microwave absorption by water in building materials," *British Journal of Applied Physics*, vol. 15, no. 7, pp. 825–836, jul 1964. [Online]. Available: https://doi.org/10.1088%2F0508-3443%2F15%2F7%2F307

[2] A. Cataldo, E. De Benedetto, and G. Cannazza, "Hydration monitoring and moisture control of cement-based samples through embedded wire-like sensing elements," *IEEE Sensors Journal*, vol. 15, no. 2, pp. 1208–1215, 2015. [Online]. Available: https://doi.org/10.1109/JSEN.2014.2360712

[3] F. P. Balobey, "Optimalisation of microwave method for moisture content measurement in asbestos-cement sheets," *Russian: Oborudovanye Prom. Story. Meter, Instrum. for Build. Mater*, vol. 1, pp. 44–50, 1964.

[4] A. W. Kraszewski, "Microwave aquametry-needs and perspectives," *IEEE Transactions*

on Microwave Theory and Techniques, vol. 39, no. 5, pp. 828–835, 1991. [Online]. Available: https://doi.org/10.1109/22.79110

[5] A. Kraszewski, "Microwave aquametry–a bibliography," *Journal of Microwave Power*, vol. 15, no. 4, pp. 298–310, 1980. [Online]. Available: https://doi.org/10.1080/16070658.1980.11689215

[6] V. Komarov, *Handbook of Dielectric and Thermal Properties of Materials at Microwave Frequencies*. Artech House, 2012. [Online]. Available: https://bit.ly/2WQE2Tv

[7] A. Cownie and L. S. Palmer, "The effect of moisture on the electrical properties of soil," *Proceedings of the Physical Society. Section B*, vol. 65, no. 4, pp. 295–301, apr 1952. [Online]. Available: https://doi.org/10.1088%2F0370-1301%2F65%2F4%2F308

[8] J. J. Windle and T. M. Shaw, "Dielectric properties of wool–water systems. ii. 26 000 megacycles," *The Journal of Chemical Physics*, vol. 25, no. 3, pp. 435–439, 1956. [Online]. Available: https://doi.org/10.1063/1.1742941

[9] A. Nakanishi, T. Hori, and J. Fujiwara, "An evaluation of"moister"as a measuring apparatus of the moisture content of paper," *Japanese: Res. Inst. Techn. Bull*, vol. 1, pp. 9–20, 1955.

[10] A. Yasukawa, "Measurement and automatic control of moisture content in rayon pulp: Soc. of instrum," *Technol. Japan J*, vol. 6, no. 8, pp. 386–391, 1956.

[11] R. Rodríguez Arisméndiz, "Estudio de la espectroscopía dieléctrica para la medición del contenido de humedad en productos alimenticios," Ph.D. dissertation, 2017. [Online]. Available: https://hdl.handle.net/11042/3487

[12] M. Berliner and S. A. Polishchuk, "Instrument for moisture content measurement in slurries," *Russian: Cement*, pp. 14–15, 1978.

[13] D. K. Cheng, *Fundamentos de electromagnetismo para ingeniería*. Pearson Educación, 1997. [Online]. Available: https://bit.ly/3cvOXIP

[14] A. R. Dean and P. Bridle, "Test on the use of a microwave moisture meter," *Timber Trade J.*, vol. 27, pp. 50–52, 1969.

[15] D. F. Tirado, P. M. Montero, and D. Acevedo, "Estudio Comparativo de Métodos Empleados para la Determinación de Humedad de Varias Matrices Alimentarias," *Información tecnológica*, vol. 26, pp. 03–10, 00 2015. [Online]. Available: http://dx.doi.org/10.4067/S0718-07642015000200002

[16] G. R. Oetzel, F. P. Villalba, W. J. Goodger, and K. V. Nordlund, "A comparison of on-farm methods for estimating the dry matter content of feed ingredients1," *Journal of Dairy Science*, vol. 76, no. 1, pp. 293–299, 1993. [Online]. Available: https://doi.org/10.3168/jds.S0022-0302(93)77349-X

[17] L. Jílková, T. Hlinčík, and K. Ciahotný, "Determination of water content in pyrolytic tars using coulometric karl-fischer titration," *Journal of Advanced Engineering*, vol. 57, no. 1, pp. 8–13, 2017. [Online]. Available: http://dx.doi.org/10.14311/AP.2017.57.0008

[18] A. M. Helmenstine, "What is distillation? chemistry definition," *ThoughtCo*, 2019. [Online]. Available: https://bit.ly/2WLgTli

[19] L. M. L. Nollet, *Handbook of Food Analysis: Physical characterization and nutrient analysis*, ser. Food Science and Technology - Marcel Dekker, Inc. CRC PressI Llc, 2004. [Online]. Available: https://bit.ly/3fMQrAI

[20] G. S. Campbell and C. S. Campbell, "Water content and potential, measurement," in *Reference Module in Earth Systems and Environmental Sciences*. Elsevier, 2013. [Online]. Available: https://doi.org/10.1016/B978-0-12-409548-9.05333-1

[21] M. R. Goyal, *Management of Drip/Trickle or Micro Irrigation*. Apple Academic Press, 2012. [Online]. Available: https://bit.ly/2yJGaVl

[22] T. Reyna, J. Linares, M. Lábaque, and S. Reyna, "Métodos para medir el contenido de humedad vs. el tiempo. estudios de infiltración. evaluación de resultados de campo," in *XXVII Congreso Latinoamericano de Hidráulica, Lima Perú*, 09 2016. [Online]. Available: https://bit.ly/3dIYexC

[23] S. Jiménez, L. Scarioni, and H. Kelim, "Nota técnica: Sensores de humedad de tipo capacitivo y resistivo, fabricados con NaCl, KBr y KCl," *INGENIERIA UC*, vol. 20, no. 1, pp. 83–86, 04 2013. [Online]. Available: https://bit.ly/2Wrj2Uv

[24] S. Okamura, "Microwave technology for moisture measurement," *Subsurface Sensing Technologies and Applications*, vol. 1, no. 2, pp. 205–227, 2000. [Online]. Available: https://bit.ly/2WWETC6

[25] E. Pinos-Vélez, S. Encalada, E. Gamboa, V. Robles-Bykbaev, W. Ipanque, and C. L. Chacón, "Development of a support system for the presumptive diagnosis of glaucoma through the processing of biomedical images of the human eye fundus in ecuador," in *Advances in Human Factors and Ergonomics in Healthcare and Medical Devices*, V. Duffy and

N. Lightner, Eds. Cham: Springer International Publishing, 2018, pp. 100–109. [Online]. Available: https://doi.org/10.1007/978-3-319-60483-1_11

[26] J. Soto, E. Paiva, W. Ipanaqué, J. Reyes, D. Espinoza, and D. Mendoza, "Cocoa bean quality assessment by using hyperspectral index for determining the state of fermentation with a nondestructive analysis," in *2017 CHILEAN Conference on Electrical, Electronics Engineering, Information and Communication Technologies (CHILECON)*, 2017, pp. 1–5. [Online]. Available: https://doi.org/10.1109/CHILECON.2017.8229718

[27] J. M. Ruiz Reyes, J. Soto Bohorquez, and W. Ipanaque, "Evaluation of spectral relation indexes of the peruvian's cocoa beans during fermentation process," *IEEE Latin America Transactions*, vol. 14, no. 6, pp. 2862–2867, 2016. [Online]. Available: https://doi.org/10.1109/TLA.2016.7555266

[28] J. Soto, J. Ruiz, W. Ipanaqué, and C. Chinguel, "New hyperspectral index for determining the state of fermentation in the non-destructive analysis for organic cocoa violet," in *2016 IEEE International Conference on Automatica (ICA-ACCA)*, 2016, pp. 1–6. [Online]. Available: https://doi.org/10.1109/ICA-ACCA.2016.7778387

[29] J. Soto, G. Granda, F. Prieto, W. Ipanaque, and J. Machacuay, "Cocoa bean quality assessment by using hyperspectral images and fuzzy logic techniques," in *Twelfth International Conference on Quality Control by Artificial Vision 2015*, F. Meriaudeau and O. Aubreton, Eds., vol. 9534, International Society for Optics and Photonics. SPIE, 2015, pp. 152–158. [Online]. Available: https://doi.org/10.1117/12.2182598

[30] A. W. Kraszewski and S. O. Nelson, "Microwave resonator technique for moisture content and mass determination in single soybean seeds," *IEEE Transactions on Instrumentation and Measurement*, vol. 43, no. 3, pp. 487–489, 1994. [Online]. Available: https://doi.org/10.1109/19.293475

[31] P. G. Bartley, S. O. Nelson, R. W. McClendon, and S. Trabelsi, "Determining moisture content of wheat with an artificial neural network from microwave transmission measurements," *IEEE Transactions on Instrumentation and Measurement*, vol. 47, no. 1, pp. 123–126, 1998. [Online]. Available: https://doi.org/10.1109/19.728803

[32] K.-B. Kim, J.-H. Kim, S. S. Lee, and S. H. Noh, "Measurement of grain moisture content using microwave attenuation at 10.5 ghz and moisture density," *IEEE Transactions on Instrumentation and Measurement*, vol. 51, no. 1, pp. 72–77, 2002. [Online]. Available: https://doi.org/10.1109/19.989904

[33] M. Ben Slima, R. Z. Morawski, A. W. Kraszewski, A. Barwicz, and S. O. Nelson, "Calibration of a microwave system for measuring grain moisture content," *IEEE Transactions on Instrumentation and Measurement*, vol. 48, no. 3, pp. 778–783, 1999. [Online]. Available: https://doi.org/10.1109/19.772221

[34] S. Trabelsi and S. O. Nelson, "Free-space measurement of dielectric properties of cereal grain and oilseed at microwave frequencies," *Measurement Science and Technology*, vol. 14, no. 5, pp. 589–600, mar 2003. [Online]. Available: https://doi.org/10.1088%2F0957-0233%2F14%2F5%2F308

[35] C. V. K. Kandala, "Moisture determination in single peanut pods by complex rf impedance measurement," *IEEE Transactions on Instrumentation and Measurement*, vol. 53, no. 6, pp. 1493–1496, 2004. [Online]. Available: https://doi.org/10.1109/TIM.2004.834058

[36] Z. Abbas, You Kok Yeow, A. H. Shaari, K. Khalid, J. Hassan, and E. Saion, "Complex permittivity and moisture measurements of oil palm fruits using an open-ended coaxial sensor," *IEEE Sensors Journal*, vol. 5, no. 6, pp. 1281–1287, 2005. [Online]. Available: https://doi.org/10.1109/JSEN.2005.859249

[37] S. Trabelsi and S. O. Nelson, "Influence of nonequilibrated water on microwave dielectric properties of wheat and related errors in moisture sensing," *IEEE Transactions on Instrumentation and Measurement*, vol. 56, no. 1, pp. 194–198, 2007. [Online]. Available: https://doi.org/10.1109/TIM.2006.887314

[38] K. Tsukada and T. Kiwa, "Magnetic measurement of moisture content of grain," *IEEE Transactions on Magnetics*, vol. 43, no. 6, pp. 2683–2685, 2007. [Online]. Available: https://doi.org/10.1109/TMAG.2007.892853

[39] C. V. K. Kandala and S. O. Nelson, "Rf impedance method for estimating moisture content in small samples of in-shell peanuts," *IEEE Transactions on Instrumentation and Measurement*, vol. 56, no. 3, pp. 938–943, 2007. [Online]. Available: https://doi.org/10.1109/TIM.2007.894796

[40] C. V. Kandala and N. Puppala, "Parallel-plate capacitance sensor for nondestructive measurement of moisture content of different types of wheat," in *2012 IEEE Sensors Applications Symposium*

Proceedings, 2012, pp. 1–5. [Online]. Available: https://doi.org/10.1109/SAS.2012.6166325

[41] S. T. Wahyuni Siregar, W. Handayani, and A. H. Saputro, "Bananas moisture content prediction system using visual-nir imaging," in *2017 5th International Conference on Instrumentation, Control, and Automation (ICA)*, 2017, pp. 89–92. [Online]. Available: https://doi.org/10.1109/ICA.2017.8068419

Rapid prototyping in the manufacture of 3D printed molds for plastic blowing

Prototipado rápido en la fabricación de moldes impresos en 3D para soplado de plástico

Gilberto Carrillo[1,*], Carolina Nuila[2], Jorge Laínez[3]

Abstract

In the Salvadoran industry, we can find entrepreneurs and microentrepreneurs who do not have the resources to make plastic bottles with stylized designs that differentiate them from other brands and products, which prevents them from escalating to other market segments or international markets, slows the growth of their business. One possible cause is that the manufacture of blow molds requires a very expensive initial investment. However, there are alternatives such as the manufacture of low-run molds, which have lower resolution and shorter life time, but, at the same time, offer as a benefit a lower manufacturing cost and, therefore, lower acquisition cost for the entrepreneur, opening in this way the opportunity to be able to produce stylized bottles at convenience. Among the various ways to manufacture low-run molds, there is the reverse engineering technique, which requires rapid prototyping equipment. This article describes the reverse engineering procedure to generate the mold for blowing. With the available design the necessary mold was printed and with this, the bottles were manufactured, which were scanned to verify with computer program their dimensions comparing them against the original mold file. Simultaneously, the containers were verified in the industrial metrology laboratory to validate the computer results, these results are presented in the document.

Keywords: Mold for blowing, 3D printing, rapid prototyping, plastic bottles.

Resumen

En la industria salvadoreña pueden encontrarse empresarios y microempresarios que no tienen los recursos para fabricar botellas de plástico con diseños estilizados que los diferencien de otras marcas y productos, lo que les impide escalar a otros segmentos de mercado o mercados internacionales, frenando el crecimiento de sus negocios. Una posible causa es que la fabricación de moldes de soplado requiere una inversión inicial muy costosa. Sin embargo, existen alternativas como la fabricación de moldes de bajo rendimiento, que tienen una resolución más baja y un tiempo de vida más corto, pero, al mismo tiempo, ofrecen como beneficio un menor costo de fabricación y, por lo tanto, un menor costo de adquisición para el empresario, posibilitando la producción de botellas estilizadas a conveniencia. Entre las diversas formas de fabricar moldes de bajo rendimiento está la técnica de ingeniería inversa, que requiere un equipo de creación rápida de prototipos. Este artículo describe el procedimiento de ingeniería inversa para generar el molde para soplado. Con el diseño disponible se imprimió el molde necesario y con esto se fabricaron las botellas, que se escanearon para verificar con el programa de computadora sus dimensiones comparándolas con el archivo original del molde. Simultáneamente, los contenedores se verificaron en el laboratorio de metrología industrial para validar los resultados de la computadora, estos resultados se presentan en el documento.

Palabras clave: molde para soplado, impresión 3D, creación rápida de prototipos, botellas de plástico.

[1,*]Centro de Innovación en Diseño Industrial y Manufactura, Universidad Don Bosco, El Salvador. Corresponding author ✉: gilberto.carrillo@udb.edu.sv. ⓘ http://orcid.org/0000-0002-9845-1381

[2]Laboratorio de Metrología, Universidad Don Bosco, El Salvador. ⓘ http://orcid.org/0000-0002-7626-389X

[3]Herramientas Centroamericanas S. A. de C. V., El Salvador. ⓘ http://orcid.org/0000-0001-7940-5366

1. Introduction

The manufacturers of plastic containers and the Salvadoran entrepreneurs cannot acquire new steel and aluminum alloy molds for new products, since it requires a high initial investment that can only be amortized with the high production of products [1]. As an example, the metal versions of the bottle blow mold can cost from US$ 2,000 up to US$ 5,000, which regionally manufactured can be received between 30 and 60 days and manufactured in Europe or North America can be received from 90 to 150 days [2]. This implies that the micro, small and medium-sized Salvadoran companies with low profit margins cannot incorporate new products with differentiated plastic containers in their offer.

As alternative solution for molds, 3D printing becomes a "disruptive technological innovation driven by the flexibility it provides and the potentially favorable economics" [3]. Another applications of printed molds are used for hand-manufacturing composite parts [4]], manufacturing plastic parts [5], develop low-cost wax injection mold [6]. Whereas it alters traditional manufacturing approaches and promotes the expansion of rapid prototyping and digital manufacturing technologies.
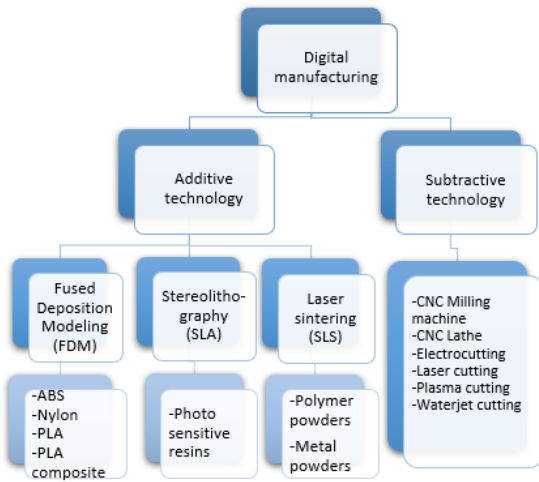
Figure 1. Digital manufacturing techniques.

Digital manufacturing technologies can be classified into additives such as 3D printing and subtractive as cutting equipment with CNC controls (computerized numerical control), as shown in Figure 1.

There are practices in the United States and Europe, where they use additive technologies such as SLA (Stereolithography) and SLS (Selective Laser Sintering) in the manufacture of molds by injection [7]. These technologies are high investment and useful in small-scale production.

To the knowledge of the authors the technique FDM (Fused Deposition Modeling) has been used lit-

tle in the manufacture of molds. This work presents the manufacture of a mold by means of rapid prototyping and low investment FDM technology, with which containers with stylized designs are produced for each need.

2. Materials and Methods

Considering the modeling techniques, the mold generation methods could be classified in reverse engineering and CAD process (Computer Aided Design), represented in Figure 2 and described as 5 stages.

Applying reverse engineering, we scanned a container provided by the industry from which the mold was obtained for study.
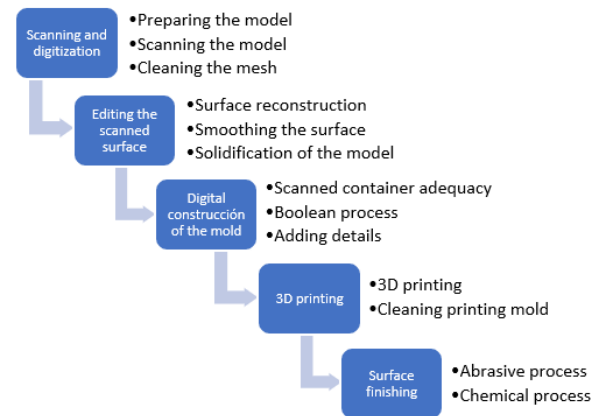
Figure 2. Stages of rapid prototyping applied.

In stage 1, the SmartScan R2-C2 scanning and scanning equipment with an accuracy of 0.01 mm and its Optocat 2015®software was used. The developer liquid is CANTESCO D101-A to attenuate the brightness and reflection of the surfaces to be scanned. The scanning procedure is in accordance with the user manual OPTOCAT version 2015R2 [8].

The temperature of the rapid prototyping room was kept in stable conditions (24 oC) and the entrance of light from outside was reduced less than 25% of the live image illuminated to avoid noise in the scanned images due to the light variations. The final cloud of points is saved in a file with STL format (Standard Triangle Language), to work then in other software.

During stage 2, the edition of the scanned surface was done with the treatment of the point cloud, using the CAD software GeoMagic Design X. The generated file was saved in STEP format (Standard for the Exchange of Product Data) which prevents the loss of design information.

For stage 3, the mold construction was carried out with Inventor software. Was incorporated block dimensions, alignment holes, thread, air exhaust holes, nozzle design.

Within stage 4, the material used in the 3D printing of the blow molds was ABS-plus (acrylonitrile styrene butadiene P430XL), the support material is SR-30XL (soluble support), the bottles material is PET (polyethylene terephthalate). Likewise, 3D printing process was done according with the user manual of the uPrint SE Plus printer, the software used is called CatalystEX and the system of elimination of support is the WaveWash equipment that works by means of ultrasonic washing [9]. The mold was used in the POLIFLEX company to manufacture 25 test bottles. With this first run the recommendations that make up stage 5 arise.

In stage 5 the surface finishes of the mold were made with automotive putty in the cavity where the container is formed. The manual sanding was carried out with sandpaper 1000 to improve the surface smoothness that facilitates the sliding of the PET during the blow.

Outside the reverse engineering process, the containers were scanned for comparison by software, and tests were performed in the industrial metrology laboratory to validate the software results.

3. Results and Discussion

In this section the results are presented in the order of blocks shown in Figure 2.

Stage 1. A cloud of points was obtained from the scan and digitization process, as shown in Figure 3. It was not necessary to scan the container's nozzle, since in the later stage of digital construction the nozzle design was incorporated. according to the blower machine. The possibility of change of nozzle in the mold occurs when planning to produce containers with machines that require preforms.
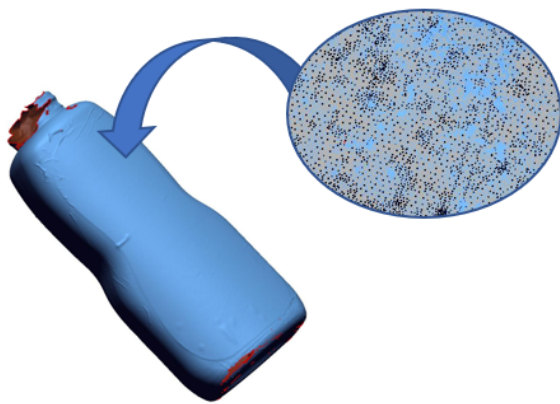
Figure 3. Nube de puntos del recipiente con formato STL, resultante del proceso de escaneado 3D y de escaneado y listo para ser procesado con software CAD.

Stage 2. The scanned surface edition consists of the set of operations to obtain a smoothed body, like cutting, merge, repair, smooth surfaces and borders. The STL file can be improved with any CAD software. The final bottle is shown in Figure 4, and can incorporate characteristic final details such as additional forms, areas for labeling, texts and logos in high and low relief, etc.
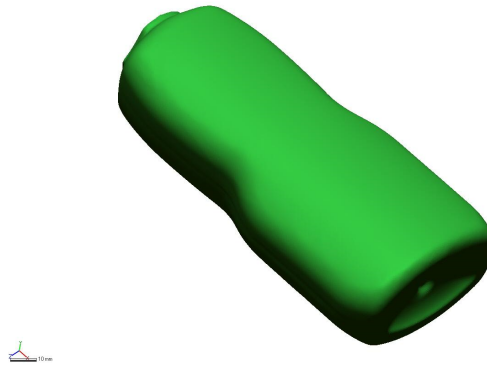
Figure 4. Bottle smoothed by computer and finished.

Stage 3. The digital construction of the mold consists in transforming the bottle from the previous stage (stage 2) to solid in the CAD. The solid body in the shape of a half bottle is joined by means of a process of cutting solid objects in the CAD software and later the details of the mold are added, for example, the fixing holes, threads, exhaust holes and nozzle spaces.

Some important considerations foreseen in the digitization of the mold, and that influence the quality of the products are:

- There were no defects in the overlapping of the container and mold block volumes.

- The thickness of the surfaces at the edges allowed to resist the loads received.

- The curvatures of the geometries and the surfaces are correct to reduce the stress concentration.

- The alignment of holes, pins, surfaces and edges were indicated to avoid unevenness in the surfaces of manufactured products [10].

- The tolerances of holes were correct so that both parts could be coupled during the production of containers with a sliding fit [11].

- The dimensions of the air exhaust were adequate so that no marks are seen in the manufactured containers.
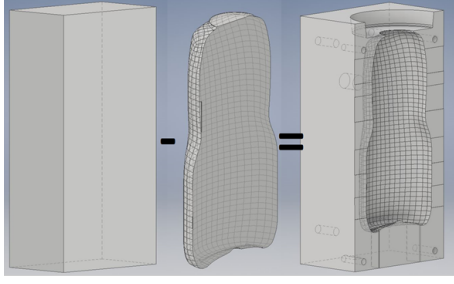
Figure 5. Sequence of processes for mold manufacturing: The solid body in the shape of a half bottle is joined by means of a process of cutting solid objects in the CAD software and later the details of the mold are added, for example, the fixing holes, vents and nozzle spaces.

The nozzle depends on the type of machine where the mold will be installed and the type of raw material. For example, the nozzle of the blow molding machine forms the external thread and uses granulated material, while the nozzle of the preform machine is smooth because it receives the preforms with its already manufactured thread. With this information a nozzle was drawn to the mold as shown in Figure 5.

The molds were designed with a removable bottom, which should be removed during the demolding of the container and installed during the closure of the mold. Its function is to evacuate the air during the blowing and form the bottom of the container to provide stability of it while remaining on flat horizontal surfaces.

The designed mold was analyzed by means of a computer with CAE Inventor software (Computer Aided Engineering), applying a pressure of 350 psi in the curved surfaces which is the blowing pressure for the manufacture of bottles. The results are shown in Figure 6, it is observed that could be an average deformation of 0.66 mm represented by the green area, and a maximum deformation of 1.026 mm at the bottom of the mold represented by the red area.
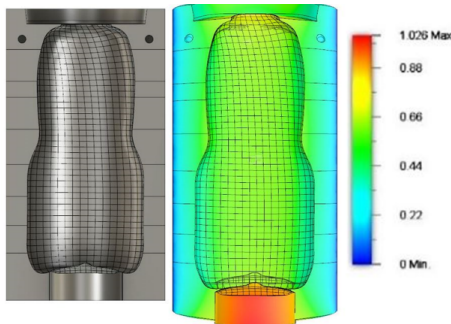
Figure 6. Critical points of the deformation of the mold, considering the points of concentration of efforts calculated by the software and shown in the color palette. The simulated charge pressure was 350 psi, analysis temperature 100 °C, and the units for deformation shown in the color scale in millimeters.

Stage 4. ABS was used as printing material, Figure 7. The height of the printing layers is 0.25 mm, shell thickness of outer surface 10 mm, infill density 100% in the wall, infill density in the middle 60%, top/bottom thickness solid layers 10 mm, with the uPrint SE plus equipment, which generates low resolution curved surfaces. This is difficult when you need smooth bottles, while for stylized designs with rough surfaces is an advantage. In our case the bottom of the mold was printed as part of one of the halves and although it showed some interference in the demolding, it affected 2 bottles of 25 so we considered that it had no negative effect during the manufacturing.
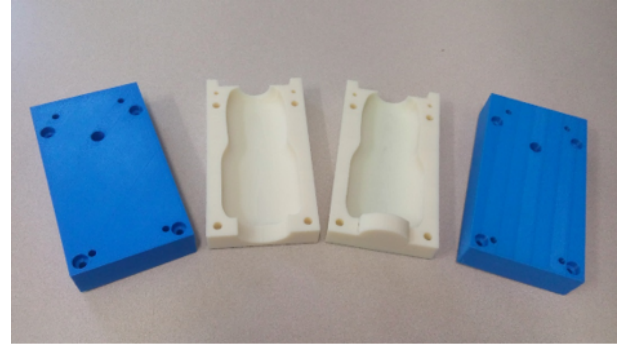
Figure 7. Blow molds for bottles printed in ABS.

The mold for blowing bottles is shown in Figure 7. The 3D printing mold includes ABS material and support material of suppliers in El Salvador, Table 1 shows 3D printing costs. The main cost is about materials and designer time, the cost of materials can be reduced when uses a open source 3D printer, and allows research about new 3D printing materials with better mechanical properties. The working time in CAD can be optimized practicing to improve skills.

Table 1. Cost of 3D printed molds, using prices of existing materials in the Salvadoran market

Cost of 3D printing mold		
Printing material (cubic centimeters)	552.48	
Support material (cubic centimeters)	227	
Printing material, cm^3 (unit cost)	$ 0.42	
Support material, cm^3 (unit cost)	$ 0.42	
Total cost printing material	$ 232.04	$ 232.04
Total cost support material	$ 95.34	$ 95.34
Cost of energy for printing	$ 0.86	
Amortization per hour	$ 2.65	
Printing time (hours)	12	
Power (kilowatts)	1.5	
Amortization during printing	$ 3.98	
Tax (IVA, El Salvador)	13%	
Total cost energy	$ 21.98	$ 21.98
Design/configuration (hours)	14	
Design/configuration (unit cost)	$ 10.00	
Total cost design/configuration	$ 140.00	$ 140.00
Total cost of 3D printing mold		$ 489.36

Figure 8. Plastic bottles made with the use of printed molds.

Figure 9. Digital verification of the dimensions of the containers produced with the printed mold together with its color palette.

With printed mold, 25 containers were obtained in a production company, the mold was installed in one of its blowing machines and bottles were produced as shown in Figure 8. The mold and the bottles were verified with the help of the scanner, determining that they are in good dimensional conditions. It is considered that the surfaces of interest to evaluate are those that supported the pressure of the preforms during the blowing operation and the surfaces that supported the closing pressure of the machine.

The bottles were scanned and compared to the design of the mold in CAD format. Figure 9 shows the points of the digitally verified containers, based on the critical points resulting from the CAE Inventor analysis of the mold in Figure 6. In general terms, the dimensions of the containers are in the range of a tenth and a half millimeter above the average dimensions, and three tenths of a millimeter below the average.

The colors blue, light blue, green and yellow in Figure 9 denote minimum deviations of the scanned model with respect to the digital model, so it is verified that the manufactured bottles are kept in the ranges of +0.15 and -0.2 mm. The measurement results obtained with digital technique are shown in Table 2. Brown color denotes high positive/negative deviation and yellow color indicates low positive/negative deviation from the average dimensions, the dimensions are A=168.168 mm (high), B=61.130 mm (upper width), C=72.610 mm (lower width), D=41.518 mm (higher depth), E=43.049 (lower depth).

The containers were analyzed in the metrology laboratory to verify hermeticity, dimensions and weight [12]. The verification points and part of the equipment used are shown in Figure 10, and Table 3 shows an extract of the determined average and extreme values. Similarly, Table 4 presents an extract of the determined weights, indicating the extreme and average values. It is important to note that none bottle presents leaks after being tested with water.

Table 2. Results of the difference of measurements between the produced containers and the printed mold

Bottle number	Point 1	Point 2	Point 3	Point 4	Point 5	Point 6
1	0.0723	0.1644	0.0917	0.0881	-0.1216	0.0280
2	0.1439	0.1445	0.0832	0.0277	-0.0110	0.0636
3	0.1182	0.1125	0.0790	0.0624	-0.0580	0.0896
4	0.0175	0.1001	0.1109	0.0551	-0.0569	0.3939
5	0.0784	0.0383	0.0622	0.1062	-0.1231	0.0720
6	0.1094	0.0512	0.0196	0.1632	-0.2330	-0.0138
7	0.0704	0.1229	0.0094	0.1078	-0.2044	0.0223
8	0.0869	0.1268	0.0843	0.1458	-0.2595	-0.1917
9	0.1063	0.0729	0.0508	0.1260	-0.1681	-0.0795
10	0.1126	0.0972	0.0793	0.1312	-0.3859	-0.2118
11	0.1419	0.1103	0.1031	0.1056	-0.2024	-0.0397
12	0.1232	0.1455	0.1077	0.0906	-0.3409	-0.1720
13	0.1664	0.1377	0.1204	0.1109	-0.1183	-0.0979
14	0.1471	0.1288	0.0862	0.0909	-0.2086	-0.2159
15	0.1109	0.1257	0.0665	0.1428	-0.1994	-0.0293
16	0.1072	0.0673	0.0558	0.1033	-0.3444	-0.1224
17	0.1411	0.0258	0.0120	0.0973	-0.3811	-0.1013
18	0.1465	0.0938	-0.0205	0.1325	-0.3631	-0.0562
19	0.1019	0.0603	-0.0090	0.1041	-0.3061	-0.0247
20	0.1286	0.0966	0.0455	0.1397	-0.1682	-0.0201
21	0.1182	0.1136	-0.0018	0.1095	-0.2294	-0.0770
22	0.0677	0.1241	0.0256	0.1068	-0.1644	-0.0080
23	0.1159	0.1199	0.0478	0.1164	-0.1837	-0.0226
24	0.1147	0.1887	0.0476	0.1233	-0.1654	-0.0870
25	0.0905	0.1295	0.0803	0.0793	-0.2773	-0.0214

The verification team used 3D scanner and the GeoMagic software.

Table 3. Reference diagram for the dimensional analysis and execution of dimensional tests with the dimensions A high, B upper width, C lower width, D higher depth, E lower depth.

Results of the verification of the 25 bottles (mm)										
Dimension	A		B		C		D		E	
Vref	168.168		61.130		72.610		41.518		43.049	
ID of the bottle	Average Value Vm	Error Vm - Vref	Average Value Vm	Error Vm - Vref	Average Value Vm	Error Vm - Vref	Average Value Vm	Error Vm - Vref	Average Value Vm	Error Vm - Vref
1	168.160	0.008	61.073	0.057	73.038	-0.027	41.335	0.182	42.941	0.107
2	168.219	-0.051	61.075	0.056	73.003	0.007	41.250	0.267	42.907	0.142
3	168.148	0.020	61.098	0.032	72.986	0.024	41.167	0.351	42.979	0.069
4	168.173	-0.005	61.089	0.041	72.981	0.029	41.335	0.183	42.980	0.069
5	168.268	-0.100	61.082	0.049	72.993	0.017	41.315	0.203	42.978	0.070
12	168.162	0.006	61.137	-0.007	73.000	0.011	41.758	-0.240	42.990	0.059
15	168.148	0.020	61.131	-0.001	73.041	-0.030	41.527	-0.009	43.151	-0.103
18	168.139	0.029	61.173	-0.042	73.051	-0.041	41.604	-0.087	43.109	-0.060
24	168.044	0.124	61.182	-0.052	72.986	0.024	41.669	-0.152	43.120	-0.072

Table 4. Weight measurement results of the 25 containers

Results of the verification of the 25 bottles (g)		
Wref		283.538
ID of the bottle	Average value Wm	Error Wm - Wref
1	283.194	-0.0345
2	286.626	0.3087
5	283.559	0.0021
7	283.558	0.0020
8	283.555	0.0016
9	283.557	0.0018
22	283.289	-0.0249
23	283.252	-0.0287
24	283.236	-0.0302
25	283.202	-0.0336

The results in orange are the highest deviations above the average and in yellow the greater deviations below the average. The values Wm in grams.
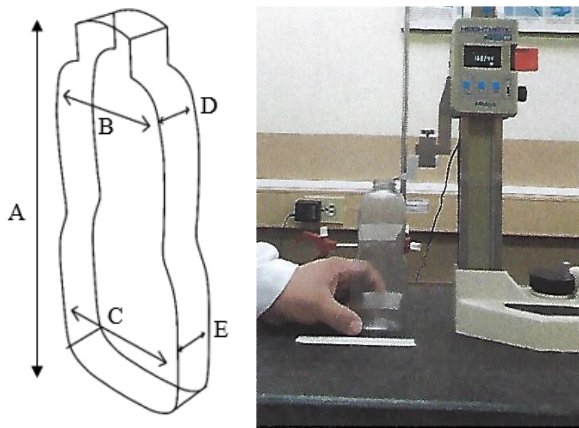
Figure 10. Reference diagram for the dimensional analysis and execution of dimensional tests with the dimensions A high, B upper width, C lower width, D higher depth, E lower depth.

Stage 5. To improve the surface finish, automotive putty was applied to the mold and smoothed with 1000 grade sandpaper, which achieved a smooth surface with roughness not noticeable to touch. This operation is variant to the normal prototyping procedure, where the models printed in 3D FDM are used without further processing. This artisanal process is recommended because it is inexpensive and does not take a long time or makes the mold more expensive, which transforms into a benefit for an SME with a low budget. The technical note of Hernández [13] refers to the level of roughness or smoothness effects on the flow of the parison during blowing because of friction against the surface of the mold. This fact may seem counterproductive, however, after observing the first containers, the surface texture can be a distinctive element for SMEs that can incorporate different designs in their packaging.

A useful result for SME users of the mold is the time elapsed from scanning until delivery of the finished and clean mold, which was 6 days. Delivery time is a positive factor when compared to mold delivery times at the regional level and outside the Central American region.

4. Conclusions

The work done shows that it is possible to apply reverse engineering to manufacture a 3D printed mold with FDM technique [14]. Reverse engineering resources are usually 3D scanning equipment, computers and scanning software, 3D printing equipment, measurement and verification equipment, among others.

The digitization process is replicable by institutions that have a high definition 3D scanner, where their product will be the digital file of the mold. The resulting file will be used to manufacture the mold in any institution that has a 3D printer, when resources

are scarce, however, when the necessary resources are available, the file can be used to generate codes that are entered into computerized numerical control manufacturing equipment.

This work gives perspective to carry out research on superficial treatments of polymer molds for the increase of durability, study of the use of molds of low cadence in thermoforming processes, molding of biodegradable plastics with the use of printed molds, molds for reinforced composite materials. These results are precedents for those who have software and 3D printers can be incorporated in the productive field, providing design services and manufacturing of printed molds.

5. Acknowledgments

References

[1] Ministerio de Economía de El Salvador, "Política nacional de fomento diversificación y transformación productiva," 2015. [Online]. Available: https://bit.ly/3fLvtCe

[2] R. Martell, *Esperiencias en la empresa Roma Chemical*, 2019.

[3] G. Unruh, "Circular economy, 3d printing, and the biosphere rules," *California Management Review*, vol. 60, no. 3, pp. 95–111, 2018. [Online]. Available: https://doi.org/10.1177/0008125618759684

[4] T. Z. Sudbury, R. Springfield, V. Kunc, and C. Duty, "An assessment of additive manufactured molds for hand-laid fiber reinforced composites," *The International Journal of Advanced Manufacturing Technology*, vol. 90, no. 5, pp. 1659–1664, May 2017. [Online]. Available: https://doi.org/10.1007/s00170-016-9464-9

[5] A. Baranov, A. I. Pronin, V. A. Dikov, A. V. Zakharov, and M. G. Lagutkin, "Casting molds for the routine production of plastic hydrocyclone components," *Chemical and Petroleum Engineering*, vol. 45, no. 7, p. 513, Oct. 2009. [Online]. Available: https://doi.org/10.1007/s10556-009-9219-7

[6] C.-C. Kuo, W.-H. Chen, X.-Z. Liu, Y.-L. Liao, W.-J. Chen, B.-Y. Huang, and R.-L. Tsai, "Development of a low-cost wax injection mold with high

cooling efficiency," *The International Journal of Advanced Manufacturing Technology*, vol. 93, no. 5, pp. 2081–2088, Nov. 2017. [Online]. Available: https://doi.org/10.1007/s00170-017-0596-3

[7] Sander Kunststofftechnik. (2017) Development and production of prototypes and small series made of plastic. [Online]. Available: https://bit.ly/3dAip0C

[8] AICON 3D SYSTEMS GMBH, *OPTOCAT 2015R2 – New version, new functions*, 2015. [Online]. Available: https://bit.ly/3cvv8l7

[9] Stratasys, *Manual del usuario uPrint SE and uPrint SE plus personal 3D printers*, 2011. [Online]. Available: https://bit.ly/2T1H2eQ

[10] S. Belcher, *Practical Extrusion Blow Molding*, 1999. [Online]. Available: https://bit.ly/2WuzVha

[11] I. Suchy, *Handbook of die design*. McGraw-Hill, 2005. [Online]. Available: https://bit.ly/35YaWGb

[12] L. Espinoza and C. Nuila, *I18RE-MD001 Mediciones dimensionales a botellas de muestra*. Laboratorio de Metrología Industrial, Soyapango, 2018.

[13] J. Hernández, *Nota técnica: Principio de funcionamiento del sistema de inyección y análisis para la comprensión de la influencia del defecto rebaba de preformas PET*. Universidad de Carabobo, Valencia, Venezuela, 2013.

[14] 3D Printers. (2018) Impresoras 3d para plástico. [Online]. Available: https://bit.ly/2Z2nISf

Proposal for implantation of coffee drying greenhouse with parabolic cover and adapted modular structure

Propuesta de implantación de invernadero de secado de café con cubierta parabólica y estructura modular adaptada

Bryan Briceño-Martínez[1,*], Jairo Castillo-Calderón[1], Rubén Carrión-Jaura[1], Diego Díaz-Sinche[1]

Abstract

The present work proposes a greenhouse for coffee drying, constituted by a parabolic solar cover and adapted modular structure. It started with a planimetric survey made using different engineering and architecture software, such as: SolidWorks y Revit Architecture. For the experiment, reverse engineering principles based on an existing structure, were used to develop a modular coupling model, in order to establish interactions between mechanisms and structure. The study demonstrated that the design of the assembly couplings facilitates their mobilization, reduces costs and allows the application of accessible materials for the solar parabolic dryer (marquee). Also, the coffee drying curves in a parabolic type solar dryer and their time are shown in Statgraphics. The result of the model with modular armature couplings was correctly associated with the existing experimental results, allowing to compare the time and efficiency of the coffee drying.

Keywords: reverse engineering, design, marquee, manufacturing, parabolic, Statgraphics.

Resumen

El presente trabajo propone un invernadero destinado al secado de café formado por una cubierta solar parabólica y estructura modular adaptada. Se inició a través de un levantamiento planimétrico elaborado por diferentes *softwares* de ingeniería y arquitectura como: SolidWorks y Revit Architecture. Para el experimento se utilizó principios de ingeniería inversa, tomando como base, una estructura ya existente para desarrollar un modelo de acople modular, con el fin de establecer interacciones entre mecanismos y estructura. El estudio demostró que el diseño de los acoples de armado, facilitan su movilización, reducen costos y permiten la aplicación de materiales accesibles para el secador parabólico solar (marquesina), adicionalmente se presentan curvas de secado de café en un secador solar tipo parabólico y su tiempo representados en Statgraphics. El resultado del modelo con acoples de armado modular se asoció correctamente con resultados experimentales existentes, permitiendo realizar comparaciones entre tiempo y eficiencia del secado de café.

Palabras clave: ingeniería inversa, diseño, marquesina, manufactura, parabólica, Statgraphics.

Briceño-Martínez et al. / Proposal for implantation of coffee drying greenhouse with parabolic cover and adapted modular structure

37

1. Introduction

The worldwide coffee sector constitutes an important livelihood for millions of people, especially in developing countries. In its global production, South America represents the 47 %, followed by Asia and Oceania with 29 %, Central America and Mexico with 13 %, and Africa with 11 %. The production of Brazil, the worldwide leading coffee producer, increased 5.6 % and was 57.4 million of bags, among which was part of the harvest from April 2018 to March 2019. It is calculated that the consumption of coffee in South America increased 1.8 % and was 26.97 million of bags, after an increment of 3.5 % in 2016/2017 [1].

The use of solar energy in the agricultural sector is growing due to the price increase of the fuels, the environmental pollution and the forecasted depletion of conventional fossil fuels. The drying using solar energy is one of the most attractive and promising applications in rural areas. Usually, agricultural crops are dried by exposing them to the sun, which contributes to extend the useful life of the harvested products, thus improving the quality, position and business of the farmer, with the purpose of maintaining a constant price in their products.

The direct sun drying requires an open space of large area, and mostly depends on the availability of sunlight, which is susceptible to the pollution with foreign materials such as dust, garbage and other chemicals that may be dragged out by the wind, as well as birds, insects and rodents. Similarly, most of the agricultural products intended to be stored should be first dried, because they could be affected by insect pests and fungi that easily develop when there are humid conditions, thus becoming unusable [2].

In a peak day it can be obtained an equivalent of 2.0 % of the total yearly production of washed coffee (drained), in a farm with a production of 2500 kg c.p., for which it is required 3.3^2 of floor, having a layer with a maximum height of 3 cm [3].

With the purpose of enabling a better utilization of the solar energy, reducing the cost and facilitating the construction, operation and maintenance, a parabolic solar dryer was improved, which will be called marquee. Just like the solar tunnel dryer, it is constituted by a metal structure, a transparent plastic cover, cemented floor, rolling gates of transparent plastic and a door for internal access. The solar dryer facilitates an acceptable quality of the coveted product with a low environmental impact, and thus it is an effective, inexpensive and safe method for drying agricultural and food products.

Figure 1 shows the marquee which occupies a total area of 18 m^2, with a concrete floor that helps to make it a clean area, and houses two shelving columns with six drying beds, each of 6 m^2, which are exposed to the sun. The plastic covers are rolled and elevated when there is rain present, or when the estimated temperature is not the correct one; therefore, the height of the drying beds above the floor level is 0.60 m, thus reducing the possibility that the coffee gets contaminated as a result of the trampling of the workers, or by the accidental entry of animals [4].

Figure 1. Marquee.

1.1. Solar drying

In general, the solar dryers are classified in three categories, as shown in Figure 2.
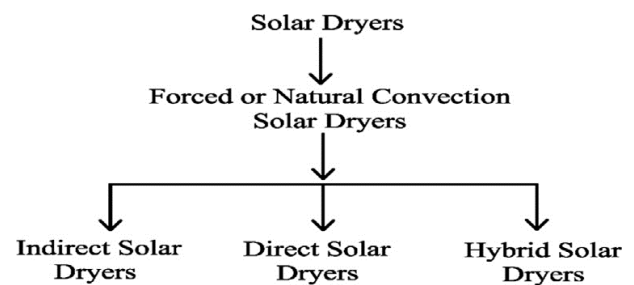
Figure 2. Classification of solar dryers [4].

In this context, this work will focus on the direct solar dryer, because the moisture of the product to be dried is eliminated by its direct exposure to sunlight, with or without natural air circulation [4]. A schematic view of the direct solar dryer is indicated in Figure 3.

The direct solar dryer has a drying chamber, an insulated box wrapped with a glass or plastic transparent cover, which has holes for letting the air move in and out of the chamber [5]. When the solar radiation affects the glass or plastic cover, the air warms and circulates naturally, or by wind pressure using an external source or a combination of both.
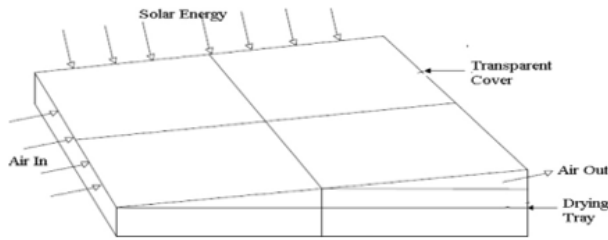
Figure 3. Direct solar dryer [5].

The construction of the direct solar dryer is simple and cheaper, and protects the product being dried from dust, rain, debris, dews, etc.; however, it also presents some drawbacks in its operation, such as product overheating, undesirable quality and limited drying capacity [6].

Tomar and Norton [7] developed a crop dryer consisting of a solar air heater and a tunnel dryer, for drying a variety of agricultural products, as can be seen in Figure 4. In comparison with the traditional solar drying methods, the drying time and the massive losses were significantly reduced with the amortization period of 1-3 years. For example, it was reported that the energy necessary for drying 1000 kg of grapes varies from 11.2 to 23.0 kWh depending on the weather conditions, with a cost between 1.2 and 2.0 USD which was absolutely insignificant as compared to the additional profit. However, the dissemination of the solar drying system to a particular area depends on the availability of electricity and of its needs.
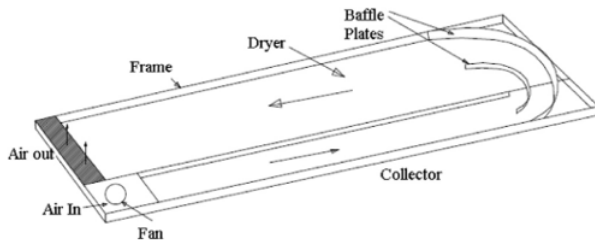
Figure 4. Solar tunnel dryer [7].

Neama and Farkas [8] presented an experimental study to increase the crop drying efficiency using a photovoltaic cell. The dryer reached a temperature of 76 °C and reduced the moisture content between 50 % and 60 %. The schematic view of the solar dryer with photovoltaic cell is shown in Figure 5.

Ogheneruona and Yusuf [9] designed and manufactured a direct natural convection solar dryer for drying tapioca, and reported a reduction of the moisture content from 79 % to 10 % wet basis at environmental conditions (32 °C and 74 % of relative humidity).
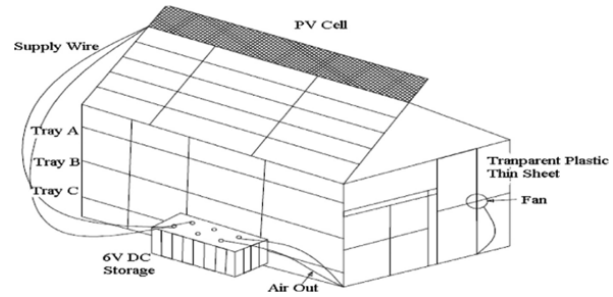
Figure 5. Photovoltaic solar dryer [9].

Tefera *et al.* [10] evaluated the performance of wooden box and pyramidal shape direct solar potato dryers, which reduced the general drying time between 2 and 3 hours compared to the open sun drying. The pyramidal dryer performed better in the generation of a more favorable drying environment, with a better economic viability. Similarly, Eke and Arinze [11] developed a prototype of a direct natural convection solar dryer made with clay, for drying corn. It was observed that the moisture content was reduced from 29 to 12 % wet basis, achieving a 55 % savings in drying time against open sun drying. It was found that the drying efficiency of the dryer and of the open sun drying method were 45.6 % and 22.7 %, respectively.

Therefore, the direct solar dryers are the devices mostly used for drying agricultural and food products. It is observed that the mean drying efficiency of direct solar dryers varies from 20 to 40 % depending on the types of products, the flow of air, and the drying location. The quality of the product obtained using direct solar dryers is acceptable, and can be improved by means of the use of certain types of pretreatment chemical processes.

2. Materials and methods

For the case study it was taken as reference the León Farm, located in the Loja canton, Vilcabamba parish. This farm has a parabolic solar dryer (marquee) consisting of a structure, shelving, and six drying beds of 6 m^2, which will be planimetrically surveyed for the design of the modular couplings for its easy mobilization and construction. The measurement equipment utilized for the survey were flexometer, laser distance meter and goniometer.

The steps followed in this research were acquisition of real measurements, the 3D planimetric survey, the conversion of the survey to a real environment using the Rendering software, the analysis of modular couplings and the graphical comparison of the efficiency of the time and the drying of the coffee.

Briceño-Martínez et al. / Proposal for implantation of coffee drying greenhouse with parabolic cover and adapted modular structure

39

2.1. Extent of the research

This research spanned a period of four months (interval between June 2019 and September 2019). The collection of data and valuable information was consulted in the following documents: i) NTE INEN 2507 [12], ii) Ecuadorian Standard of Construction NEC-11, chapter 14 Renewable Energy [13].

2.2. Planimetric survey

Dimensions of all the components that constitute the marquee are presented, as indicated in Figure 6.

Figure 6. Marquee prior to taking the measurements.

The dimensions of the marquee are 3 m high, 3 m wide and 6 m long; it consists of six beds for coffee drying, with dimensions 1 m wide x 6 m long. Figures 7 and 8 show the coffee drying beds located on the left and right hand sides, respectively, of the marquee.

Figure 7. Coffee drying beds located on the left hand side inside the marquee.

Figure 8. Coffee drying beds located on the right hand side of the marquee.

2.3. Acquisition of real measurements

The acquisition of real measurements concerning the marquee, where it is evident the front view (Figure 9), right side view (Figure 10), left side view (Figure 11) and internal part (Figure 12).

Figure 9. Dimensioned front view.
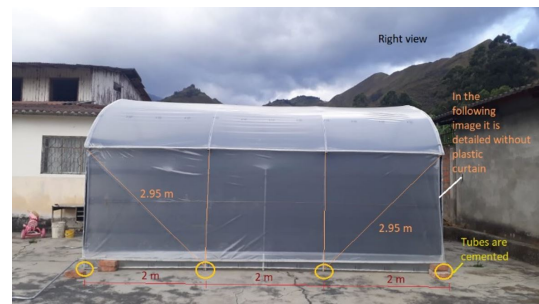
Figure 10. Dimensioned right side view.
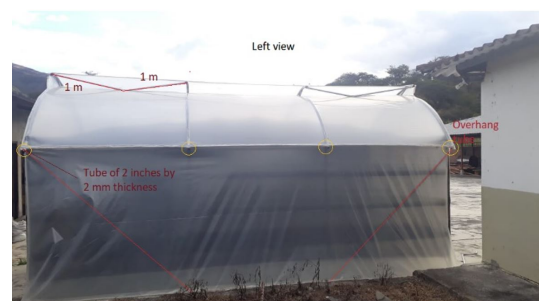
Figure 11. Dimensioned left side view.
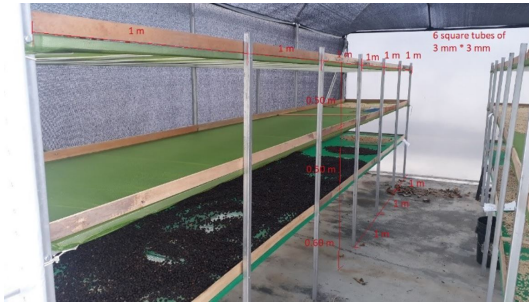
Figure 12. Internal view of the marquee.

2.4. 3D survey

For taking measurements of the different components of the marquee, it is proceeded to make the survey in three dimensions; for this it is required an interactive software and different applications, both for learning technical drawing and for engineering analysis; Solid-Works is chosen [14]. In the following, it is detailed the front (Figure 13), right side (Figure 14), upper (Figure 15) and isometric (Figure 16) views.
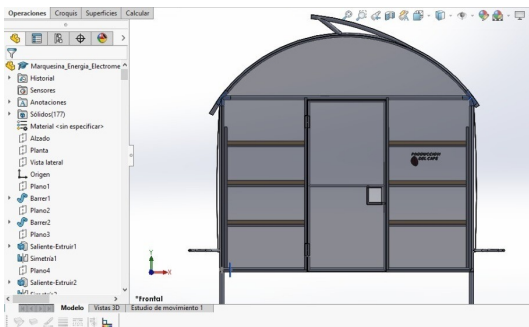
Figure 13. Front view of the marquee.
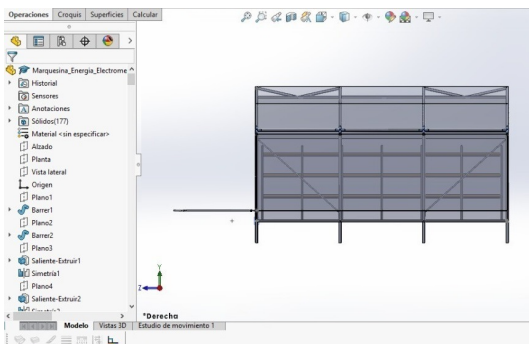
Figure 14. Right side view of the marquee.
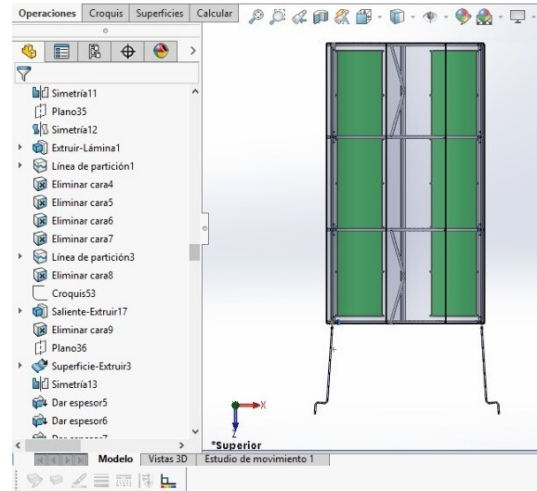
Figure 15. Upper view of the marquee.
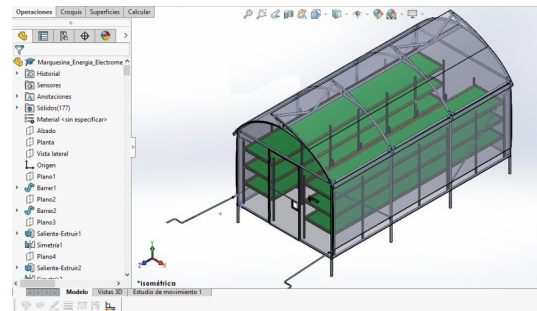
Figure 16. Isometric view made with the SolidWorks software.

2.5. Architectural presentation

For a better finish and future projection of a scale prototype, the model made by SolidWorks is converted to a real environment using the Rendering software [15] applied in the architectural field. Figures 17 and 18 present the isometric design made by Rendering.

Figure 17. Marquee designed by Rendering.

Briceño-Martínez et al. / Proposal for implantation of coffee drying greenhouse with parabolic cover and adapted modular structure

41
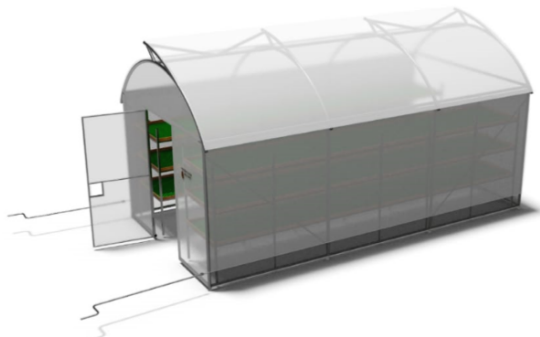
Figure 18. Isometric view of the marquee.

2.6. Materials and costs

In parallel with taking the measurements, a revision of the materials that constitute the marquee was carried out. Table 1 presents the main elements.

Table 1. Materials implemented in the marquee

Materials	Quantity used
Greenhouse plastic	25 m
Saran Mesh	24 m
Green plastic mesh 3/16"	12 m
Bug repellent plastic mesh	24 m
Galvanized round tube 2"	54,76 m
Galvanized round tube 1"	21,19 m
Square tube	28 m
Angles	83,4 m
Corrugated rod 8	43,5 m
Steel wire	60 m
Thread	254 m
Wood strips	83,4 m
Hexagonal bolts and nuts	36 units

The estimated costs of the materials that are available in the domestic market are indicated in Table 2.

2.7. Experimental design

The results of the analyses and the graphs regarding drying time and efficiency, were obtained from the statistical software STATGRAPHICS Centurion XV (Trial version 16.1.18) [16]. A factorial design of one or various factors was used as the experimental design. The theory of the efficiency of the collector of Duffie and Beckmen [17] was established in the thermal study. The following equation (1) is utilized for calculating the thermal efficiency of a greenhouse.

$$n_{empty} = \frac{C_p \dot{m}_a (T_0 - T_i)}{A_s I_s} \qquad (1)$$

Where n_{empty} is the percentage of thermal efficiency of the empty greenhouse, C_p is the air specific

heat (kJ/kg °C); m_a, mass flow of air; T_0, initial temperature of the greenhouse; T_i, final temperature of the greenhouse; A_s area of the greenhouse and I_s is the solar intensity on the wall and roof of the greenhouse.

Table 2. Costs of materials employed

Materials	Commercial presentation	Estimated value $
Greenhouse plastic	roll of 200 m	106,25
Saran Mesh	rollo de 30 m	182,4
Green plastic mesh 3/16"	roll of 30 m	57,48
Anti Trip Bug repellent plastic mesh	roll of 100 m	79,92
Galvanized round tube	6 m	238,2
Galvanized round tube	6 m	35,8
Square tube	6 m	35,8
Angles	6 m	161
Corrugated rod 8	6 m	38,4
Steel wire	roll of 75 m	33
Thread	roll of 100 m	63,5
Wood strips	2 m	48
Hexagonal bolts and nuts	perno de 2"	3,96
TOTAL		**$1.083,71**

3. Results and discussion

3.1. Analysis of the structural coupling

The software engineering techniques are utilized for modeling systems, specially the design and simulation of tunnel greenhouses. Traditional concepts of object oriented technology, are focused on developing software based on software engineering components, similar to the model-based design, the specification of the components and standards, applying the use of libraries and the reutilization of design structures [18, 19]. All these techniques are common in the design of greenhouses, as indicated in Figure 19.

Figures 20 and 21 present the structure of the marquee made by SolidWorks, detailing the design of the coupling of assembly in the corners and in the rear part, indicating the type of tube and its specifications, with the purpose of providing an easy access of assembling and disassembling for its quick mobilization.

When there is the need to model multitunnel greenhouses, methods that include concepts of reutilization, class hierarchy and succession are applied, which enable the user to have available different technological applications, with the purpose of constructing a series

of basic blocks for manufacturing greenhouses, once the design has been revised. From this point of view, a greenhouse is no more than a series of blocks adapted to a space; the efficiency in the use of such space constitutes a critical issue [20].
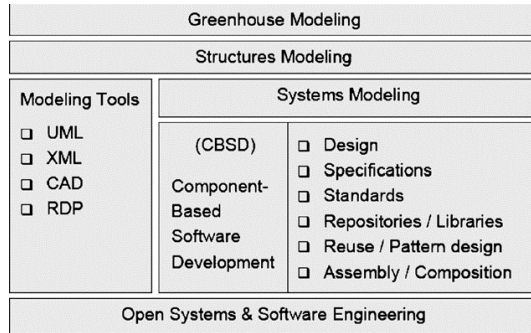
Figure 19. ASome software engineering techniques for greenhouse modeling [18].
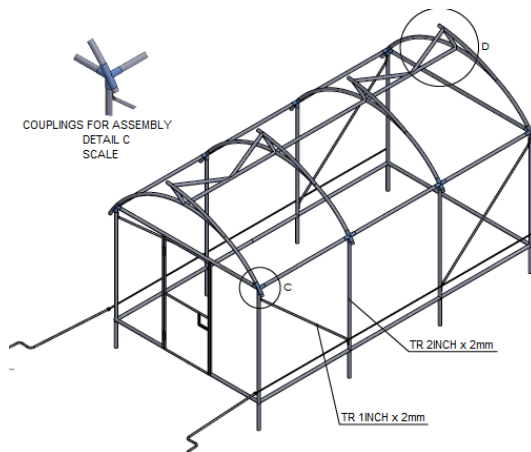
Figure 20. Coupling of assembly of the marquee.
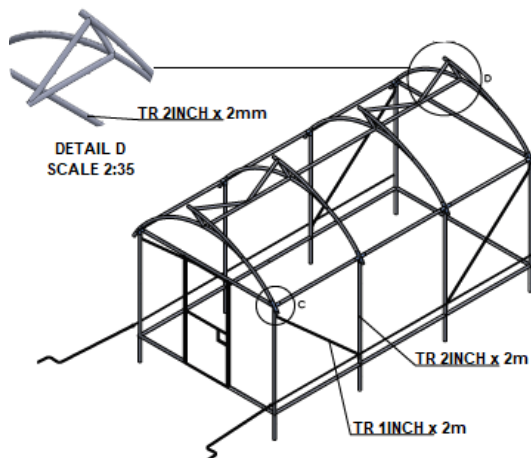
Figure 21. Detail of the structure.

3.2. Analysis of the shelving

At present, the unified modeling language (UML) is utilized in different engineering disciplines for modeling systems, which enables to understand and describe the structure and operation of a system under study; for example, the UML is utilized in industrial systems: automotive sector [21, 22], teleoperation [20], robotics [22, 23], and production systems for monitoring [24]. Therefore, UML has been employed in the agricultural sector as a complementary technique for modeling greenhouses.

The technique of Computer Aided Design (CAD) is used for the analysis of the shelving, as indicated in Figure 22, which shows the length and height, Figure 23, which shows the separation of the coffee drying beds and the type of tube employed with its specifications. At last, Figure 24 details an isometric view of the shelving constituted by six drying beds, and specifies the composite material and its dimensions.
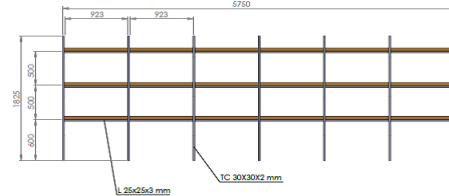
Figure 22. Dimensions of the coffee drying beds.
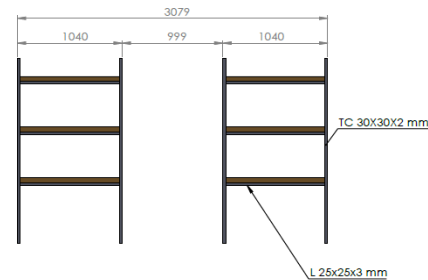
Figure 23. Distance between columns of drying beds.
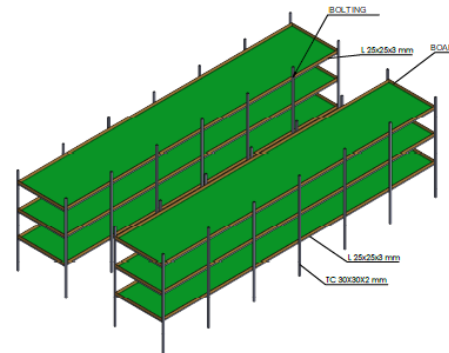
Figure 24. Isometric view of the shelving and its specifications.

Briceño-Martínez et al. / Proposal for implantation of coffee drying greenhouse with parabolic cover and adapted modular structure

43

3.3. Analysis, moisture – coffee drying time

In order to estimate the relationship between moisture and coffee drying time, it is proceeded to perform a statistical analysis of linear regression, due to the little curvature exhibited by the plots in Figure 25, setting the moisture (%) as the dependent variable and the drying time (days) as the independent variable. Figure 25 indicates the plot of the model fitted, moisture – drying time, setting equations (2) and (3) as such model.

$$Y = a + b \times X \qquad (2)$$

$$Moisture = 50,7786 + 5,79048 \times drying\ time \quad (3)$$
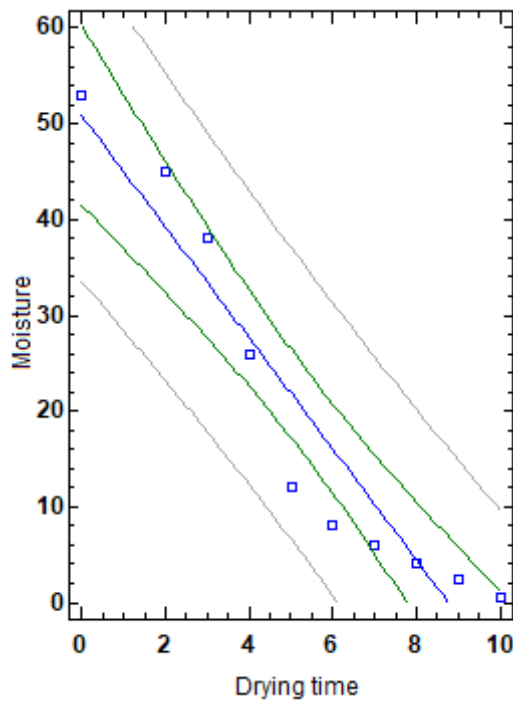
Figure 25. Plot of the fitted model moisture – drying time.

Table 3 presents the coefficients of the relationship moisture – drying time, where it is shown the estimated and incorrect parameters of the coffee drying.

Table 3. Coefficients, moisture – drying time

Parameter	Least Squares Estimated	Standard Error	Stadistical T	P-value
Intercept	50,7786	4,05208	12,5315	0
Slope	–5,79048	0,653902	–8,85527	0

From the statistical analysis, the following values were obtained:

- Correlation coefficient = –0.952588

- R-squared = 90,7424 %

- R-squared, (titted for g. l.) = 89.5852 %

- Standar error ofthe estimate = 6.28562

- Mean absolute error = 4.83571

- Durbin-Watson Statistical = 0.587605 (P = 0.0005)

- Autocorrelation of residues in delay 1 = 0.60396

It can be seen in Table 4 that the P-value is smaller than 0.05, which indicates that there is a significant statistical relationship between moisture and drying time, with a confidence level of 95.0 %.

Table 4. Analysis of variance moisture-drying time of the coffee

Source	Sum of squares	Gl	Mean square	F-ratio	P-value
Model	3098,14	1	3098,14	78,42	0,0000
Residue	316,073	8	39,5091		
Total	3414,21	9			

The statistical parameter R-squared indicates the fitted model, showing a 90.7424 % of variability in the moisture, and consequently the correlation coefficient is equal to -0.952588, which indicates a relatively strong relationship between the variables. The estimated standard error shows that the standard deviation of the residues is 6.28562 and the mean absolute error is 4.83571, since it is the average value of the residues.

The Durbin-Watson (DW) statistical analysis indicates the residues with the purpose of determining if there is any significant correlation based in the order in which the collected data are presented.

Since the P-value is smaller than 0.05, there is an indication of a possible serial correlation with a confidence level of 95.0 %, which means that the smaller the drying time in the greenhouse, the greater the percentage of moisture.

3.4. Analysis, Drying area – production

In places in which the solar drying has yearly productions smaller than 500 arrobas of dried parchment coffee, they usually occupy drying places such as marquees, canopies or parabolic dryers [25]. Table 5 presents a statistical summary showing the average and standard deviation of the samples. It should be taken into account that there is a difference of more than 3 to 1 between the smallest and largest standard deviations. This may cause problems because the analysis of variance assumes that the standard deviation of all the levels is equal, thus, the production of coffee in quintals is increasing.

Table 5. Statistical summary of the drying area and production

	Count	Average	Standard deviation	Coef. of variation	Min.
Drying area	8	63	51,8129	82,2426%	12,0
Production	8	210	172,71	82,2426%	40,0
Production in quintals	8	48,75	44,7014	91,6952%	10,0
Total	24	107,25	126,677	118,1140%	10,0

Table 6 presents an ANOVA table, which decomposes the variance of the data in two components: one between groups and another inside groups. The F-ratio, which in this case is equal to 5.54178, is the quotient between the estimate between groups and the estimate inside groups, since the P-value of the F-test is smaller than 0.05; there is a statistically significant difference between the means of the three variables with a confidence level of 95 %, and thus, they are valid and accurate statistical samples in the production of coffee.

Table 6. Anova table

Source	Sum of squares	Gl	Mean square	F-Ratio	P-value
Between groups	127503	2	63751,5	5,54	0,0117
Inside groups	241580	21	11503,8		
Total (Corr.)	369083	23			

Table 7 shows the mean for each column of the obtained data, and the standard error of each mean, which is a measure of the variability of the sampling. The standard error indicates a result of dividing the pooled standard deviation by the number of observations in each level. In addition, it also marks a sample of interval around each mean.

Table 7. Table of means with confidence intervals of 95 %

	Cases	Mean	Est. Error (s) Gropued	Lower limit	Upper limit
Drying area	8	63	37,9206	7,23727	118,763
Production	8	210	37,9206	154,237	265,763
Production in quintals	8	48,75	37,9206	−7,01273	104,513
Total	24	107,25			

The intervals currently shown are based in the procedure of the least significant difference (LSD) of Fisher; it is constructed in such a way that, if two means are equal, their intervals will overlap 95 % of the times, which can be graphically observed in Figure 26.

Figure 27 indicates the relationship of the drying area with the production in arrobas of dried parchment coffee; it presents that in a drying area of 18 m² of the marquee it can be produced around 1500 kg yearly.
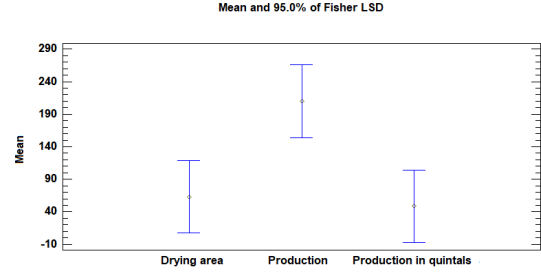
Figure 26. Graph of means and of the 95 % of Fisher LSD.
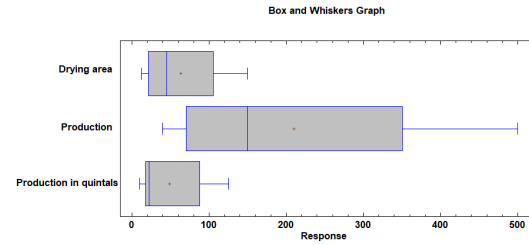
Figure 27. Box-and-whisker plot of the area-production relationship.

3.5. Directional field of the heat flow inside the marquee

When Newton's law is considered to study the effect with which a body reaches the internal temperature, as it is the case of the coffee bean inside the marquee, the temperature T of the coffee bean and the ambient temperature T_a are considered. Equation (4) is employed for studying the field of directions of the heat flow inside the marquee.

$$\frac{\partial T}{\partial t} = K(T - T_a) \qquad (4)$$

Constant K is the thermal conductivity of the medium, considering a controlled environment of $0,02 \left[\frac{W}{Km}\right]$. The initial condition of the problem will be $T(t_0) = T_0$. The particular solution of the equation for time $t_0 = 0$. (Equation 5).

$$T(t) = (T_a - T_0) \cdot e^{Kt} + T_a \qquad (5)$$

From the measured temperature data inside the marquee it was established a $T_a = 82$L, considering that there are not adiabatic losses for the analysis. The representation of the field of directions for the autonomous continuous ordinary differential equation (Equation 6, Equation 7) is shown in Figure 28, employing a set of meshed points. It can be appreciated an equilibrium point at the ambient temperature inside the marquee. It also occurs that the points below this point behave as attractor points that have an exponential growth.

$$Tv = \begin{bmatrix} t \\ T \end{bmatrix} \quad (6)$$

$$T_{dor} = \begin{bmatrix} t \\ T \end{bmatrix}' = \begin{bmatrix} 1 \\ K(T - T_a) \end{bmatrix} = \begin{bmatrix} 1 \\ K(Tv(2)) \end{bmatrix} \quad (7)$$
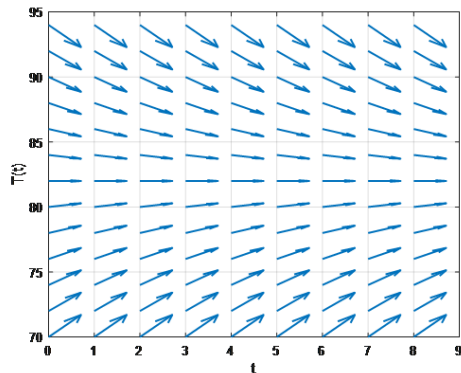
Figure 28. Plot of the directional field for the direction of heat inside the marquee.

4. Conclusions

The use of the marquee is applied to the drying of agricultural products, highlighting the drying of coffee, due to its great potential from the experimental and energy saving viewpoints. There are different types of solar dryers that have been designed and developed in some agro-industry sectors, producing different degrees of technical performance. The modular couplings made after the planimetric survey, have enabled to improve its mobility and adaptability.

The values obtained regarding the relationship moisture and drying time of the coffee, exhibited a linear regression statistical analysis, setting the moisture as the dependent variable and the drying time as the independent variable resulting in a fitted model, showing a reduction of moisture with an increase of drying. In the analysis of variance of the moisture with respect to the drying of coffee it was obtained a P-value smaller than 0.05, which indicates that there is a significant statistical relationship between moisture and drying time with a confidence level of 95 %.

In the analysis of production with respect to the drying area it was made a statistical summary based on an average of samples and standard deviation, and it was obtained a difference of more than 3 to 1 between the smallest and the largest standard deviations, thus it is assumed that the standard deviations of all levels are equal, providing a growth in the production of coffee. It was performed a variance of the data in two components: between groups and inside groups,

giving a statistically significant difference between the means of the three variables with a confidence level of 95 %, indicating that the data obtained are valid and convenient statistical samples in the production of coffee.

The intervals of moisture and drying area indicate the relationship of drying area with the production in arrobas of dried parchment coffee, for a drying area of 18 m^2 there is the capacity of producing fifteen quintals yearly.

References

[1] ICO, *Anuario 2017–2018*. International Coffee Organization, 2018. [Online]. Available: https://bit.ly/36fPT1G

[2] K. Jitjack, S. Thepa, K. Sudaprasert, and P. Namprakai, "Improvement of a rubber drying greenhouse with a parabolic cover and enhanced panels," *Energy and Buildings*, vol. 124, pp. 178–193, 2016. [Online]. Available: https://doi.org/10.1016/j.enbuild.2016.04.030

[3] C. E. Oliveros-Tascón, C. A. Ramírez-Gómez, and J. R. Sanz-Uribe, "Secador solar de túnel para café pergamino," *Avances Técnicos Cenicafé*, pp. 1–8, 2006. [Online]. Available: https://bit.ly/3cNt2NG

[4] M. Kumar, S. K. Sansaniwal, and P. Khatak, "Progress in solar dryers for drying various commodities," *Renewable and Sustainable Energy Reviews*, vol. 55, pp. 346–360, 2016. [Online]. Available: https://doi.org/10.1016/j.rser.2015.10.158

[5] A. Ghazanfari, L. Tabil Jr., and S. Sokhansanj, "Evaluating a solar dryer for in-shell drying of split pistachio nuts," *Drying Technology*, vol. 21, no. 7, pp. 1357–1368, 2003. [Online]. Available: https://doi.org/10.1081/DRT-120023183

[6] M. E.-A. Slimani, "Etude d'un séchoir solaire agricole muni d'un capteur solaire de type "pv-therm" : réalisation d'un prototype et caractérisation," Ph.D. dissertation, 2017. [Online]. Available: https://bit.ly/2LQNzVr

[7] V. Tomar, G. N. Tiwari, and B. Norton, "Solar dryers for tropical food preservation: Thermophysics of crops, systems and components," *Solar Energy*, vol. 154, pp. 2–13, 2017, solar Thermal Heating and Cooling. [Online]. Available: https://doi.org/10.1016/j.solener.2017.05.066

[8] M. Al-Neama and I. Farkas, "Utilization of solar air collectors for product's drying processes," *The Journal of Scientific and Engineering Research*, vol. 5, no. 2, pp. 40–56, 2018. [Online]. Available: https://bit.ly/3eaPDUJ

[9] D. E. Ogheneruona and M. O. L. Yusuf, "Design and fabrication of a direct natural convection solar dryer for tapioca design and fabrication of a direct natural convection solar dryer for tapioca," *Leonardo Electronic Journal of Practices and Technologies*, vol. 10, no. 18, pp. 95–104, 2011. [Online]. Available: https://bit.ly/3bMGqQz

[10] A. Tefera, W. Endalew, and B. Fikiru, "Evaluation and demonstration of direct solar potato dryer," *Livestock Research for Rural Development*, vol. 25, no. 12, 2013. [Online]. Available: https://bit.ly/2LN8Lf4

[11] R. Patil and R. Gawande, "A review on solar tunnel greenhouse drying system," *Renewable and Sustainable Energy Reviews*, vol. 56, pp. 196–214, 2016. [Online]. Available: https://doi.org/10.1016/j.rser.2015.11.057

[12] INEN, *NTE INEN 1757 Frutas frescas, limón, requisitos.* Norma Técnica Ecuatoriana, 2016. [Online]. Available: https://bit.ly/2XtNXPt

[13] MIDUVI, *NEC-11. Energías Renovables.* Norma Ecuatoriana de la Construccón, 2011. [Online]. Available: https://bit.ly/2XdaEqY

[14] Dassault Systemes. (2019) SOLIDWORKS. [Online]. Available: https://bit.ly/2XdakZf

[15] Rendering. (2019) Rendering, rendering 3d, rendering animation. [Online]. Available: https://bit.ly/3e2eUQK

[16] R. García, *Curso básico de STATGRAPHICS Version 5.0*, 2005. [Online]. Available: https://bit.ly/2ZjCB2Z

[17] J. A. D. W. A. Beckman, *Solar Thermal Power Systems.* John Wiley & Sons, Ltd, 2013, ch. 17, pp. 621–634. [Online]. Available: https://doi.org/10.1002/9781118671603

[18] G. T. Heineman and W. T. Councill, *Component-based Software Engineering: Putting the Pieces Together.* ACM Press series, 2001. [Online]. Available: https://bit.ly/2zjQfs2

[19] L. Iribarne, J. M. Troya, and A. Vallecillo, "A trading service for cots components," *The Computer Journal*, vol. 47, no. 3, pp. 342–357, 2004. [Online]. Available: https://doi.org/10.1093/comjnl/47.3.342

[20] L. Iribarne, J. A. Torres, and A. P. na, "Using computer modeling techniques to design tunnel greenhouse structures," *Computers in Industry*, vol. 58, no. 5, pp. 403–415, 2007. [Online]. Available: https://doi.org/10.1016/j.compind.2006.09.001

[21] S. H. Kong, S. D. Noh, Y.-G. Han, G. Kim, and K. I. Lee, "Internet-based collaboration system: Press-die design process for automobile manufacturer," *The International Journal of Advanced Manufacturing Technology*, vol. 20, no. 9, pp. 701–708, Oct. 2002. [Online]. Available: https://doi.org/10.1007/s001700200209

[22] K. L. Mills and H. Gomaa, "A knowledge-based method for inferring semantic concepts from visual models of system behavior," *ACM Trans. Softw. Eng. Methodol.*, vol. 9, no. 3, pp. 306–337, Jul. 2000. [Online]. Available: https://doi.org/10.1145/352591.352594

[23] M. Wirsing, A. Knapp, and S. Balsamo, *Radical Innovations of Software and Systems Engineering in the Future.* 9th International Workshop, RISSEF 2002, Venice, Italy, October 7-11, 2002, Revised Papers. Springer-Verlag Berlin Heidelberg, 2004. [Online]. Available: https://doi.org/10.1007/b96009

[24] M. Ghazel, A. Toguyéni, and M. Bigand, "An uml approach for the metamodelling of automated production systems for monitoring purpose," *Computers in Industry*, vol. 55, no. 3, pp. 283–299, 2004, object-oriented modelling in design and production. [Online]. Available: https://doi.org/10.1016/j.compind.2004.08.005

[25] Cenicafé, "Secado del café pergamino," *Cenicafé*, 2019. [Online]. Available: https://bit.ly/2zZwRk0

Control of a System of Energy based on Flywheel to mitigate the Voltage Gaps at the Point of Common Coupling

Control de un sistema de energía basado en volantes de inercia para mitigar los huecos de tensión en el punto de conexión común

Carlos Orellana Uguña[1,*], Luis González Morales[2], Nuno Abreu Sousa[3]

Abstract

This article presents the design of a power system based on flywheel to mitigate voltage sags. With this system the power quality is improved at a point in a distribution network, which is subject to the random connection of electric machines. For this purpose, the power distribution system is modeled, the power supply system which is composed of an electric machine with flywheel, the bidirectional energy conversion system and the current, voltage and speed control system. The designed system enables supplying a power of 22.8 kW and capacity of 1.2 Wh, compensating the transients produced by the loads connected to the network.

Keywords: Batteries, flywheel, AC/DC, PCC.

Resumen

Este artículo presenta el diseño de un sistema de energía basado en volante de inercia para mitigar los huecos de tensión. Con el sistema se mejora la calidad de energía en un punto de una red de distribución, el cual está expuesto a la conexión aleatoria de máquinas eléctricas. Para ello, se modela el sistema de distribución de energía, el sistema de inyección de energía que está compuesto por una máquina eléctrica con volante de inercia, el sistema de conversión de energía bidireccional y el sistema de control de corriente, voltaje y velocidad. El sistema diseñado permite inyectar una potencia de 22.8 kW y capacidad de 1.2 Wh, compensando los transitorios producidos por las cargas conectadas a la red.

Palabras clave: baterías, volante de inercia, AC/DC, DC/AC, PCC.

[1,*]Instituto Tecnológico Superior Luis Rogerio González, Azogues – Ecuador.
Corresponding author ✉: carl.mauryou@yahoo.es. ⓘ http://orcid.org/0000-0001-7214-4060
[2]Departamento de Ingeniería Eléctrica Electrónica y Telecomunicaciones (DEET), Universidad de Cuenca, Cuenca – Ecuador. ⓘ http://orcid.org/0000-0001-9992-3494
[3]Departamento de Engenharia Electrotécnica da Escola Superior de Tecnologia e Gestãodo Instituto Politécnico de Leiria - Portugal. ⓘ http://orcid.org/0000-0002-3837-0547

1. Introduction

Since the electric power distribution company is responsible for supplying power to the consumers based on established standards, it is under the obligation to maintain the quality of the delivered power, and such quality can be estimated by means of the service continuity and the quality of the voltage waveform.

In order to carry out this objective, different power backup strategies were implemented in electrical power systems, which seek to improve the power quality and stability [1]. According to their discharge time [2], these systems may be classified as follows:

> Discharge time from seconds to minutes: are used to improve the power quality. The discharge times are of 10 minutes with responses in milliseconds. This type of systems include the supercapacitors with powers up to 1 MW, and the flywheels with powers between 10 kW and 1 MW.

> Discharge time from minutes to one hour: are used as power bridges, i.e., they ensure the reliability of the supply source to the users, have responses from seconds to minutes with discharge times of up to 1 hour, and powers between 1 kW and 10 MW. Electrochemical batteries are included in this type.

> Discharge time in hours: they are utilized for energy management; this type includes the pumped and compressed air hydraulic energy storage, with powers between 100 MW and 1 GW, respectively, and the thermal energy storage with storage capacities between 10 MW and 100 MW.

Regardless of the technology used, it must be considered aspects such as: operating and constructive expenditures, life cycle, response time after the occurrence of a disturbance in the network, geographical limitations and physical properties [3].

If geographical limitations are considered, the pumped storage systems are ruled out, since they require two reservoirs located at different levels because the energy stored is proportional to the volume of liquid and to the difference between the heights of the reservoirs, thus its installation is limited to places with non-planar characteristics.

Compressed air is neither chosen because it requires very resistant underground caverns to house air at high pressure and, at last, the thermal energy storage is discarded since the operating principle of each of them depends on the working ambient temperature.

As a result, electrochemical batteries, flywheels and supercapacitors are the options remaining [2].

The electrochemical batteries exhibit drawbacks, such as: at the end of their useful life they pollute the environment because an adequate recycling infrastructure is not available [4], their useful life depends on the working environment and on the number of charges/discharges and, the most important, they cannot be charged nor discharged quickly because they have a large internal resistance [5].

Therefore, the use of the flywheels is the option remaining, which offer the following advantages: a greater cycle of charges/discharges with medium to high power (kW to MW) during short periods of time (seconds) without affecting their useful life [6], high response capacity, friendly to the environment since they do not require chemical reactions, and no special geographical conditions are needed for their construction [7].

In comparative terms, the main competitors of the flywheels are the supercapacitors, which similarly offer the following advantages over electrochemical batteries: they may be charged/discharged in short periods of time (seconds), may supply high charge currents, have a life cycle of the order of millions of times, operate under very tough temperature conditions, and do not have toxic elements in their structure [2].

In this work it is intended to carry out the study about the design of a power supply system based on flywheels, to mitigate the voltage sags in the common connection point of an electrical distribution system. For this purpose, it will be modeled the flywheel with its control system and the distribution network. The design is applied to a rural area with mining and agricultural activities with electric machines as loads, using PSIM® as simulation tool.

1.1. Problem description

Due to the increase in the loads connected to the common connection point (CCP) belonging to the mining and agricultural area under study, the power supply quality decreases, due to the features of the existing distribution system and the continuous start-up of high-capacity electric machines, and also soft starters that contribute to the occurrence of voltage sags.

The case study will cover the Pucará canton and surroundings, specifically the San Juan de Naranjillas village belonging to the Azuay province, Ecuador, which is supplied by the feeder 1424 of the South Regional Electric Company (Empresa Eléctrica Regional Sur).

Due to the lack of technical standards that regulate the power of the motors utilized in the different mining/agricultural activities, it was considered as reference the machinery utilized in a main mining company called TRES CHORRERAS, which establishes the use of 32 HP Allis Chalmers motors, and according to this and catalogs available in Ecuador, W21 50 HP Explosion-proof NEMA Premium electric motors are utilized to drive centrifugal pumps for liquid handling, crushers, conveyor belts, among others [8].

The features of the motors to be utilized are indicated in Figure 1 [9].

Orellana Uguña et al. / Control of a System of Energy based on Flywheel to mitigate the Voltage Gaps at the Point of Common Coupling

51

The simulation model of the distribution network is indicated in Figure 1, with resistances of 20Ω that emulate small electrical equipment distributed in each of the phases (lightning, appliances).
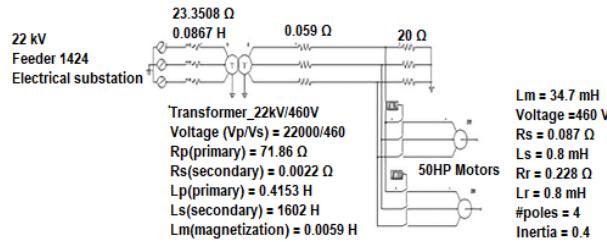
Figure 1. Model of the distribution network and features of the 50 HP motors.

1.2. Power quality

One of the important aspects related to the power quality are the so-called voltage sags, described in detail in the technical standards IEEE 1159, CONELEC 004/01 and NP EN 50160-2010, which define them as a decrease in the supply voltage to a value between 10 % and 90 % of the nominal voltage.

In addition, the standards define the voltage swell as an increase in the supply voltage to a value between 110 % and 180 % of the nominal voltage, followed by a voltage restore after a short period of time. Applying this criterion to the phase-to-neutral voltage level of the secondary side of the transformer of Figure 1, the range for the occurrence of sags is between 26.55 V and 238.95 V, and for swells between 292.05 V and 477.9 V, thus resulting in a permissible range from 238.95 V to 292.05 V.

The methods utilized in this work to mitigate the occurrence of voltage sags are described in the following.

2. Materials and Methods

2.1. Proposed power system for the mitigation of voltage sags in the common connection point

Figure 2 shows the block diagram model proposed by this study to mitigate the voltage sags in the CCP, which is constituted by an electrical machine with flywheel, two controlled three-phase power converters and a coupling capacitor called DC-link.
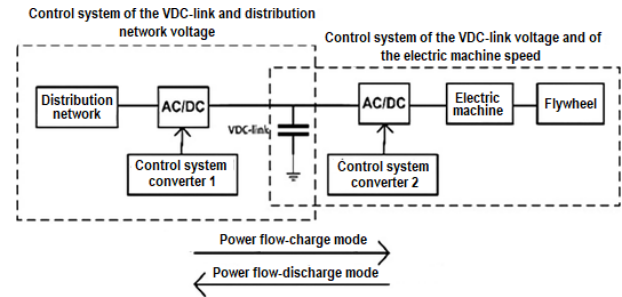
Figure 2. System based on flywheel to mitigate voltage sags in the CCP.

In Figure 2, the proposed model consists of the followings control stages:

Control system 1: The power converter associated to the distribution network consists of a control of current in the synchronous reference system such as the utilized in [10,11]. Its task is to control the distribution network voltage and the DC-link voltage. This control may be divided in two sub-stages: charge mode, power flows from the distribution network to the direct current bus to reach the nominal value of $V_{DC-link}$. In this mode, the $V_{DC-link}$ control system operates using the converter as a controlled three-phase rectifier. In discharge mode, power flows from the direct current bus to the distribution network, in this mode, the control system of the distribution network voltage operates using the converter as a controlled three-phase inverter.

Control system 2: the power converter associated to the electric machine consists of a control of current in the synchronous reference system. This control system can be divided in two sub-stages: charge mode, power flows from the $V_{DC-link}$ voltage source to the electric machine that is operating as a motor to reach the nominal speed of charge, in this mode, the electric machine speed control system operates using the converter as a controlled three-phase inverter. In this state, the energy of the system is stored as kinetic energy. In discharge mode, power flows from the electric machine operating as a generator to the $V_{DC-link}$ source, to maintain the voltage at a reference value in the presence of any load connected to the distribution network. In this mode, the control system of the voltage $V_{DC-link}$ of the intermediate circuit operates using the converter as a controlled three-phase rectifier.

The change between the control modes is subject to the voltage at the CCP; in this sense, each of the power converters will operate as AC/DC or DC/AC.

The control loops that constitute the power supply system based on flywheel are described in the following.

2.1.1. Control system 1, belonging to the control of the distribution network voltage and of the $V_{DC-link}$ voltage.

The control system 1 has a structure defined by the charge or discharge operation mode. Figure 3 shows a block diagram of the cascade control system.

Due to the voltage level which are able to withstand the SKiM459GD12E4 three-phase converter and the coupling capacitor U37F type E37F501CPN103MFK0M, a voltage level of 900 Vdc was established as reference for the $V_{DC-link}$.
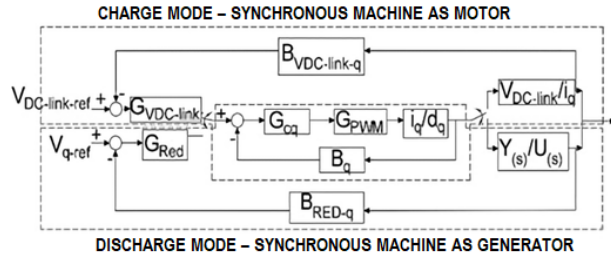
Figure 3. Control loops of the distribution network voltage and of the $V_{DC-link}$ voltage.

From Figure 3, B_q, B_{Red-q}, $B_{VDC-link}$ are the gains associated to the measurements of current, distribution network voltage and $V_{DC-link}$ voltage, respectively, with unit values, G_{cq}, $G_{VDC-link}$, $G_{network}$ are the transfer functions of the controllers, where in this application classical controllers of proportional-integral (PI) configuration are utilized, G_{PWM} is the gain of the PWM, a unit gain has been used in this case, $\frac{Y(s)}{U(s)}$ represents the transfer function that relates the distribution network voltage with respect to the current in the quadrature axis, and $\frac{V_{DC_{link}}}{\tilde{i}_q}$ is the transfer function that relates the $V_{DC-link}$ voltage with respect to the current in the quadrature axis.

The power converter can be modeled through equation 1, as utilized in [10, 11].

$$\frac{\tilde{i}'_{d(s)}}{\tilde{d}'_{d(s)}} = \frac{\tilde{i}'_{q(s)}}{\tilde{d}'_{q(s)}} = \frac{V_0}{Ls' + R_s} \qquad (1)$$

The following is considered regarding the parameters involved in Equation 1:

V_0 is the $V_{DC-link}$ voltage, which in the present work has been defined at a value of 900 V.

According to [12], L is the inductance of the input filter. For the calculation it is proceeded in the following way: the inductive reactance

is considered equal to 10 % of the base resistance [10], thus resulting $Xl = 0,565\ \Omega$, and therefore, $L = 1,5\ mH$. From this initial value L is calibrated until reaching a value of 7 mH, with which the total harmonic distortion (THD) fulfills the standard NP EN 50160-2010, Conelec 004/01 (smaller than 8 %).

According to [12], R_s is associated to the losses of the passive elements and semiconductors in the converter.

s' is the Laplace operator.

Similarly, the energy balance equations associated to the capacitor of the bus, which can represented by means of equations (2) and (3) [10], are also honored.

$$\frac{V_{DC\_link}}{\tilde{i}_q} = \frac{D_q}{Cs' + \frac{I_0}{V_{DC\_link}}} \qquad (2)$$

$$D_q = \frac{2\sqrt{2}V_{f-n}}{V_{DC\_link}} \qquad (3)$$

Where: D_q is the modulation index, C is the total capacitance of the capacitors that constitute the direct current bus, I_0 is the current that circulates from the rectifier bridge to the direct current bus, $V_{DC_{link}}$ is the voltage of the direct current bus, s' is the Laplace operator.

In the case of the discharge mode, the power converter controlled by means of the current loops in the direct and quadrature axes is utilized for controlling the voltage in the distribution network by means of the transfer function $\left(\frac{Y(s)}{U(s)}\right)$, which for the design of the control system has been characterized as a first order approximation. In order to find the parameters that constitute such transfer function, it is considered that the system based on the flywheel will be connected in parallel to the distribution network behaving as a current source. Graphically, Figure 4 shows the scheme to determine the previously described transfer function by means of the step response.

Figure 4. Model for the transfer function that relates the voltage at the CCP with the supply of current in phase.

Orellana Uguña et al. / Control of a System of Energy based on Flywheel to mitigate the Voltage Gaps at the Point of Common Coupling

53

When applying the previously described procedure, the behavior of the distribution network voltage after a disturbance in current with amplitude $\Delta I = 400\ A$ results in $\Delta V = 51,6\ V$, obtaining a transfer function as the one given by Equation 4.

$$\frac{Y_{(s)}}{U_{(s)}} = \frac{0,129}{0,287s' + 1} \tag{4}$$

It is important to remark that the currents supplied from the energy storage system to the CCP, require a phase synchronization system to control the active or reactive power. A normalized phase-locked loop (PLL) system as the one used in [10] has been utilized in this design.

2.1.2. Control system 2, belonging to the control of the electric machine speed and of the $V_{DC-link}$ voltage.

The electric machine used in the present work is a permanent magnet synchronous machine, since it presents advantages over the induction machines, such as: high efficiency, excellent power density, good mechanical torque/current ratio and small size [13]. It should be remarked that in synchronous machines the speed of the rotor is equal to the speed of the rotor flux. Therefore, θ_1 (angle necessary for the Park transformation) is directly measured by means of position sensors or by means of the integration of the rotor speed [14].

A field-oriented control (FOC) was utilized to control de synchronous machine speed, which enables decoupling the mechanical torque and the components of the magnetization flux, due to simplicity of being able to independently control the currents i_{sd} (associated to the magnetic flux of the machine) and i_{sq} (associated to the mechanical torque exerted by the machine), thanks to its smooth rotor ($Ld = Lq$) [10].

The mathematical model of the permanent magnet synchronous machine in the synchronous reference system is expressed by Equations 5 and 6.

$$V_d = R_s I_d - wL_q I_q + L_d \frac{dl_q}{dt} \tag{5}$$

$$V_q wL_d I_d + R_s I_q + L_q \frac{dI_q}{dt} + \lambda_m \frac{\sqrt{6}}{2} w \tag{6}$$

Where: w is the electric angular speed in (rad/s); λ_m is the flux of the permanent magnets, L_q and L_d are the inductances of the machine in the quadrature and direct synchronous axes, respectively, in (H); R_s is the resistance of the stator of the synchronous machine in (Ω).

The effective power and the torque are expressed by Equations 7 and 8.

$$P_e = w\left[(L_d - L_q)I_q I_d + \lambda_m I_q \frac{\sqrt{6}}{2}\right] \tag{7}$$

$$T_e = p\left[(L_d - L_q)I_q I_d + \lambda_m I_q \frac{\sqrt{6}}{2}\right] \tag{8}$$

Where: p is the number of poles of the synchronous machine.

The relationship between the angular speed of the rotor and the current referred to the quadrature axis, is expressed by Equation 9.

$$\frac{dw_r}{dt} + Bw_r = p\lambda_m I_q \frac{\sqrt{6}}{2} \tag{9}$$

Where: J is the moment of inertia in $(kg \cdot m^2)$, B is the friction coefficient in $(N \cdot m \cdot s)$ and w_r is the mechanical angular speed.

The relationship between the steady-state current in the quadrature axis and the voltage of the capacitor of the direct-current bus is expressed by means of Equation 10.

$$I_{qs} = \frac{V_{DC\_link} I_{dc}}{p\lambda_m \frac{\sqrt{6}}{2} w_r} \tag{10}$$

From the equations of the synchronous machine together with the capacitor referred to the synchronous axis, it is obtained the block diagram shown in Figure 5, where it is observed an internal loop belonging to the current loop in the quadrature axis and two external loops that correspond to the control of the synchronous machine speed and the control of the $V_{DC-link}$ voltage [15].

Figure 5. Control loop of the $V_{DC-link}$ voltage and of the synchronous machine speed.

From Figure 5, G and M are the gains associated to the measured values of current and speed, with unit values, and D, A, C are the transfer functions of the controllers. PI controllers have been used in this application; F is the gain of the PWM, which in this case is a unit gain. H is expressed by equation (1), $Z = \frac{2V_{DC\_medido} I_{dc}}{p\lambda_m \sqrt{6} w_r}$, $T = \frac{p\lambda_m \sqrt{6}}{2}$, $X = \left(\frac{p\lambda_m \sqrt{6}}{2}\right)^2 \left(\frac{1}{Js'+B}\right)$, $K = \frac{1}{Js'+B}$.

For tuning the speed and current loop, it is necessary to know the electric and mechanical parameters of the three-phase synchronous machine; these data are shown in Table 1 [15].

Table 1. Parameters of the permanent magnet synchronous machine

Power (kW)	< 125
Poles	2
Speed (krpm/min)	< 36
Resistance of the stator(Ω)	0,02
Inductance of the stator (μH)	entre 70 y 120
Inertia ($kg \cdot m^2$)	0,633
Coefficient of friction ($N \cdot m \cdot s$)	$4,2 \times 10^{-05}$
External inductance (mH)	1,5

The transfer function required for tuning the PI controller related to the control of the $V_{DC-link}$ voltage is the same given by equations 2 and 3.

Equations 11 and 12 are the result of the simplification of the loops of current and synchronous machine speed.

$$\frac{i_{qs}}{i'_{qs}} = \frac{Es'^2 + Ps' + N}{Qs'^3 + Is'^2 + Ys' + U} \tag{11}$$

Where:

$E = 4JLV_{DC-link}$, $P = (4LBV_{DC-link} + 4JRV_{DC-link})$.
$N = 4RB$, $L = L_{synchronous-machine} + L_{external}$ belonging to the numerator of equation (11).
$Q = 4JL^2$, $I = 4L^2B + 8JRL$, $Y = 8RBL + 6V_{DC-link}p^2\lambda_m^2L$, $U = 4R^2B + 6V_{DC-link}p^2\lambda_m^2R$, $L = L_{synchronous-machine} + L_{external}$ belonging to the denominator of equation (11).

$$\frac{w_r}{i_{qs}} = \frac{1,22p\lambda_m}{Js' + B} \tag{12}$$

The tuning of the PI controllers for the different control loops is carried out by assignment of poles and zeroes, considering the following aspects [11]:

In this work the switching frequency is set at 15 kHz, which limits the dynamics of the current loops, since for frequencies above $\frac{f_{sw}}{2} = 7.5\ kHz$, the modeling technique loses its validity.

From the tuning frequency of the PI for the current loop, it should be tuned a decade below for the remaining control loops.

The phase margin of the Bode plot has to be greater or equal to 60° electrical.

The gain margin is greater than or equal to 7 dB.

Considering these aspects, the following parameters of the PI controllers were obtained:

Control system 1: for the control loop of the direct and quadrature currents, the PI controller has $k_p = 0.36$ and $k_i = 0.09$, for the control loop of the direct current bus $V_{DC-link}$ voltage, the PI controller has $k_p = 51.02$ and $k_i = 0.32$, and for the control loop of the distribution network voltage, the PI controller has $k_p = 36.98$ and $k_i = 4.3$.

Control system 2: for the control loop of the direct and quadrature currents, the PI controller has $k_p = 655$ and $k_i = 166.62$, for the control loop of the $V_{DC-link}$ voltage of the direct current bus the PI controller has the same values as the control system 1, and for the control loop of the synchronous machine speed, the PI controller has $k_p = 9.5$ and $k_i = 0.005$.

The system based in the flywheel has two constraints in the discharge mode:

Minimum voltage level of the $V_{DC-link}$ voltage of the direct current bus, which is calculated by means of Equation 13 [10]. For this work, the minimum voltage is $V_{dc\,minimum} = 639V$.

Discharge depth of the flywheels. This is calculated as the 75 % of its stored energy, which for this case is $w_{r-minimum} = 27rad/s$.

$$V_{DC\_minimmunm} = \frac{2\sqrt{2}V_{f-n(rms)}}{D_q} \tag{13}$$

If the system based on flywheels is below the constraints in discharge mode, the reference current is fixed to a value of 0, so that it does not supply nor absorb power during the occurrence of a voltage sags at the CCP.

3. Results and Discussion

3.1. Performance of the control system

In order to verify the performance of the system based on flywheel, the limits established in section 3 are considered. On that basis, the model of Figure 1 is simulated, without including the system based on flywheel. The resulting voltage level is illustrated in Figure 6.
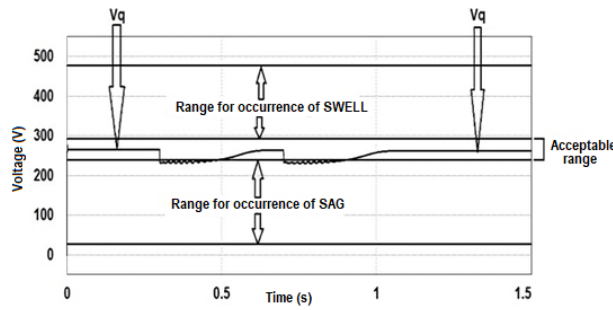
Figure 6. Behavior of the voltage at the CCP at the moment of starting the motors in the distribution network, without the power system based on flywheels.

From Figure 6 it can be seen that before starting the operation of the loads (t < 0,3 s) the voltage level at the CCP is 265.5 V, which is between the acceptable margins established in section 3 and with a current of 13 A (Figure 7), due to the charge of 20 Ω which is connected.

At the moment when the first electric motor starts (t ≥ 0,3 s), a sudden and transient decrease in voltage is observed with a value of 231 V (Figure 6), which demands a peak current of 400 A with a duration time of 0.2 s, as indicated in Figure 7. In this condition, the voltage at the CCP is in the range established for the occurrence of a voltage sag.

The time in which the voltage level enters again in the acceptable range is 0.2 s (Figure 6).

Such behavior occurs again in 0.7 s, because the second motor is connected, with the same value of peak current and stabilization time.
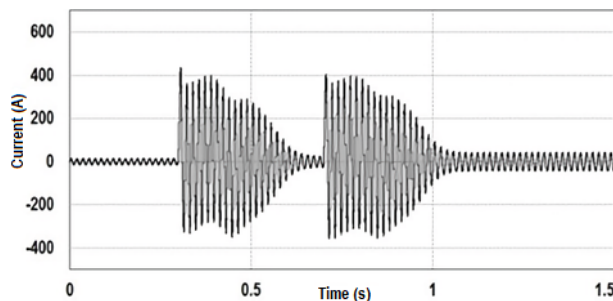
Figure 7. Behavior of the current in phase «A» at the CCP, at the moment of start-up of the electric machine in the distribution network, without the power system based on flywheels.

The connection of the power system based on flywheels is now considered, which supplies energy to mitigate the voltage sags at the CCP, resulting in Figure 8.
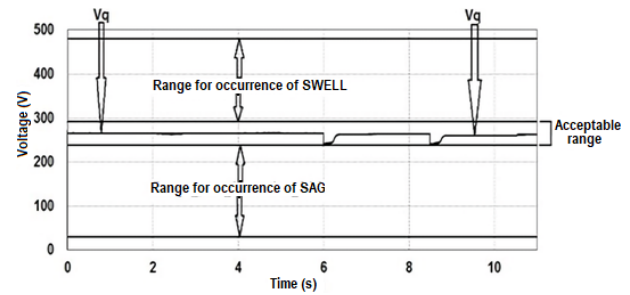
Figure 8. Voltage level by including the power system based on flywheels to mitigate voltage sags at the CCP.

It can be seen in Figure 8 that at the start-up instant of the first motor, which is 6 s, the voltage level is inside the acceptable range established in section 3, with a value of 244 V, compared to the voltage level of Figure 6 it increased 13 V. Similarly, it occurs at 8.5 s when the second motor starts with a voltage level of 244 V at that instant.

It can be seen in Figure 9 the voltage $V_{DC-link}$ and the synchronous machine speed. The following events are observed: before the motors start the voltage $V_{DC-link}$ increases up to a reference value of 900 V, with the associated power converter operating as a rectifier so that the distribution network can absorb power, with its corresponding current loop with negative reference equal to -20 A (Figure 10a).

It is important to remark that in this condition, the current of the system based on flywheel known as I_{filter} is out of phase with the current that circulates through the load (Figure 10a). Similarly, it is observed in Figure 9 that the synchronous machine speed starts to increase up to a reference value of 200 rad/s with the associated power converter operating as an inverter, so that the flywheel absorbs power from the $V_{DC-link}$ voltage source, with its corresponding current loop with positive reference equal to 40 A (Figure 11). In this state the power system based on flywheel is in charging mode.

When the synchronous machine reaches the corresponding reference speed operating as a motor, it consumes a total current of 3.8 A (Figure 11). In this state the power system based on flywheel is in stand-by mode.

At time t ≥ 6 s of Figure 9 it is observed a sudden decrease in the voltage $V_{DC-link}$ with a value equal to 860 V, which is due to the start of the first motor connected to the CCP, and at this instant the associated power converter operates as inverter to supply power to the distribution network, with the corresponding current loop with positive reference equal to 115 A (Figure 10b). An important aspect is that the current supplied to the network by the system based on flywheel, known0 as I_{filter}, is in phase with the current that circulates through the load (Figure 10b).

To avoid that the $V_{DC-link}$ decreases sharply, the synchronous machine starts operating as a generator reducing its velocity up to a value of 164.3 rad/s, delivering power by means of the power converter in rectifier mode to the $V_{DC-link}$ voltage source, with the corresponding current loop with negative reference equal to -100 A (Figure 11).

The decrease of the $V_{DC-link}$ voltage and the machine speed are maintained during the start of the motor, which is of 0.2 s. In this state, the system based on flywheel is in discharge mode.

Once the start time of the motor has passed and when the voltage at the CCP is in the range established in section 3, the $V_{DC-link}$ voltage jointly with the machine speed increase again up to their reference values (Figure 9), and the previously mentioned cycle is repeated again when another voltage sag occurs.
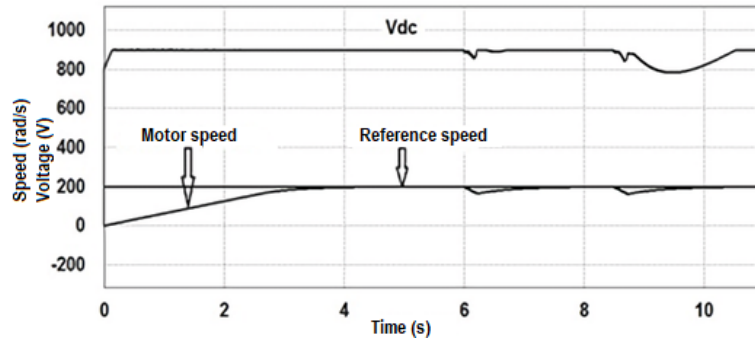
Figure 9. $V_{DC-link}$ voltage and synchronous machine speed.
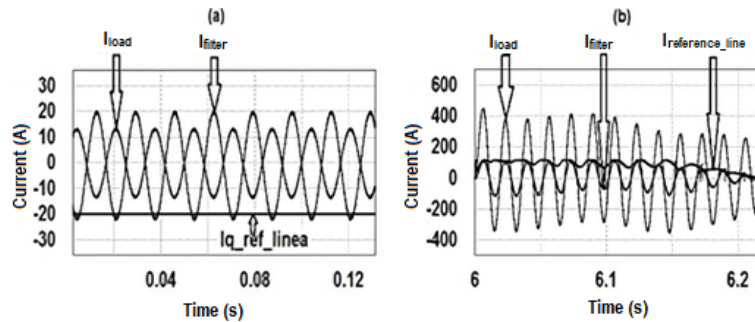
Figure 10. Reference current of the power system based on flywheels: a) charge mode, b) discharge mode.
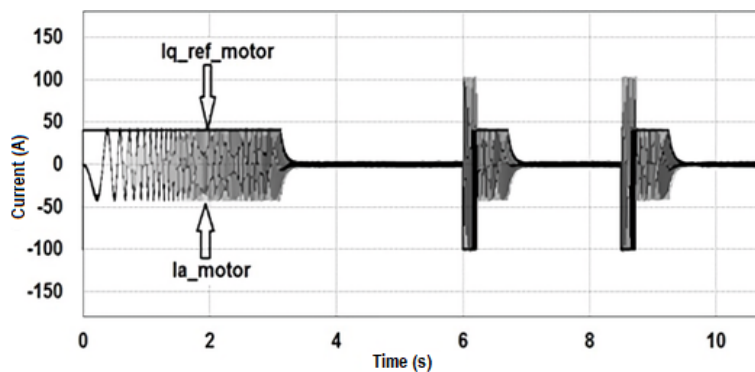
Figure 11. Reference current for the synchronous machine.

Orellana Uguña et al. / Control of a System of Energy based on Flywheel to mitigate the Voltage Gaps at the Point of Common Coupling

57

Another important aspect is the THD level at the charge, stand-by and discharge moments of the system based on flywheel. After the simulation test, the following results were obtained: 1) regarding the THD of the current that circulates to the load it was obtained 2.4 %, less than the established which is 8 % (standards CONELEC 004/01, NP EN 50160-2010), 2) regarding the THD of the voltage measured at the CCP it was obtained 2.4 %, less than the established in the standard, 3) regarding the THD of the current that circulates to the system based on flywheel it was obtained 3.4 %, less than the established in the standard.

4. Conclusions

The present paper carries out a study about the voltage levels caused by the incorporation to a distribution network of a power system based on flywheels, in the presence of voltage sags caused by the entry of transient loads to the electrical network.

According to the results presented, it can be concluded that the voltage level is regulated in the distribution network, when the system is loaded with the presence of loads in the electrical network.

The system exhibits a response time smaller than milliseconds, thus avoiding the occurrence of voltage sags in the CCP at the moment when important loads connected to the network are started.

Another important aspect is that the power system based on flywheel does not affect the THD levels of the voltage and current at the CCP.

A limitation of this system is that it will not be able to compensate a voltage swell once the nominal load condition is reached, because it will not have additional capacity to absorb the excess power at the CCP, since both the voltage of the direct current bus and the synchronous machine speed already reached their nominal values.

If no actions are taken, the useful life of each of the components of the system will deteriorate, shortening its operating time.

A problem of this system is that, if the voltage level of the direct current bus and the synchronous machine speed are below the minimum allowed values, the system will not be able to supply energy to avoid the occurrence of voltage sags, and if at that instant the control systems behaves incorrectly, the system based on the flywheel will start absorbing power from the network thus entering in the charge mode, involving directly a more severe decrease of the voltage level at the CCP.

To overcome this problem, an auxiliary power supply system must be installed in parallel, which should consist of a control system that jointly monitors: the voltage level of the direct current bus, the synchronous machine speed and the distribution network voltage, since in this way, when the system based on the flywheel and the distribution network are below the allowed values, it starts supplying power to avoid the occurrence of voltage sags at the CCP.

Acknowledgement

References

[1] N. S. Gayathri, N. Senroy, and I. N. Kar, "Smoothing of wind power using flywheel energy storage system," *IET Renewable Power Generation*, vol. 11, no. 3, pp. 289–298, 2017. [Online]. Available: https://doi.org/10.1049/iet-rpg.2016.0076

[2] D. O. Akinyele and R. K. Rayudu, "Review of energy storage technologies for sustainable power networks," *Sustainable Energy Technologies and Assessments*, vol. 8, pp. 74–91, 2014. [Online]. Available: https://doi.org/10.1016/j.seta.2014.07.004

[3] S. Gayathri Nair and N. Senroy, "Power smoothening using multi terminal dc based dfig connection and flywheel energy storage system," in *2016 IEEE 6th International Conference on Power Systems (ICPS)*, 2016, pp. 1–6. [Online]. Available: https://doi.org/10.1109/ICPES.2016.7584134

[4] J. A. Guacaneme, D. Velasco, and C. A. L. Trujillo, "Revisión de las características de sistemas de almacenamiento de energía para aplicaciones en micro redes," *Información tecnológica*, vol. 25, pp. 175–188, 00 2014. [Online]. Available: https://bit.ly/3bMXPsE

[5] D. R. Aitchison, M. Cirrincione, and N. Leijtens, "Design development of a flywheel energy storage system for isolated pacific island communities," in *2016 IEEE International Conference on Advanced Intelligent Mechatronics (AIM)*, 2016, pp. 1628–1633. [Online]. Available: https://doi.org/10.1109/AIM.2016.7577003

[6] J. Itoh, T. Masuda, D. Sato, T. Nagano, T. Suzuki, and N. Yamada, "Development of magnetic assist system in flywheel energy storage system for power load-leveling," in *2016 IEEE International Conference on*

Renewable Energy Research and Applications (ICRERA), 2016, pp. 198–203. [Online]. Available: https://doi.org/10.1109/ICRERA.2016.7884537

[7] X. Zhang and J. Yang, "A robust flywheel energy storage system discharge strategy for wide speed range operation," *IEEE Transactions on Industrial Electronics*, vol. 64, no. 10, pp. 7862–7873, 2017. [Online]. Available: https://doi.org/10.1109/TIE.2017.2694348

[8] F. Franco Hernández and H. Valdés Carrillo, *Minería artesanal del oro de aluvión en Mocoa, Putumayo, Amazonia colombiana.* Universidad Nacional de Colombia, 2005. [Online]. Available: https://bit.ly/2zTe5uL

[9] G. V. Deshpande and S. S. Sankeshwari, "Speed control of induction motors using hybrid pi plus fuzzy controller," *International Journal of Advances in Engineering & Technology, IJAET*, vol. 6, no. 5, pp. 2253–2261, 2013. [Online]. Available: https://bit.ly/3dYCspA

[10] L. G. González Morales, "Mejora de la eficiencia y de las prestaciones dinámicas en procesadores electrónicos de potencia para pequeños aerogeneradores sincrónicos operando en régimen de velocidad variable," Ph.D. dissertation, 2011. [Online]. Available: https://bit.ly/2Tqfksm

[11] F. A. Bardemaker, "Modulação vetorial aplicada a retificadores trifásicos PWM unidirecionais," Ph.D. dissertation, 2006. [Online]. Available: https://bit.ly/3e5gsta

[12] A. S. de Morais, F. Lessa Tofoli, and I. Barbi, "Modeling, digital control, and implementation of a three-phase four-wire power converter used as a power redistribution device," *IEEE Transactions on Industrial Informatics*, vol. 12, no. 3, pp. 1035–1042, 2016. [Online]. Available: https://doi.org/10.1109/TII.2016.2544248

[13] S. M. de Pancorbo, G. Ugalde, J. Poza, and A. Egea, "Comparative study between induction motor and synchronous reluctance motor for electrical railway traction applications," in *2015 5th International Electric Drives Production Conference (EDPC)*, 2015, pp. 1–5. [Online]. Available: https://doi.org/10.1109/EDPC.2015.7323219

[14] M. Bhardwaj, *Sensored Field Oriented Control of 3-Phase Permanent Magnet Synchronous Motors.* Texas Instruments, 2013. [Online]. Available: https://bit.ly/3gahvKc

[15] S. Talebi Rafsanjan, "Advanced high-speed flywheel energy storage systems for pulsed power application." Ph.D. dissertation, 2008. [Online]. Available: https://bit.ly/3cPPO7j

DETECTION OF SUDDEN CARDIAC DEATH USING THE ADAPTIVE SPECTRAL METHOD ON THE T WAVE: AN EXPERIMENTAL STUDY ON PUBLIC DATABASES

DETECCIÓN DE LA MUERTE SÚBITA CARDÍACA USANDO EL MÉTODO ESPECTRAL ADAPTATIVO SOBRE LA ONDA T: ESTUDIO EXPERIMENTAL SOBRE BASES DE DATOS PÚBLICAS

Marco Flores-Calero[1,*,2], Melisa Pilla-Barroso[3]

Abstract

T-wave alternans (TWA) analysis is one of the main techniques for determining whether an individual is at risk of sudden cardiac death (SCD). Among the existing methods for determining TWA is the adaptive spectral method (SM-Adaptive), which uses time-frequency distributions (TFD) for the analysis. The objective of the study is to apply the method on main public databases in order to detect the presence or absence of alternations, and to obtain quality parameters of the aforementioned method. The method was tested on synthetic signals, 90 signals without TWA and 450 with TWA; on the other hand, 10 signals from Physionet's TWADB database belonging to healthy patients and 26 signals from patients with risk factors associated to SCD were used. Tests with synthetic signals showed a sensitivity of 94.89%, specificity of 92.22% and accuracy of 94.44%. As for the tests in the database, the method exhibits an accuracy of 80.56%, which indicates that the SM-Adaptive method enables detecting TWA with an acceptable accuracy and, in addition, it shows greater robustness against noise and stationary data.

Resumen

El análisis de la alternancia de la onda T (TWA, T-wave alternants) constituye una de las principales técnicas para determinar la presencia del síndrome de muerte súbita cardíaca (MSC). Entre los métodos existentes para determinar TWA se encuentra el método espectral adaptativo (SM-Adaptivo), el cual utiliza distribuciones en tiempo-frecuencia (TFD, time-frecuency distribution) para el análisis. El objetivo del estudio es aplicar este método sobre las principales bases de datos públicas con el fin de detectar la presencia o ausencia de alternancias y obtener parámetros de calidad del método en mención. El método fue probado en señales sintéticas, 90 señales sin TWA y 450 con TWA; por otro lado, se utilizaron 10 señales de la base de datos TWADB de Physionet pertenecientes a pacientes sanos y 26 señales de pacientes con factores de riesgo asociados a la MSC. En las pruebas con señales sintéticas se obtuvo una sensibilidad de 94,89 %, especificidad de 92,22 % y exactitud de 94,44 %. En cuanto a las pruebas en la base de datos el método presenta una exactitud del 80,56 %, lo que indica que el método SM-Adaptivo permite detectar TWA con una exactitud aceptable, además, que presenta mayor robustez frente a ruido y a la estacionariedad de datos.

[1,*]Departamento de Eléctrica, Electrónica y Telecomunicaciones, Universidad de las Fuerzas Armadas, Sangolquí, Ecuador. Corresponding author ✉: mjflores@espe.edu.ec. ⓘ http://orcid.org/0000-0001-7507-3325
[2]Departamento de Sistemas Inteligentes, Tecnología I&H, Latacunga, Cotopaxi, Ecuador.
[3]Profesional en libre ejercicio, Quito, Ecuador. ⓘ http://orcid.org/0000-0002-1441-1236

1. Introduction

The sudden cardiac death (SCD) is an event that causes the death in a fast and unexpected manner of an apparently healthy individual, or with a known cardiac disease but with low death probability. The SCD is produced by an electric instability of the heart, which prevents the occurrence of a heartbeat and, as a consequence, the heart stops pumping blood to the rest of the body. This produces a lack of blood flow to the brain, with causes the loss of oxygen; this gives rise to an abrupt loss of consciousness, and the death of the individual.

Among the main causes of the SCD are the cardiovascular problems [1]. The cardiac diseases that are more related to the SCD are the following: coronary artery disease, cardiomyopathies, electrophysiological anomalies, heart valve disease and congenital cardiac anomalies, among others [2].

Similarly, it is estimated that the SCD is responsible for 3 to 7 million of deaths worldwide every year [2,3]. In Latin American countries there are no official records related to the SCD, which prevents knowing its incidence in a precise manner. The reports about this problem are not uniform, since the SCD constitutes a multifactorial problem and varies according to the age. In addition, there is the possibility that it continues to increase as a result of the increment of the coronary diseases (smoking, obesity, diabetes mellitus, high blood pressure, high cholesterol levels), thus becoming an important unresolved challenge.

At present, the therapies mostly used to prevent the SCD are the medication and the implantable cardioverter-defibrillator (ICD) [3], however, since they are invasive and high cost tests, it is evident the search for techniques that enable a fast detection of this type of phenomena of great interest in the social and technological areas.

The ECG is one of the tools mostly used for the study and diagnosis of heart diseases. It enables recording the electrical activity of the heart by placing electrodes on the body surface, such that it is obtained a sequence of heartbeats described in a set of waveforms (P, Q, R, S, T), segments and complexes [4,5].

The existing mechanisms to measure the electrical instability of the heart in the ECG include the QT prolongation, QT dispersion, late potentials, T-wave alternans (TWA) and heart rate turbulence [6]. The TWA has been used for the analysis of the ventricular repolarization, which manifests in the ECG as periodic fluctuations of the T-wave amplitude [7].

The TWA estimation implies measuring, beat-to-beat, the variability of the amplitude, duration and shape of the ST-T segment of the ECG record [8]. The TWA signal is generally in the range of microvolts; therefore, it is necessary to use advanced digital signal processing techniques and computational algorithms for its detection.

In recent years, various TWA analysis procedures have been proposed. The techniques mostly used have been developed in time-domain, among which there is the moving average method (MAM), which calculates the TWA value using the difference of the mean value of even and odd beats [9]; another method is the correlation method (CM), which detects alternans using the cross-correlation [10]. The methods developed in frequency-domain include, among others, the spectral method (SM), which utilizes the discrete Fourier transform (DFT) to analyze the frequency component at 0.5 cycles per beat (cpb) [11]. A similar method is complex demodulation (CD), which fits a sinusoidal signal at the frequency of 0.5 cycles per beat of the aligned T-waves [12]. The main drawback of these methods is that they are very sensitive to signals with noise. Recently, artificial intelligence techniques are being used for SCD classification [5].

With the purpose of overcoming the limitations of the methods previously described, Ghoraani *et al.* [13] propose a method called Adaptive-SM for detection and quantification of TWA, which is based on the process of the SM method and carries out the analysis of TWA using time-frequency distributions; hence, it enables representing the spectral variations of TWA along time, and at the same has the capability of following nonstationary structures. On the other hand, it utilizes the non-negative matrices factorization (NMF) with the purpose of separating the noise from the TWA signal, so that the detection capability is improved.

The main objective in this work is evaluating the performance of the Adaptive-SM method in different scenarios. In order to achieve this objective, a set of synthetic signals (simulations) with and without added TWA of variable amplitudes, and with different levels of noise, have been utilized. The first group, i.e., the synthetic signals with added TWA were generated from five base signals to which alternans with different amplitudes have been added: $10\mu V$, $20\mu V$, $50\mu V$, $100\mu V$ and $200\mu V$. Therefore, there are 25 signals available; the alternans are generated from three wave shapes: Gaussian, triangular and rectangular, which results in 75 signals. At last, five different levels of Gaussian white noise were added to all ECG signals, with SNR: 10, 20, 30, 40 and 50. These signals together with the noise-free signals resulted in a total of 450 test signals. For the second group, constituted by synthetic signals with TWA, five signals were taken as base, with three different wave shapes (15 signals) and five noise levels. Therefore, together with the noise-free signals, 90 signals were obtained. Hence, between the two groups there is a total of 540 synthetic test signals. Then, the test on real signals was developed for which the Adaptive-SM method was applied to 36 signals of Physionet's TWADB database. The signals belong to healthy patients and to patients that have the risk of

Flores-Calero y Pilla-Barroso / Detection of sudden cardiac death using the adaptive spectral method on the T wave: An experimental study on public databases

61

SCD. The TWA magnitude was calculated with the purpose of determining the existence or absence of alternans of the test signal. This enabled to establish values of sensitivity, specificity and accuracy. In addition, a comparison of such parameters was carried out with the SM and MAM methods which are available in the TWAnalyser software [14].

2. Materials and methods

The present work is focused on the analysis of heart signals; 540 synthetic signals and 36 signals from the TWADB database, with the purpose of detecting TWA in the signals using the Adaptive-SM method, and then, obtaining the quality parameters of the algorithm, to evaluate its performance.

Initially, the method requires a preprocessing stage to filter the signals, and to detect and segment the characteristic points of the ECG signal.

Then, the Adaptive-SM method is applied followed by the NMF technique, with the purpose of detecting the presence or absence of alternans in the signal. This enables the classification of the signals with and without TWA. Figure 1 shows the stages of the proposed methodology.
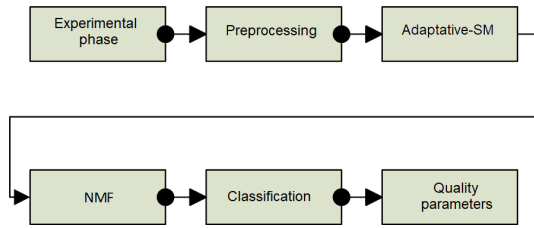
Figure 1. Proposed methodology for the detection of SCD.

This procedure enables obtaining the quality parameters of the model, namely sensitivity, specificity and accuracy.

2.1. Development of the experimental phase

First, it was tested the performance of the algorithm on 450 synthetic signals, which represent signals without TWA, with different noise levels and variable alternan amplitude. In addition, a second group of 90 signals without added TWA, i.e., with amplitude $0\mu V$ and different noise levels.

Then, 36 signals taken from the T-Wave Alternans Database (TWADB) presented in [15] were selected, which includes signals belonging to healthy patients and patients with risk factors associated to SCD. The ECG records have been sampled at 500 Hz with an approximate duration of two minutes.

The 36 signals are divided as follows, 10 signals corresponding to healthy patients, and the remaining 26 signals of patients with risk factors associated to SCD, these records have been obtained from patients with myocardial infarctions, transient ischemia, and ventricular tachyarrhythmias, among others.

2.2. Preprocessing

In general, heart signals have noise that disturbs and distorts the information contained in the signal. The noise is caused by external interferences, such as the body movement, breathing and muscle spasms, bad placement of the electrodes, etc. This is why a robust preprocessing stage is required, which includes the elimination of noise, the removal of interferences at different external frequencies and the correction of the baseline deviation [4].

The methods utilized should guarantee that an appropriate filtering is carried out, as well as that there is no loss of relevant information, since the alternans are often confused with noise components because they are in the level of microvolts. In this case, the aim is to maintain the alternans characteristics, and at the same time, eliminate noise.

On the other hand, as a prerequisite for the Adaptive-SM method, it is necessary to extract the ST-T segment from every beat. Therefore, a method for extracting the characteristics is required, and another for segmentation of the different waves, segments and complexes that constitute the ECG signal [5].

2.3. Description of Adaptive-SM

The Adaptive-SM method utilizes time-frequency distributions (TFD) to obtain a representation of the frequency components of the signal along time. It is constituted by two stages, (i) alignment and (ii) estimation of the adaptive TFD.

2.3.1. Alignment

With the aligned waves it is constructed a matrix A, as shown in Equation 1, of dimension M × N, where M is the number of beats, in this case 128, and N is the length of the segment ST-T.

$$A = \begin{bmatrix} T_1(1) & T_1(2) & \cdots & T_1(N) \\ T_2(1) & T_2(2) & \cdots & T_2(N) \\ T_3(1) & T_3(2) & \cdots & T_3(N) \\ \vdots & \vdots & \cdots & \vdots \\ T_M(1) & T_M(2) & \cdots & T_M(N) \end{bmatrix} = \begin{bmatrix} A_1 & A_2 & \cdots & A_N \end{bmatrix}$$

(1)

The rows represent the ST-T segments of each beat and the columns describe the beat-to-beat variations of the ST-T segment. The graphical representation of alignment matrix A is shown in Figure 2.
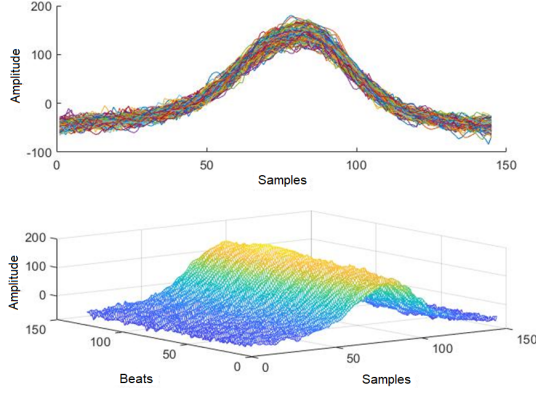
Figure 2. Aligned ST-T segments (128 segments) with a length of 132 samples, of the signal TWADB55.

Figure 3. Average adaptive TFD of the TWADB55 signal corresponding to a healthy patient; it is observed low alternan values at 0.5 cpb.

2.3.2. Adaptive TFD

TFD is a two-dimensional representation of the signal energy in terms of time and frequency. The adaptive TFD method utilizes the Matching Pursuit algorithm to decompose a signal x in time-frequency atoms. Once the signal is decomposed, the Wigner-Ville distribution is used to obtain the energy distribution in the time-frequency domain, using Equation 2.

$$V(t,f) = \sum_{i=1}^{I} |\alpha_{\gamma i}|^2 \, WVG_{\gamma i}(t,f) \qquad (2)$$

Matrix Vi is generated applying the Adaptive TFD method to matrix A, and then a matrix defined by Equation 3 is constructed calculating the average.

$$V_{\frac{M}{2} \times M} = \frac{1}{N} \sum_{i=1}^{N} V_i \qquad (3)$$

The TWA magnitude is calculated taking the energy values at 0.5 cycles per beat. The energy at 0.5 cycles per beat T(t) and the energy values of the noise present in the interval 0.36 to 0.49 cycles per beat, are required to estimate the TWA value.

Figures 3 and 4 show a graphical representation of the adaptive TFD on two heart signals of the TWADB database [15].

Figure 4. Average adaptive TFD of the TWADB12 signal corresponding to a patient with risk factors of SCD; it is observed low alternan values at 0.5 cpb, however, between samples 20 and 40 there is a possible alternan component.

2.4. Non-negative matrices factorization

A new matrix $V_{l \times M'}$ is constructed in this stage, where in this case $I = 16$ and M is equal to the length of the analysis window, 128 in this case. NMF factors the input matrix V in two matrices $W_{m \times r}$ and $H_{r \times n}$ of smaller size. Taking the value $r = 3$, three vectors W_1, W_2 and W_3 are determined. The representative components of the TWA magnitude are grouped in a single vector represented as W_t .

The TWA magnitude is expressed according to Equation 4, and thus it is possible to separate the alternans components of the noise.

$$TWA = w_t h_t \tag{4}$$

At last, the TWA value of vector w_t is calculated, which is the component with the greatest TWA magnitude, according to equation 5.

$$f = Real\sqrt{T - \mu_{noise}} \tag{5}$$

Figures 5 and 6 show the separation of the alternans components of the noise. The upper graph indicates the alternan components, and the lower part shows the noise extracted from the signal.
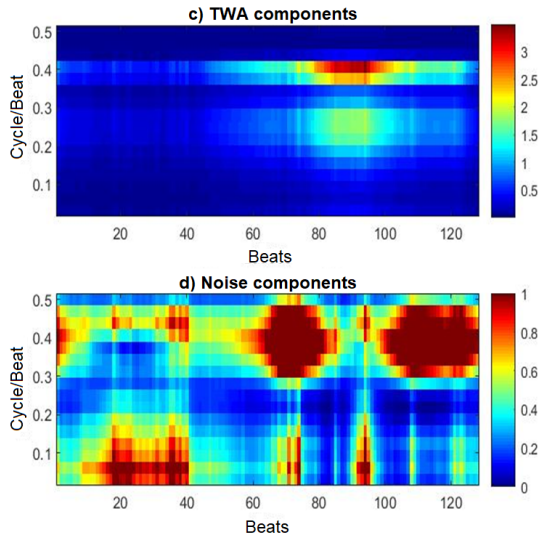
Figure 5. Decomposition of the TWADB55 signal in its alternan and noise components.
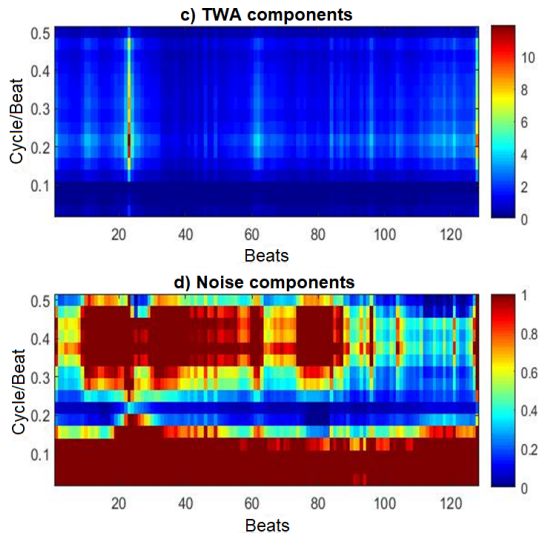
Figure 6. Decomposition of the TWADB12 signal in its alternan and noise components.

Figures 7 and 8 correspond to the signal factorized in three components; the component with the greatest TWA magnitude is indicated in the graph.
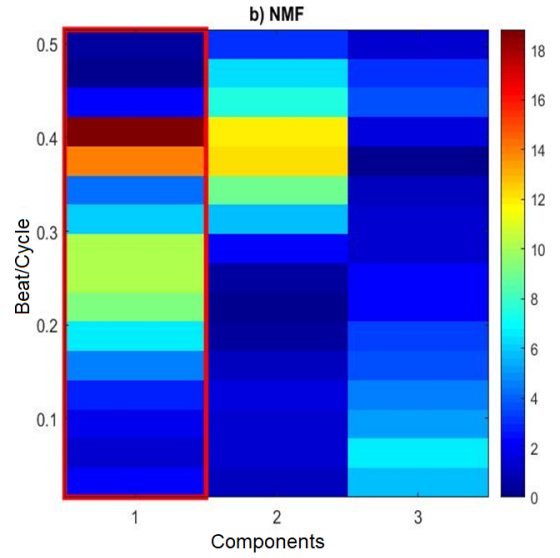
Figure 7. Component with the greatest TWA magnitude of the TWADB55 signal, the TWA is calculated at 0,5 bcpl.
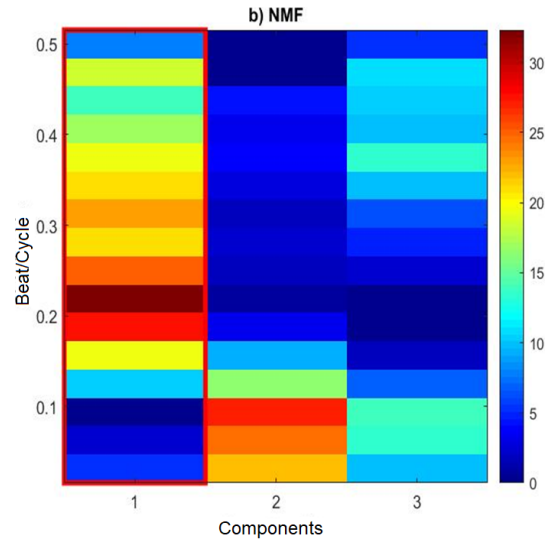
Figure 8. Component with the greatest TWA magnitude of the TWADB12 signal, the TWA is calculated at 0,5 bcpl.

2.5. Classification

Immediately after calculating the TWA magnitude, a threshold value (Th) of $1,5\ \mu V$ is established. Then, the signals are classified according to the hypothesis given by Equation 6.

$$\begin{aligned} f > Th &\Rightarrow H_0 \\ f < Th &\Rightarrow H_1 \end{aligned} \tag{6}$$

Where H_0 indicates presence of TWA in the signal, and inversely, H_1 indicates absence of TWA.

3. Results and discussion

3.1. Tests with synthetic signals

This first test was carried out with the purpose of evaluating the performance of the Adaptive-SM method on synthetic signals, which simulate heart signals, to which artificial alternans and noise have been added, at different levels.

The scheme of Figure 9 shows the synthetic signals used, divided in two groups, and the process necessary to find the quality parameters.
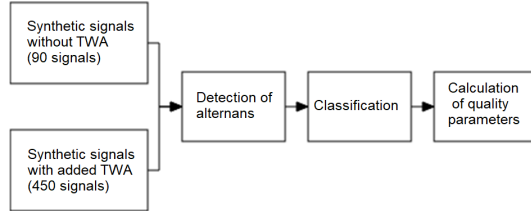
Figure 9. Process for obtaining the quality parameters using synthetic signals with and without added TWA.

Initially, the SM-Adaptive method was evaluated in 90 synthetic signals without TWA, i.e., signals that simulate heart signals without the presence of alternans, which correspond to healthy individuals. The results of the classification obtained applying the method to the 90 signals can be found in Table 1, the values are presented according to the different levels of noise.

Table 1. Classification of the synthetic signals without TWA according to the levels of added noise

SNR (dB)	VN	FP
Without noise	15 (100 %)	0 (0 %)
50	15 (100 %)	0 (0 %)
40	15 (100 %)	0 (0 %)
30	15 (100 %)	0 (0 %)
20	12 (80 %)	3 (20 %)
10	11 (73,33 %)	17 (26,67 %)
Total	**83 (92,22 %)**	**23 (7,78 %)**

As a result, 83 true negatives (TN) and 7 false positives (FP) were obtained. In this case, the true negatives indicate that a signal without TWA has been effectively classified as a signal without TWA; on the other hand, the false positives indicate that a signal without TWA has been classified as a signal with TWA.

Table 1 shows that the signals without the presence of any type of noise, which does not occur in real signals, have been correctly classified. It occurs similarly with the signals with high SNR values, 50, 40 and 30, which correspond to low noise levels (amplitude of the noise), since they are inversely proportional. The classification of the signals starts generating false results

for lower values of SNR, it is seen that for SNR of 20 and 10 the number of false positives is 3 and 17, respectively, i.e., for these values of SNR the classification does not show a 100 % accuracy and in any case it has been reduced up to 73.33 % for the signals with the lowest SNR value. This indicates that the algorithm is sensitive to high levels of noise (low SNR), in particular for values of SNR smaller than 20.

However, when calculating the specificity of the method which was found to be 92.22 %, the Adaptive-SM method has been capable of appropriately classifying signals without TWA (healthy individuals), even with high noise levels.

Continuing with the tests on synthetic signals, 450 synthetic signals with TWA artificially added have been taken, which represent individuals with risk factors associated to the SCD.

The results of the classification are shown in Tables 2 and 3. In Table 2 the results are divided according to the noise level, while Table 3 shows the results according to the amplitude of the added alternans.

Table 2. Classification of the synthetic signals with TWA according to the added noise levels

SNR(dB)	VP	FN
Without noise	75 (100 %)	0 (0 %)
50	75 (100 %)	0 (0 %)
40	75 (100 %)	0 (0 %)
30	74 (98.66 %)	1 (1,34 %)
20	70 (93.33 %)	5 (6,67 %)
10	58 (77,33 %)	17 (22,67 %)
Total	**427 (94,89 %)**	**23 (7,78 %)**

Table 3. Classification of the synthetic signals with TWA according to the amplitude of the added alternans

Amplitude (μV)	VP	FN
10	76 (84,44 %)	14 (15,56 %)
20	85 (94,44 %)	5 (5,56 %)
50	87 (96,67 %)	3 (3,33 %)
100	89 (98,89 %)	1 (1,11 %)
200	90 (100 %)	0 (0 %)
Total	**427 (94,89%)**	**23 (5,11 %)**

As a result of the classification carried out by the Adaptive-SM method, there are 427 tests diagnosed as true positives and 23 as false negatives. The true positives indicate that a signal with TWA has been correctly classified, and on the contrary, the false negatives indicate that a signal with TWA has been classified as a signal without TWA.

Table 2 includes the responses of the method for signals with different noise levels. A noise-free signal is diagnosed with an accuracy of 100 %, and similar

Flores-Calero y Pilla-Barroso / Detection of sudden cardiac death using the adaptive spectral method on the T wave: An experimental study on public databases

65

results are achieved for SNR values of 50 and 40, i.e., as the SNR value of the signal is greater, the method shows more accurate results. For SNR values of 30 dB, 20 dB and 10 dB, the classification starts to give wrong results; it is the case that for these values of SNR there are 1, 5 and 17 false negatives, respectively. Therefore, the method is more sensitive for values of SNR smaller than 30 dB, resulting in false detections.

Table 3 shows the resulting classification for different values of alternans. For an amplitude of 200 µV the detection is made with an accuracy of 100 %, which indicates that, as the alternans contained in the signal are greater, it is simpler for the algorithm to detect them. As the amplitude of the alternans decreases, also does the detection percentage, and for 10 µV it has decreased up to 84.44 %, i.e., the method shows difficulties in detecting a very small alternan wave, which could be due to the fact that such wave is being confused with noise or another type of interference.

From the known values of true positives and false negatives, the value of sensitivity was determined as 94.89 %, an acceptable value, which shows that the method has a high probability of correctly classifying a signal with TWA (individuals with risk of SCD). Therefore, the method has been capable of performing a correct classification with an accuracy of 94.44 %, which indicates that it has a high probability of diagnosing correctly signals with and without TWA, with different levels of noise and variable alternans.

3.2. Tests with signals from the TWADB database

A second way for evaluating the performance of the Adaptive-SM method was conducted utilizing real signals from the Physionet's TWADB database. The selected signals correspond both to healthy individuals and to individuals with risk of SCD, as shown in the scheme in Figure 10.
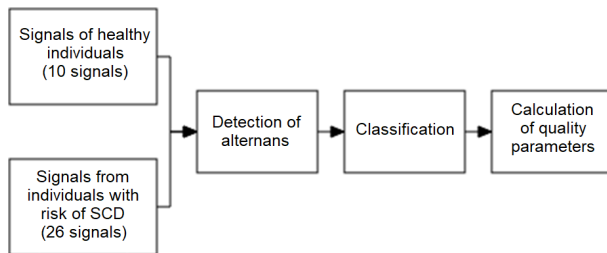
Figure 10. Process for obtaining the quality parameters using signals from the TWADB database.

The tests were carried in two groups of analysis, on one side, ten signals from healthy patients were taken, i.e., signals that do not contain alternans. Once the Adaptive-SM method is applied to these signals, the classification shown in Table 4 is obtained as a result, which has the following information: name of the signal

chosen, calculated value of the detected alternan and the diagnosis generated, true negative or false positive.

Table 4. Results given by the Adaptive-SM method in signals of healthy individuals

Signal	TWA Value	Diagnosis
twa39	0	VN
twa46	8,3949	FP
twa55	0	VN
twa60	0	VN
twa10	0	VN
twa23	0	VN
twa61	0	VN
twa62	0	VN
twa71	0	VN
twa93	27,1057	FP

The method classified 8 of 10 signals as signals without TWA, i.e., there are 8 true negatives and 2 false positives. This indicates that the method is capable of correctly detecting a signal without TWA and, therefore, a healthy individual (specificity), with a probability of 80 %.

The other group of analysis is constituted by 26 signals corresponding to patients with risk of SCD. The results are shown in Table 5, which has the following information: name of the signals, calculated TWA value, in µV, and diagnosis of the detection.

In the case of signals with risk of SCD, of the 26 signals, 5 were classified as signals without TWA, i.e., there are 5 false negatives; on the other hand, the remaining 21 signals have been correctly classified, and thus there are 21 true negatives. With the number of true positives and false negatives, the sensitivity of the method has been calculated resulting in 80.76 %, i.e., it has a high probability of correctly detecting signals without TWA and, therefore, individuals with risk of SCD.

According to the data of Tables 4 and 5, there are 29 signals correctly classified of a total of 36 signals, among signals with and without TWA, which results in an accuracy of the method of 80.56 %, i.e., the method has a high probability of correctly detecting and classifying signals with and without TWA.

Table 5. Results given by the Adaptive-SM method in signals of patients with risk of SCD

Signal	TWA Value	Diagnosis
twa07	8,1842	VP
twa32	8,0292	VP
twa85	0	FN
twa92	3,6081	VP
twa00	0	FN
twa08	0	FN
twa45	40,2243	VP
twa63	1,8172	VP
twa68	4,1085	VP
twa95	6,5078	VP
twa12	0	FN
twa27	0	FN
twa03	24,1159	VP
twa11	9,8338	VP
twa18	6,7598	VP
twa19	6,1028	VP
twa20	0	FN
twa31	10,3374	VP
twa36	6,6947	VP
twa40	0	FN
twa41	5,6962	VP
twa48	8,1214	VP
twa49	4,0385	VP
twa53	2,6401	VP
twa54	53,9866	VP
twa83	9,1466	VP

Subsequently, in this work a comparison was made between the Adaptive-SM method and the SM and MMA methods; these latter are implemented in the TWAnalyser software [14]

The 36 signals previously described were taken for this experiment. The results of specificity, sensitivity and precision are shown in Table 6.

The MMA method is the one that exhibits more problems, since its sensitivity of 100 % and specificity of 0 % suggests that it classifies all signals as signals with TWA, although they do not have alternans. Then, this method considers any type of disturbance as an alternan, which is wrong, and this is the reason why the methods classifies incorrectly 50 % of the test signals. On the other hand, the SM method shows a more balanced performance, however, when compared to the Adaptive-SM the percentage of accuracy in the classification is considerably smaller, with a precision of only 63.89 %. The Adaptive-SM method results a more acceptable method with a balanced behavior in the detection of signals with and without TWA.

Table 6. Quality parameters of the Adaptive-SM, SM and MMA methods

Parameter	Adaptative-SM	SM	MMA
Sensitivity	80,76%	61,53%	100%
Specificity	80%	70%	0%
Precision	80,56%	63,89%	50%

From the results in both types of tests, i.e., on synthetic signals and records from the TWADB databases, these indicate a better performance of the Adaptive-SM method with respect to the other two methods, in all quality indices. Specifically, the Adaptive-SM algorithm is characterized by its robustness in the detection of alternans.

4. Conclusions

The extensive experiments showed that the Adaptive-SM method is capable of correctly detecting alternans and classifying the signals. In addition, it could be compared, by means of standard metrics, the performance of the algorithm when subject to different noise and alternans levels, exhibiting advantages with respect to the classical SM and MMA methods. This superiority is because the Adaptive-SM utilizes time-frequency distributions that enable a more detailed analysis of the signal, thus avoiding the loss of relevant information contained in the heart signal and, therefore, yielding better results in the detection of alternans.

In conclusion it could be indicated that the Adaptive-SM is a promising technique for the early and non-invasive detection of the SCD.

In a future work it will be studied the capability of the algorithm for long-term analysis, and its performance in mobile monitoring systems intended to eHealth; all this accompanied with the criterion of an expert cardiologist specialized in SCD.

Acknowledgements

References

[1] M. Vargas Sanabria, J. C. Vega Chaves, G. Hern A¡ndez Romero, and G. Montero Solano, "Síndrome de brugada como casusa de muerte súbita de origen cardíaco," *Medicina Legal de Costa Rica*, vol. 34, pp. 157–164, 03 2017. [Online]. Available: https://bit.ly/2ZEI4Sf

[2] R. Devi, H. K. Tyagi, and D. Kumar, "Early stage prediction of sudden cardiac death," in *2017 International Conference on Wireless Communications, Signal Processing and Networking (WiSPNET)*, 2017, pp. 2005–2008. [Online]. Available: https://doi.org/10.1109/WiSPNET.2017.8300112

[3] J. T. Willerson, J. N. Cohn, H. J. J. Wellens, and D. R. Holmes, *Cardiovascular Medicine*, ser. SpringerLink : Bücher. Springer London, 2007. [Online]. Available: https://bit.ly/3eag8cD

[4] U. Satija, B. Ramkumar, and M. S. Manikandan, "Automated ecg noise detection and classification system for unsupervised healthcare monitoring," *IEEE Journal of Biomedical and Health Informatics*, vol. 22, no. 3, pp. 722–732, 2018. [Online]. Available: https://doi.org/10.1109/JBHI.2017.2686436

[5] F. Panjaitan, S. Nurmaini, M. Akbar, A. H. Mirza, H. Syaputra, T. B. Kurniawan, and R. Umi P, "Identification of classification method for sudden cardiac death: A review," in *2019 International Conference on Electrical Engineering and Computer Science (ICECOS)*, 2019, pp. 93–97. [Online]. Available: https://doi.org/10.1109/ICECOS47637.2019.8984465

[6] E. V. Garcia, C. A. Pastore, N. Samesima, and H. G. Pereira Filho, "T-wave alternans: desempenho clínico, limitações, metodologias de análise," *Arquivos Brasileiros de Cardiologia*, vol. 96, pp. e53–e61, 03 2011. [Online]. Available: http://dx.doi.org/10.1590/S0066-782X2011005000018

[7] Y. Karplyuk, K. Ivanko, and N. Ivanushkina, "Peculiarities of t wave alternans detection and evaluation," in *2015 IEEE 35th International Conference on Electronics and Nanotechnology (ELNANO)*, 2015, pp. 356–361. [Online]. Available: https://doi.org/10.1109/ELNANO.2015.7146909

[8] O. Karnaukh, Y. Karplyuk, and N. Nikitiuk, "Evaluation of machine learning techniques for ecg t-wave alternans," in *2018 IEEE 38th International Conference on Electronics and Nanotechnology (ELNANO)*, 2018, pp. 346–350. [Online]. Available: https://doi.org/10.1109/ELNANO.2018.8477528

[9] G. M. Nijm, S. Swiryn, A. C. Larson, and A. V. Sahakian, "Estimation of t-wave alternans from multi-lead ecg signals using a modified moving average method," in *2008 Computers in Cardiology*, 2008, pp. 517–520. [Online]. Available: https://doi.org/10.1109/CIC.2008.4749092

[10] S. Ayub, G. Gupta, and Y. Kumar, "Heart rate calculation and detection of t-wave alternans by correlation method," in *2016 8th International Conference on Computational Intelligence and Communication Networks (CICN)*, 2016, pp. 200–203. [Online]. Available: https://doi.org/10.1109/CICN.2016.45

[11] T. W. Shen and Y. T. Tsao, "An improved spectral method of detecting and quantifying t-wave alternans for scd risk evaluation," in *2008 Computers in Cardiology*, 2008, pp. 609–612. [Online]. Available: https://doi.org/10.1109/CIC.2008.4749115

[12] B. D. Nearing, A. H. Huang, and R. L. Verrier, "Dynamic tracking of cardiac vulnerability by complex demodulation of the t wave," *Science*, vol. 252, no. 5004, pp. 437–440, 1991. [Online]. Available: http://doi.org/10.1126/science.2017682

[13] B. Ghoraani, S. Krishnan, R. J. Selvaraj, and V. S. Chauhan, "T wave alternans evaluation using adaptive time–frequency signal analysis and non-negative matrix factorization," *Medical Engineering & Physics*, vol. 33, no. 6, pp. 700–711, 2011. [Online]. Available: https://doi.org/10.1016/j.medengphy.2011.01.007

[14] A. Khaustov, S. Nemati, and G. D. Clifford, "Twanalyser - a t-wave alternans detector," *Computers in Cardiology*, 2008. [Online]. Available: https://bit.ly/36nUz5L

[15] G. B. Moody, "The physionet/computers in cardiology challenge 2008: T-wave alternans," in *2008 Computers in Cardiology*, 2008, pp. 505–508. [Online]. Available: https://doi.org/10.1109/CIC.2008.4749089

CONTROL FOR THE OUTPUT VOLTAGE ON A FLYING CAPACITOR MULTILEVEL INVERTER

CONTROL PARA EL VOLTAJE DE SALIDA DE UN INVERSOR MULTINIVEL DE CAPACITORES FLOTANTES

Beatriz Angélica Aguilar-López[1], José Antonio Juárez-Abad[2,*],

Jorge Luis Barahona-Avalos[2], Rosalino Mayoral-Lagunes[1],

Jesús Linares-Flores[2], Marco Antonio Contreras-Ordaz[2]

Abstract

This paper presents the design of a robust Active Disturbance Rejection Controller (ADRC) for tracking the reference trajectory of the output voltage of a flying capacitor multilevel inverter. If the dynamics of each flying capacitor and of the passive elements of the filter are considered in the dynamic model of the converter, it results a high order model, which is difficult to control. PS-PWM modulation is used in this work to keep the voltages in the flying capacitors at their nominal values, and thereby generate a second-order simple dynamic model that is easier to control. The simulation and experimental results confirm that the controller is robust in the presence of disturbances, caused by either linear or nonlinear load changes. The experimental prototype of the complete system was built, and the implementation of the controller and the modulator was carried out in a FPGA; the results obtained are shown in the final part.

Resumen

Este artículo presenta el diseño de un controlador mediante la técnica de rechazo activo de perturbaciones para el seguimiento de la trayectoria de referencia para el voltaje de salida de un inversor multinivel de capacitores flotantes. Si en el modelo dinámico del convertidor se consideran las dinámicas de cada capacitor flotante, adicionalmente, las de los elementos pasivos del filtro de salida, el modelo resultante es de un orden alto, lo que dificulta su control. En este trabajo se emplea la modulación PS-PWM para mantener los voltajes en los capacitores flotantes en sus valores nominales y de esta manera poder generar un modelo dinámico simple, que resulta ser más fácil de controlar. Los resultados de simulación y experimentales, confirman que el controlador es robusto a perturbaciones provocadas por cambios en la carga, sin importar si son de tipo lineal o no lineal. Se realizó la construcción del prototipo experimental del sistema y se implementó el controlador y modulador en un FPGA y en la parte final se muestran los resultados obtenidos.

[1,*]División de estudios de posgrado, Universidad Tecnológica de la Mixteca - México.
  http://orcid.org/0000-0002-2769-4992, http://orcid.org/0000-0003-3420-7416
[2]Instituto de Electrónica y Mecatrónica, Universidad Tecnológica de la Mixteca - México.
  Corresponding author ✉: abad@mixteco.utm.mx
  http://orcid.org/0000-0001-7440-0849, http://orcid.org/0000-0002-5502-6692
  http://orcid.org/0000-0002-5723-4786, http://orcid.org/0000-0002-3478-796X

1. Introduction

Electric power may be available in two modes: direct current (DC) or alternating current (AC). There are applications where it is required the transformation from one mode to the other, and such conversion is carried out by a device known as power converter; for example, the AC-DC transformation is performed by a converter called rectifier, and the DC-AC conversion is carried out by a converter called inverter [1]. The power converters are built with commutation devices and passive elements such as capacitors, inductors, diodes and transformers. In general, the power that the converter is capable of delivering is limited by the current and voltage ratings of its switches and commutation devices.

Even though an inverter should ideally produce a sinusoidal voltage in traditional applications of alternating current (to achieve better efficiency and low electromagnetic interference, among other advantages [2]), they are only capable of producing rectangular waves (i.e., with three levels). With the rise of multilevel inverter topologies, it was possible to generate voltage waves with multiple levels, which are more similar to the ideal sinusoidal wave. The most well-known topologies of multilevel converters are: cascade cells, diode clamped and flying capacitor [3]. The first topology mentioned consists of a series connection of H-bridges and requires isolated voltage sources for each of the cells, while the last two require only one voltage source [4].

The topology of flying capacitor multilevel converters (FCMC) has demonstrated to be an excellent choice in applications where high power density is required [5]. The structure of a FCMC consists of power cells. Each power cell is constituted by a pair of switches and a flying capacitor. The number of levels at the output of the FCMC may be increased by adding more cells to the FCMC, but more capacitors and switches are required. Each flying capacitor should be charged to a particular nominal voltage. Depending on the state of the cell switches, the flying capacitor will or will not supply its voltage at the output of the converter.

For the correct operation of the FCMC, a balanced distribution in the voltages of the flying capacitors should be maintained: each of them should maintain a nominal voltage equivalent to a fraction of the total voltage of the DC bus divided between the number of cells. Two independent processes known as precharge and balancing (or regulation) of the voltages in the flying capacitors, are carried out to achieve a correct operation of the FCMC.

For the case of the precharge, some reported methods may be found in [6] and [7]. On the other hand, the balancing of the voltages in the flying capacitors may be carried out passively and actively. The natural or passive balancing utilizes a modulation technique commonly called Phase Shifted-PWM (PS-PWM). This modulation technique is employed to generate the commutation states that form the desired output voltage signal and, at the same time, it maintains an average net charge equal to zero in the flying capacitors.

The aforementioned passive balancing technique is easy to implement, but it does not guarantee that the voltages of the capacitors reach their nominal values, because the components utilized in the construction of the FCMC regularly have non-ideal conditions, i.e.: unequal leakage currents in the capacitors, asymmetrical charge and discharge in the capacitors and load disturbances, among others [8]. On the other hand, in active balancing the voltage of the flying capacitors is individually regulated. This approach requires the use of a voltage sensor for each of the flying capacitors as shown in [9] and [10], or estimating them by means of observers as it is considered in [11].

A necessary control task in power converters is supplying an output voltage of constant amplitude, regardless of the effective load resistance. For the case of the DC-AC converter it is desired that the output tracks a reference voltage despite the disturbances that occur due to changes in the load current or in the input voltage [12]. A feedback control system is required for these tasks to be carried out precisely. Voltage tracking in multilevel inverters has been addressed using different control techniques. Different control schemes have been employed for the cascade cells topology, which include: passivity-based controller [13] and generalized proportional integral tracking control [14]. Voltage tracking for the flying capacitor topology has been carried out in [15] and [16]. In [15], each appropriate commutation state is generated to produce the desired output voltage, using an algorithm that does not require an additional modulation nor the model of the converter. In [16], the authors state that the tasks of voltage balancing and voltage reference tracking are coupled, which becomes a serious problem in high bandwidth and high precision applications. They emphasize in the decoupling of these tasks by means of two techniques: feedback linearization and a variant of vector space modulation. Proportional-integral (PI) and linear quadratic regulator (LQR) controllers are applied for voltage tracking, and simple proportional (P) controllers for balancing the voltages in the capacitors.

The objective of the present work is the tracking control of a sinusoidal reference signal applied to the output voltage of a FCMC. The PS-PWM modulation is responsible for the task of balancing the voltages in the flying capacitors. This enables avoiding the use of multiple voltage sensors, and reducing the complexity of both the converter dynamic model and of the controller implementation. The controller is based on the Active Disturbance Rejection Control (ADRC) technique.

Section 2.1 describes the components of the system: controller, modulator and power converter. The average dynamic model of the FCMC is obtained in section 2.2. The exact linearization of the FCMC model is carried out in section 2.3. The design of the ADRC-based controller is presented in section 2.4. Section 3 shows the results of the cosimulation carried out in Matlab-Simulink/PSIM, where it is analyzed the effectiveness of the controller before the experimental construction, the experimental results are shown in section 4 and, at last, the conclusions are presented in section 5.

2. Materials and methods
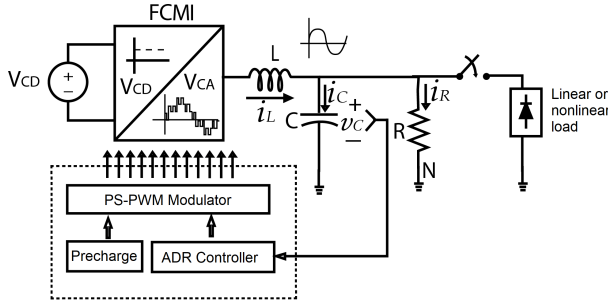
Figure 1. Block diagram of the system.

Figure 1 shows the complete system which is described in the following. From a direct current voltage source, V_{CD}, the FCMC synthetizes at the output a signal with multiple voltage levels based on PWM. Such output voltage is processed by a low pass LC passive filter, with the purpose of attenuating the high frequency components of the PWM signal and, at last, obtaining a voltage signal purely sinusoidal at the output of the filter. The active disturbance rejection controller feedbacks the voltage signal of the filter and compares it against a sinusoidal reference signal, of frequency 60 Hz and variable amplitude; the reference or modulating signal is employed for the PS-PWM modulator. During the firing of the FCMC the flying capacitors are discharged, and therefore, the correct voltage, or nominal voltage, in each of them is established by means of the precharge process.

Initially, a resistive load with known value is connected in parallel with the capacitor C of the output filter, and at a given time a linear or nonlinear load is added to the system as an external disturbance.

The FCMC is shown in Figure 2, which consists of multiple power cells connected one after another. Each power cell (except the one connected to the DC bus) contains a pair of power switches and a flying capacitor.
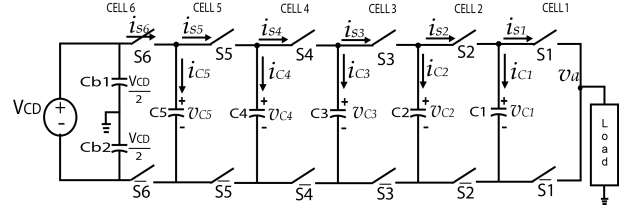
Figure 2. Topology of the flying capacitor multilevel inverter (FCMI).

For example, cell 1 is constituted by switches $S1$, $\bar{S}1$ and by capacitor $C1$. Six cells are required to obtain seven voltage levels, including the level corresponding to $0V$. Each flying capacitor of the ith cell, should be charged and should be maintained at a nominal voltage V_{Ci}, which may correspond to any of the following values: $V_{CD}/6$, $2V_{CD}/6$, $3V_{CD}/6$, $4V_{CD}/6$, $5V_{CD}/6$.

Individually, each switch of the converter may be closed (ON) or open (OFF). For the purpose of avoiding short circuits in the cells, the switches of each cell should operate in a complementary manner, and consequently never should remain closed at the same time; this condition is guaranteed using a delay time between commutations. In the flying capacitors topology, as well as in other multilevel topologies, a particular level of voltage may be obtained with different commutation states, which are called redundant states. In the topology of half-bridge FCMC of seven levels, the following voltage levels may be obtained at the output: $-3V_{CD}/6$, $-2V_{CD}/6$, $-V_{CD}/6$, 0, $V_{CD}/6$, $2V_{CD}/6$, $3V_{CD}/6$.

2.1. Average dynamic model

Applying Kirchhoff's current law to the FCMC shown in Figure 2, the following set of equations for the currents in the flying capacitors is obtained:

$$
\begin{aligned}
C_1 \frac{dv_{C1}}{dt} &= i_L(d_2 - d_1) \\
C_2 \frac{dv_{C2}}{dt} &= i_L(d_3 - d_2) \\
C_3 \frac{dv_{C3}}{dt} &= i_L(d_4 - d_3) \\
C_4 \frac{dv_{C4}}{dt} &= i_L(d_5 - d_4) \\
C_5 \frac{dv_{C5}}{dt} &= i_L(d_6 - d_5)
\end{aligned}
\tag{1}
$$

where i_L is the current through the inductor of the output filter, C_i is the capacitance of the capacitors of the FCMC, d_i represents the duty cycle of the S_i switch and v_{Ci} are the voltages in the flying capacitors, with $i = \{1, 2, 3, 4, 5\}$.

The output voltage of the FCMC of Figure 2 is measured from node va with respect to ground and is called v_{aN},, which is determined in the following manner:

$$v_{aN} = v_{C1}(d_1 - d_2) + v_{C2}(d_2 - d_3) + v_{C3}(d_3 - d_4)+$$
$$v_{C4}(d_4 - d_5) + v_{C5}(d_5 - d_6) + V_{CD}d_6 - \frac{V_{CD}}{2} \qquad (2)$$

The PS-PWM modulation generates the PWM signals for each pair of switches of the cells of the FCMC. Figure 3(a) shows some cycles of the carrier signals $C1$ to $C6$, which are triangular signals with amplitudes that take values in the interval $[-1, 1]$ and frequency f_c, 60 degrees out of phase. The frequency of the carriers is greater than the frequency f_m of the modulating signal, and consequently it is common to define a modulating index $\frac{f_c}{f_m} \geq i_m$. In this work, a modulating index $i_m = 40$ was employed. For the case of the modulating signal u_{av}, its amplitude takes values in the interval $[-1, 1]$ and has a frequency $f_m = 60\ Hz$.

Each carrier signal is compared with the modulating signal to obtain the PWM signals, as can be seen in Figure 3(b), producing the PWM signals named as $V_a - V_f$, which have the same duty cycle d.

Applying this signal to the FCMC of seven levels, all switches have the same duty cycle, i.e.:

$$d_1 = d_2 = d_3 = d_4 = d_5 = d_6 = d \qquad (3)$$

According to equation (1), the variation of the average voltage in each flying capacitor is zero when all duty cycles, d_1 to d_6, are equal. Therefore, the dynamics of the voltages (1) in the flying capacitors can be considered as constant, and their derivatives equal to zero. This is the reason why the dynamics of the capacitors may not be considered in the average model of the FCMC.

On the other hand, there is a relationship between the duty cycle d and the modulating signal u_{av}, which is expressed as $d = \frac{u_{av}}{2} + 0.5$. Considering this and substituting (3) in (2), the output voltage V_{aN} can be expressed as follows:

$$v_{aN} = V_{CD}(d) - \frac{V_{CD}}{2} = \frac{V_{CD}}{2}u_{av} = Eu_{av} \qquad (4)$$

where E is the voltage of each of the capacitors $Cb1$ and $Cb2$, whose value is $V_{DC}/2$. Equation (4) enables seeing the FCMC of seven levels in a simplified manner, as a multilevel converter «reducer» with a supply voltage source Eu_{av} (where $E = V_{CD}/2$), a low pass LC filter and a varying load, as shown in Figure 4.

(a)

(b)
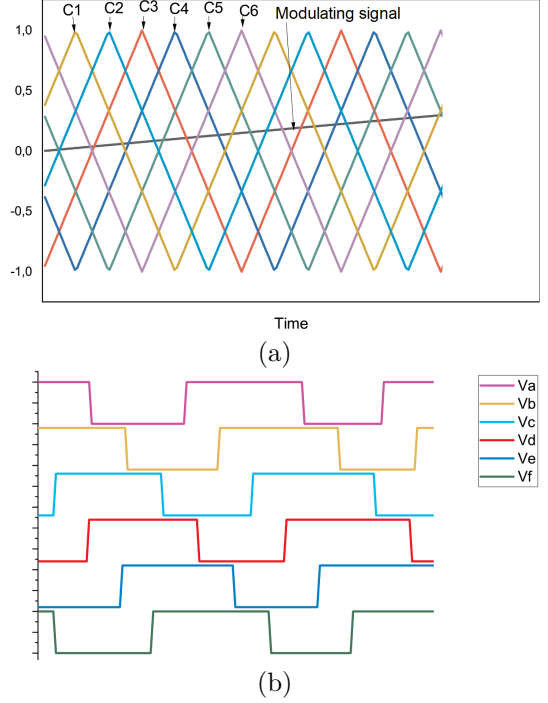
Figure 3. PS-PWM modulation: (a) Carriers of the modulation; (b) Duty cycle in the generated PWM channels.
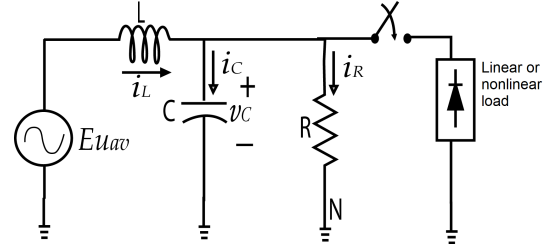
Figure 4. Simplified model of the flying capacitor multilevel inverter.

Considering the above, the second order average model of the FCMC can be expressed as in (5):

$$L\frac{di_L}{dt} = -v_C + Eu_{av}$$
$$C\frac{dv_C}{dt} = i_L - \frac{v_C}{R} \qquad (5)$$

The control input u_{av} represents the PWM modulating signal, which can take values in the continuous interval $[-1, 1]$. The term v_C is the voltage in the filter capacitor. The current that circulates through the switches and through the output inductance is i_L, L and C are the values of the inductance and capacitance of the filter, respectively.

2.2. Exact linearization of the model

The FCMC system previously described is linear, Single Input-Single Output (SISO) and, as it was men-

tioned above, of reducing nature. Regrouping the model shown in equation (5) to be expressed in its nonlinear affine form, yields:

$$\dot{x} = f(x) + g(x)u$$
$$y = h(x) \tag{6}$$

where:

$$f(x) = \begin{pmatrix} -\frac{v_C}{L} \\ \frac{i_L}{C} - \frac{v_C}{RC} \end{pmatrix}, \quad g(x) = \begin{pmatrix} \frac{E}{L} \\ 0 \end{pmatrix}$$

and:

$$x = \begin{pmatrix} x_1 \\ x_2 \end{pmatrix} = \begin{pmatrix} i_L \\ v_C \end{pmatrix}$$

As it is widely described in [17], the output function that enables exact linearization of the nonlinear system (6) is given as:

$$h(x) = v_C \tag{7}$$

The relative degree r of the nonlinear system (6) is obtained by means of the successive calculation of the Lie derivatives:

$$L_g L_f^k h(x) = 0 \tag{8}$$

until finding the Lie derivative that satisfies:

$$L_g L_f^{r-1} h(x) \neq 0 \tag{9}$$

where $k < r-1, \forall x \in \Omega$. The calculated Lie derivatives are:

$$L_g L_f^0 h(x) = L_g h(x) = \frac{\partial h(x)}{\partial x} g(x)$$
$$= \begin{pmatrix} 0 & 1 \end{pmatrix} \begin{pmatrix} \frac{E}{L} \\ 0 \end{pmatrix} = 0 \tag{10}$$

$$L_g L_f^1 h(x) = \frac{\partial [L_f h(x)]}{\partial x} g(x) = \begin{pmatrix} \frac{1}{C} & -\frac{1}{RC} \end{pmatrix} \begin{pmatrix} \frac{E}{L} \\ 0 \end{pmatrix} = \frac{E}{LC} \tag{11}$$

Since (11) is different than 0, the relative degree r of system (6) is equal to 2. The transformation of coordinates **x** to **z** is carried out by means of:

$$\mathbf{z} = \mathbf{\Phi}(\mathbf{x}) = \begin{pmatrix} z_1 \\ z_2 \end{pmatrix} = \begin{pmatrix} L_f^0 h(x) \\ L_f^{n-1} h(x) \end{pmatrix} \tag{12}$$

In order to verify if **Φ** is a diffeomorphism, it is verified the nonsingularity of the Jacobian matrix, given by

$$\mathbf{J_\Phi} = \frac{\partial \mathbf{\Phi}(\mathbf{x})}{\partial \mathbf{x}} = \begin{pmatrix} \frac{\partial z_1}{\partial x_1} & \frac{\partial z_1}{\partial x_2} \\ \frac{\partial z_2}{\partial x_1} & \frac{\partial z_2}{\partial x_2} \end{pmatrix} = \begin{pmatrix} 0 & 1 \\ \frac{1}{C} & -\frac{1}{RC} \end{pmatrix} \tag{13}$$

It can be shown from (13) that $\mathbf{J_\Phi}$ is nonsingular for any **x**, and consequently the coordinate transformation is valid. The coordinate system **z** is expressed as:

$$z_1 = v_C$$
$$z_2 = \frac{1}{C} i_L - \frac{1}{RC} v_C \tag{14}$$

The original system (6) is transformed into the linearized system in the Brunovsky normal form, as shown in the following:

$$\dot{z}_1 = z_2$$
$$\dot{z}_2 = \alpha(x) + \beta(x)u = v \tag{15}$$

where:

$$\alpha(x) = (\frac{1}{C^2 R^2} - \frac{1}{LC}) v_C - \frac{1}{C^2 R} i_L \tag{16}$$

$$\beta(x) = L_g L_f^1 h(x) = \frac{E}{LC} \tag{17}$$

Variable v is an auxiliary control law whose expression will be stated later and will define the desired tracking dynamics of the system. The control law is obtained solving (15) for u, as follows:

$$u = \frac{v - \alpha(x)}{\beta(x)} \tag{18}$$

The model of the FCMC shown in (5) considers a resistive load R of known value, but since the inverter is subject to loads of varying nature, the load current i_L will change its value depending of the load, thus causing disturbances in the output voltage of the inverter. As can be seen, the control law of Equation (18) requires the value of $\alpha(x)$, which in turn requires the measurement of i_L. A way to avoid using the current sensor is proposed in the following.

2.3. Design of the ADRC controller

Based on the ADRC approach with extended state observer, a Linear Extended State Observer (LESO) [18] is designed, making the following assumptions:

1. It is only measured the flat output $F = v_C$.

2. The nominal values of the parameters L, C, R, E are known.

3. The control input u_{av} is available.

4. The disturbance function $\alpha(x)$ is unknown, but it is considered as bounded.

5. The estimated variables of the flat output and its derivative are denoted as $F_1 = \widehat{F}$ and $F_2 = \widehat{\dot{F}}$.

6. The estimated variables of the disturbance function and its derivative are $\eta_1 = \widehat{\alpha(x)}$ and $\eta_2 = \widehat{\dot{\alpha}(x)}$.

The LESO observer is designed from (15) and is defined as follows:

$$
\begin{aligned}
\dot{F}_1 &= F_2 + \lambda_3(F - F_1) \\
\dot{F}_2 &= \eta_1 + \beta(x)u + \lambda_2(F - F_1) \\
\dot{\eta}_1 &= \eta_2 + \lambda_1(F - F_1) \\
\dot{\eta}_2 &= \lambda_0(F - F_1)
\end{aligned}
\tag{19}
$$

The set of coefficients $\lambda_0, \lambda_1, \lambda_2, \lambda_3$ are constant values, and are chosen by means of a fourth order Hurwitz polynomial:

$$
\begin{aligned}
\lambda_0 &= \omega_n^4 \\
\lambda_1 &= 4\zeta\omega_n^3 \\
\lambda_2 &= 2\omega_n^2 + 4\zeta^2\omega_n^2 \\
\lambda_3 &= 4\zeta\omega_n
\end{aligned}
\tag{20}
$$

The ADRC control is designed from (18) and (19), where the estimated values of the LESO observer are adapted to the auxiliary tracking controller:

$$
v = \dot{F}_2^* - k_1(F_2^* - z_2) - k_0(F_1^* - z_1)
\tag{21}
$$

where the tracking signals are:

$$
\begin{aligned}
F_1^* &= A\sin(\omega_n t) \\
F_2^* &= -A * \omega_n \cos(\omega_n t) \\
\dot{F}_2^* &= A(\omega_n)^2 \sin(\omega_n t)
\end{aligned}
\tag{22}
$$

with $\omega_n = 2\pi f$ and $f = 60$ Hz.
The control law based on the ADRC technique is stated as follows:

$$
u = \frac{v - \eta_1}{\beta(x)}
\tag{23}
$$

In (22), η_1 represents the estimated value of $\alpha(x)$, i.e., $\eta_1 = \widehat{\dot{\alpha}(x)}$. The coefficients k_0, k_1 are constant values, chosen by means of a second order Hurwitz polynomial, as shown in the following:

$$
\begin{aligned}
k_0 &= w_{nc}^2 \\
k_1 &= 2\zeta_c w_{nc}
\end{aligned}
\tag{24}
$$

3. Simulation of the system

The simulation of the system was performed using the SimCoupler module and was carried out through a cosimulation between PSIM 9.0 and MATLAB/Simulink. The controller is constructed in MATLAB/Simulink, as shown in Figure 5. On the other hand, the precharge circuit and the elements of the multilevel inverter (output filter, PS-PWM modulator and the control for load changes) are constructed in PSIM, as shown in Figure 6. Therefore, the controller processing is carried out in MATLAB/Simulink and is coupled to PSIM through the SimCoupler module; the value of the coupled control signal is called u_{av}, which is received by the PS-PWM modulator as duty cycle to perform the control action on the FCMC output.

(a)

complex plane, in order to guarantee the stability.

(b)
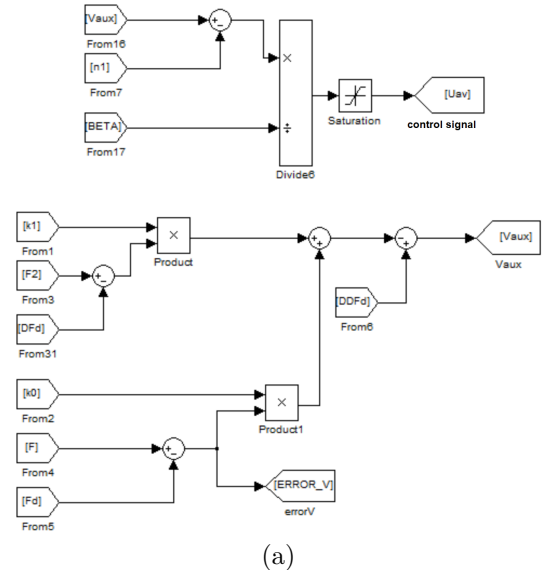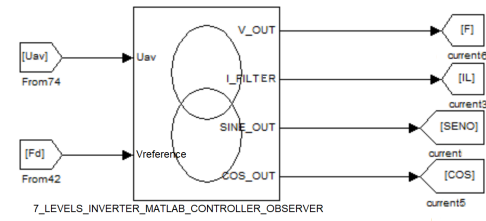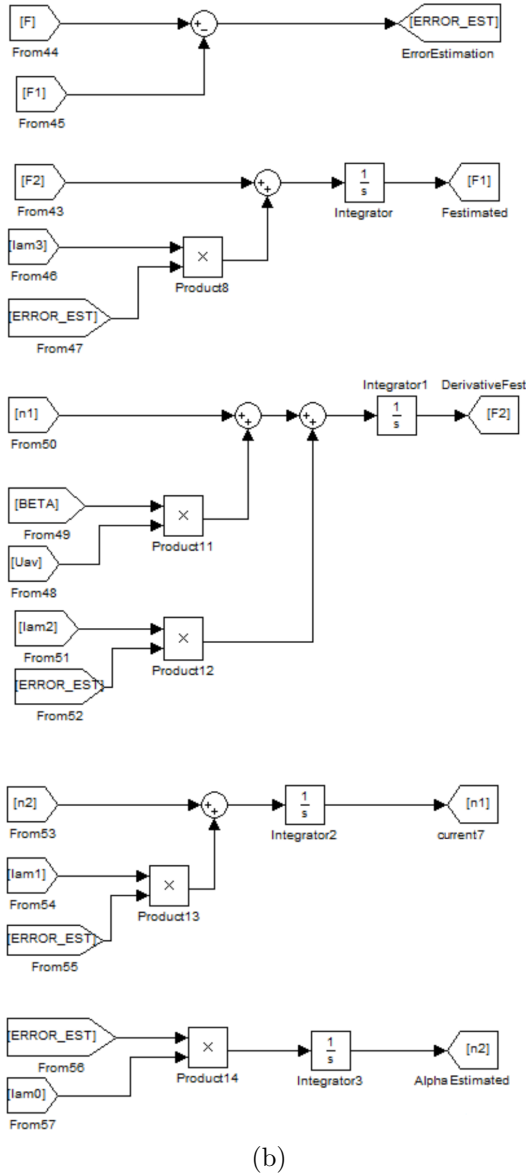
Figure 5. MATLAB/Simulink: (a) ADRC control and (b) LESO Observer.

(a)

(b)

(c)
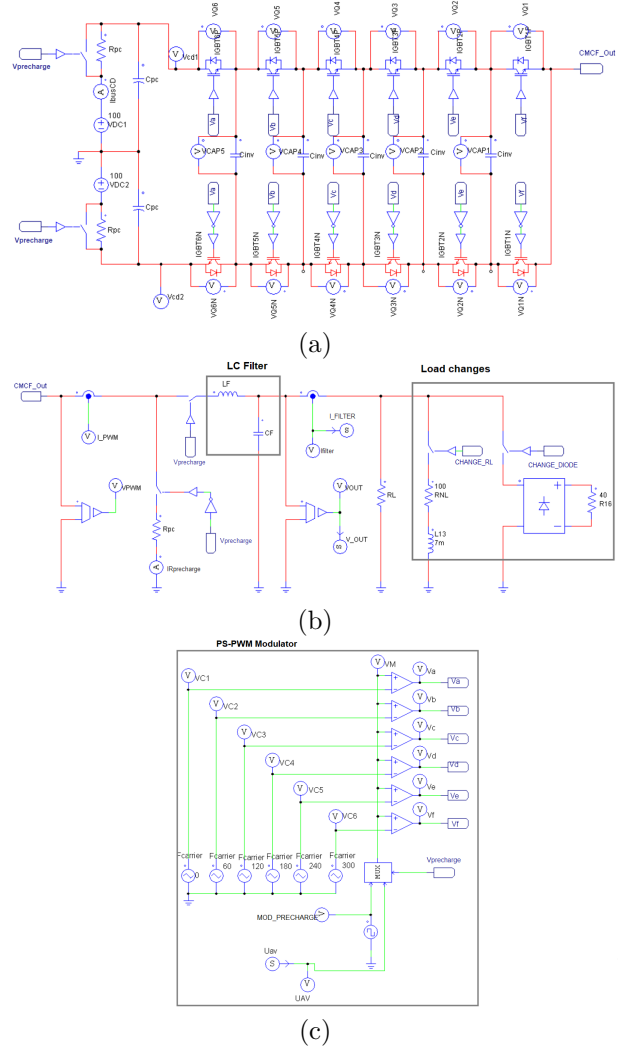
Figure 6. (a) Multilevel inverter, (b) LC filter at the output and load change control, (c) PS-PWM modulator and load changes activation.

For all passive components employed, plate nominal values were considered with a tolerance of 20 % for capacitors and of 10 % for resistors and inductors; therefore, for the multilevel converter the following values were used: $C_{CAP1...CAP5} = 10 \ \mu F$; the DC bus capacitors have a value of $C_{PC} = 1000 \ \mu F$. The values of the elements of the output filter are $C_F = 4.7 \ \mu F$, $L_F = 7 \ mH$ and $R_L = 100 \ \Omega$. The voltage reference signal is equal to $Vd = A \sin(2\pi f)$, the tests were conducted for a desired amplitude $A = 80 \ V$ and a frequency $f = 60 \ Hz$. On the other hand, the PS-PWM modulation utilizes carriers with frequency 2.4 kHz. The value of the parameters for the LESO observer λ_0, λ_1, λ_2, λ_3 are calculated with $w_n = 30000$ and $\zeta = 0.707$. The parameters of the controller k0 and k1 are calculated with $w_{nc} = 3000$ and $\zeta_c = 0.707$. In both cases the poles are located in the left side of the

In order to verify the robustness of the ADRC controller in the presence of sudden load changes, two types of tests were conducted: for a first test, an additional $R - L$ load, with nominal values $R_{NL1} = 80 \ \Omega$ and $L_{NL} = 7 \ mH$, is added at the output of the inverter, after the filter. The result of the simulation is shown in Figure 7(a), where it can be seen that when the load change occurs, the current i_L increases its value, and the LESO estimator together with the ADRC controller update the control signal u_{av}, enabling that the capacitor voltage retakes the reference trajectory again.

(a)

(b)
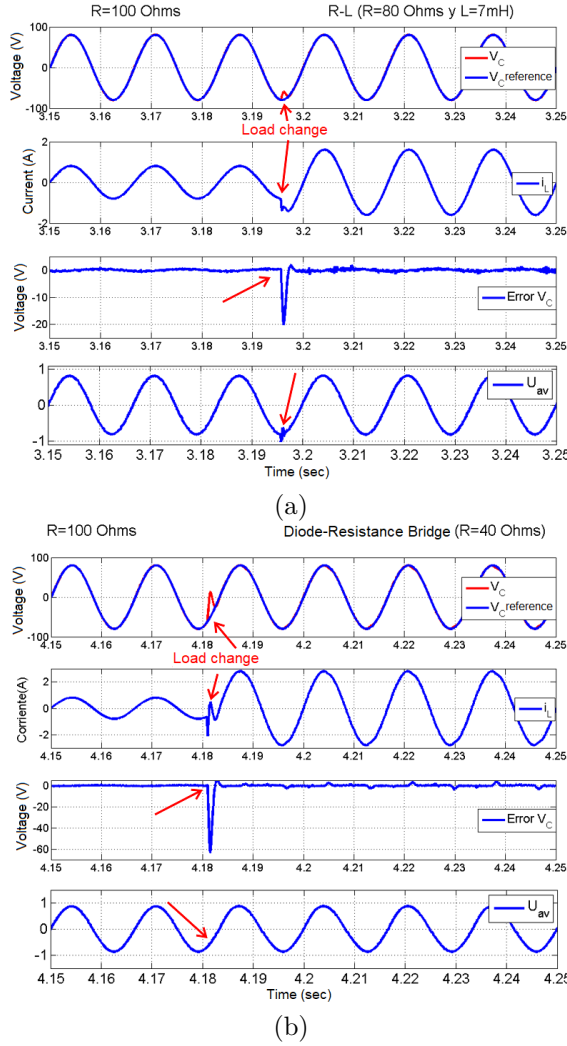
Figure 7. Simulation results: (a) With additional R − L load, (b) With additional load constituted by a bridge of diodes and a resistance.

The second test consisted in adding a nonlinear load constituted by a bridge of diodes together with a resistive load of 40 Ω. Figure 7(b) shows the result of the simulation, where it can be seen that adding the nonlinear load produces a significant transient deviation of the capacitor voltage from its sinusoidal reference, which is similarly corrected by the action of the LESO estimator and the ADRC controller.

Figure 8 shows the result of the simulation with the controller, of the behavior of the voltage in the flying capacitors during the load changes implemented in the previous tests. The precharge of the flying capacitors is carried out according to the work presented in [7], where a time interval of $t = [0 − 2]$s is proposed. In the presence of load changes, it is seen that the average voltages of the flying capacitors are maintained at their nominal values; the ripple increases, and is larger when the nonlinear load of diode + resistance is connected. To validate the effect of the controller on the output voltage v_C, two simulation tests were

conducted, the first test without controller, only with the PS-PWM modulator; the result of this test can be seen in Figure 9(a). In the second test the proposed controller is utilized, and the result is shown in Figure 9(b). In this test the voltage v_C of the capacitor remains without changes or changes hardly perceptible close to the reference. At this point, and analyzing the aforementioned figures, it can be argued that the PS-PWM modulation for itself would not be capable of maintaining the output voltage.
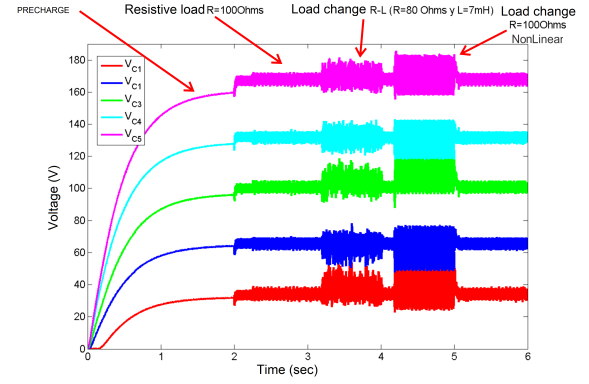
Figure 8. Simulation result of the voltages in the flying capacitors during the precharge, normal operation and load changes.

(a)

(b)
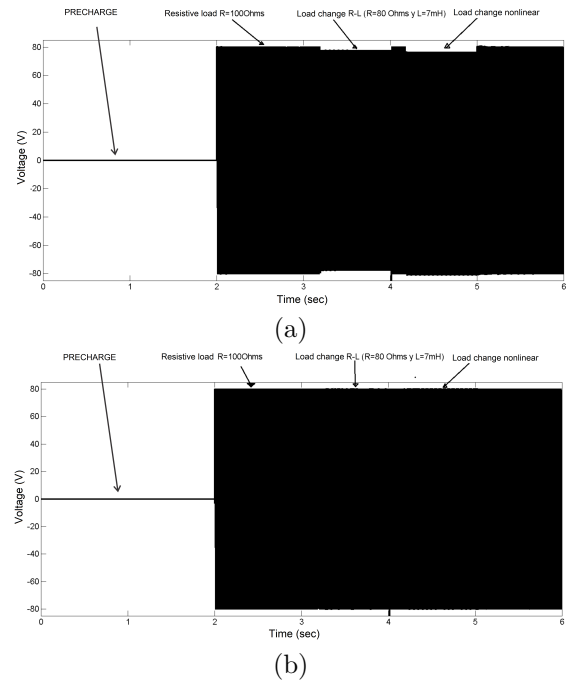
Figure 9. Simulation results for the output voltage v_C: (a) With load changes and only the PS-PWM modulator, (b) With load changes and applying the controller + LESO estimator.

4. Experimental results

In order to verify the simulation results, the implementation of the system was carried out which consisted of two main parts: the first comprises the construction of the multilevel converter prototype and of the auxiliary systems for its operation; the description of this system is shown in Figure 10.

The second part is the implementation in a FPGA of the algorithms of the ADRC controller and the PS-PWM modulator. In [19] it is recommended to follow the top-down methodology, which is very appropriate to implement algorithms in reconfigurable logic devices, and has been used with excellent performance in [14] [20–22]. In order to carry out the implementation the software Xilinx ISE 14.7 was utilized, and the coding was made in VHDL without using any high level tool based on blocks or code generation, and the internal elements of the FPGA were utilized, such as

BRAM memories and embedded multipliers, to optimize the use of the device internal resources; the design which was made is shown in Figure 11. It is worth mentioning that the 32-bit simple floating point numerical representation, according to the IEEE-754 standard, was utilized for the necessary arithmetic operations, and a sampling time of 10 μs was achieved.

For evaluating the performance of the controller, two types of tests were carried out just like in simulation: open-loop and closed-loop. Linear and nonlinear load changes were made in both cases, to verify the performance of the proposed controller.

The prototype was initially tested to verify its correct operation, and the result of this test is shown in Figure 12. The output with seven levels taken before the output filter can be seen in Figure 12(a); Figures 12(b) and (c) show the sinusoidal output after the LC filter for the supplied voltage and current, respectively.
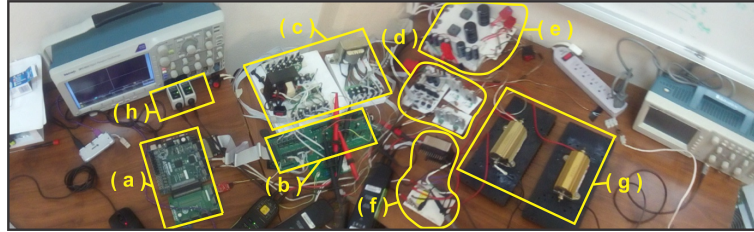
Figure 10. Developed prototype of the seven levels flying capacitor multilevel inverter: (a) Development board based on FPGA (Nexys-2), (b) Multilevel inverter, (c) Isolated sources for gate drivers and instrumentation, (d) Control of the precharge of capacitors and of the load change at the output, (e) Main DC source, (f) LC filter at the inverter output, (g) Loads at the inverter output (200 W), (h) Isolated measurement probes.

(a)

(b)
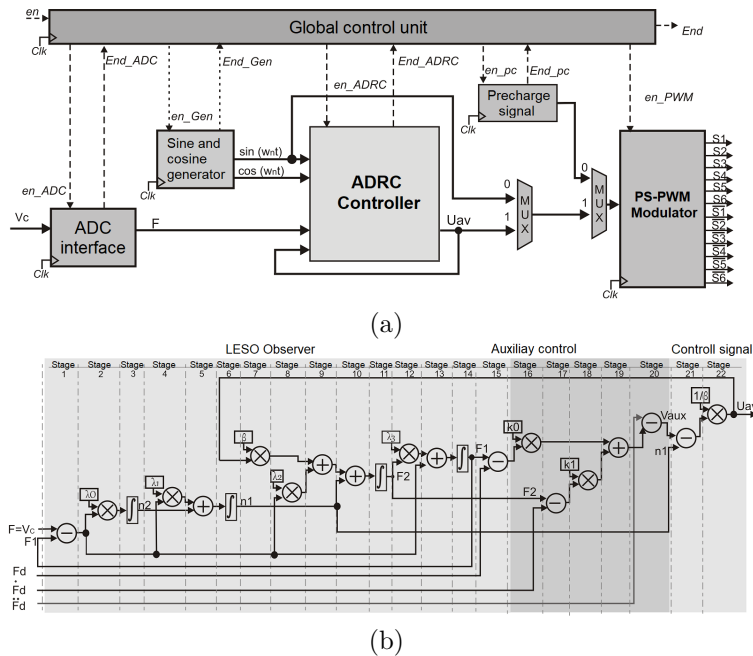
Figure 11. Implementation in the FPGA device: (a) Proposed block diagram, (b) Designed architecture for the execution of the control algorithm and LESO.
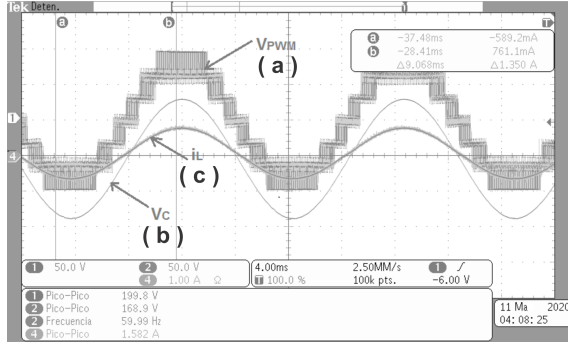
Figure 12. Shapes of the output waves obtained from the experimental prototype: (a) Multilevel output voltage of 7 levels before the LC filter (V_{PWM}), (b) Output voltage after the LC filter (V_C), (c) Current supplied to the load (i_L).

A test with a power quality meter (Hioki 3197) was carried out to validate the harmonic content of the inverter output wave; the result is shown in Figure 13, where it is observed a high quality of the output wave, both in voltage (THD_v) and current (THD_i).
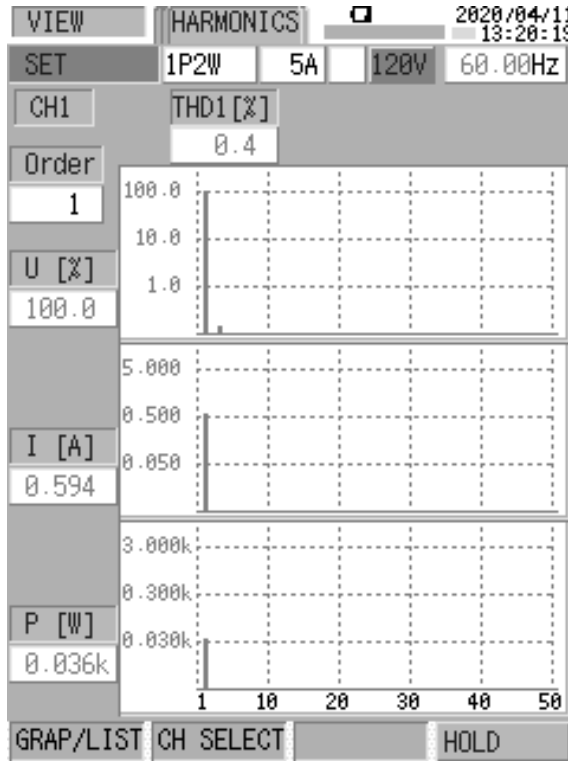
Figure 13. Result of the THD_v and THD_i measurement at the output of the multilevel inverter.

As a result of the open-loop test, Figure 14 shows the results of three aspects that are considered important: the control signal (uav), the converter output voltage (v_C) and the voltage of the capacitors ($V_{C1...C5}$). As it was previously mentioned, linear and nonlinear load changes were carried out. Figure 14(a)

shows the value of the control signal with a fixed amplitude after the precharge with a value $u_{av} = 0.85$, which is equivalent to a reference value of the output voltage $V_C = 85$ V, as can be seen in Figure 14(b) when the system is subject to sudden load changes. It can be clearly observed in this figure that during transients, the voltage amplitude is affected, since it decreases. It is observed in Figure 14(c) that the balance of the capacitors is nominally maintained inside their working zone, but an increase in the ripple of each of them can be seen when load changes occur.
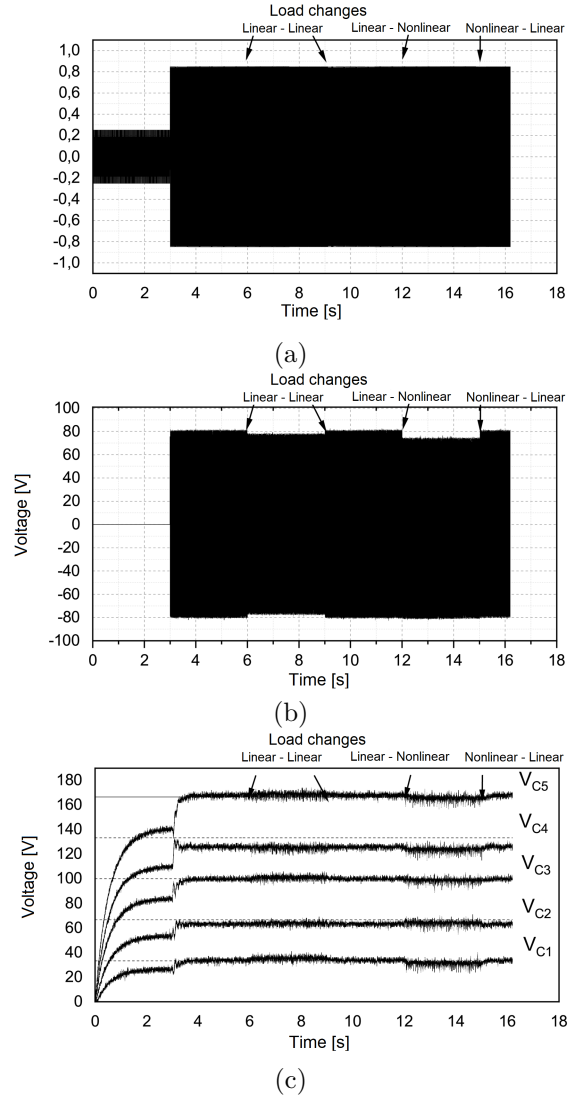
Figure 14. Plots of the experimental results obtained in open-loop in the presence of different load changes: (a) Control signal (u_{av}), (b) Inverter output voltage after the filter (V_C), (c) Voltage in the flying capacitors $V_{C1...C5}$.

The closed-loop test was carried out under the same procedure used for the open-loop test. Figure 15(a) shows the result of the control signal; after the precharge period, an initial value $u_{av} = 0.85$ is established for a reference value of $V_C = 85$ V, and in

the same figure it can be seen the action of the controller (variable u_{av}) during the sudden connection of loads. Figure 15(b) shows that the amplitude of the output voltage does not vary when the load changes are performed. Figure 15(c) shows the voltage of the capacitors, which maintain the balance and only a high frequency increase is observed in each of them.

(a)

(b)

(c)
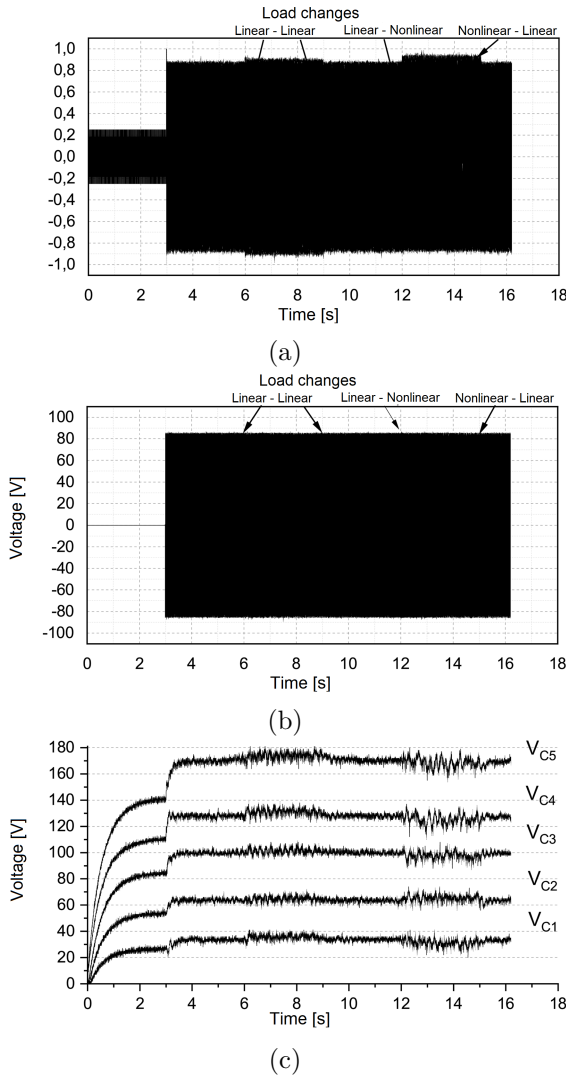
Figure 15. Plots of the experimental results obtained in closed-loop with the ADR_C controller, in the presence of different load changes: (a) Control signal (u_{av}), (b) Inverter output voltage after the filter (V_C), (c) Voltage in the flying capacitors $V_{C1...C5}$.

5. Conclusiones

In general, it is observed that reducing the complexity of the FCMC model considerably helped in other aspects such as the reduction in the computation capability necessary to process the controller, reduction of the processing time and requiring less sensors in the prototype.

On the other hand, it can be stated that it is necessary that the PS-PWM modulation maintains the balance of the 12 voltages of the flying capacitors for the ADRC control to work appropriately, i.e., so that it performs the tracking of the reference voltage, but the PS-PWM modulation is not capable of maintaining the desired output voltage at its nominal value in the presence of disturbances in the load current.

By adding the ADRC controller, the control task is carried out in an effective manner. The ADRC controller and the LESO observer effectively manage the current disturbance, and consequently the controller may be considered as robust in the presence of external disturbances produced by linear and nonlinear load changes. The voltage signal in the filter capacitor effectively tracks the imposed reference, except for transient deviations that are quickly minimized by the controller. It should be considered that in the case of unbalance of the capacitors, the ADRC control is not capable of tracking the reference voltage.

The use of the programmable logic device for implementing the system, as can be observed in experimental tests, contributed to obtaining very good results, especially in terms of speed of execution of the algorithm and attention to disturbances. It was verified that the multilevel inverters have among their main features a high quality in the output wave ($THD_v < 5$ %, as required by the IEEE-519 standard), and that the flying capacitor topology is a recommended choice among the other existing multilevel structures, since it requires only one DC source.

References

[1] D. Hart, *Electrónica de potencia.* Madrid: Pearson Education, 2001. [Online]. Available: https://bit.ly/3eJZYXH

[2] R. Haider, R. Alam, N. B. Yousuf, and K. M. Salim, "Design and construction of single phase pure sine wave inverter for photovoltaic application," in *2012 International Conference on Informatics, Electronics & Vision (ICIEV).* IEEE, may 2012. [Online]. Available: https://doi.org/10.1109/iciev.2012.6317332

[3] L. Franquelo, J. Rodríguez, J. Leon, S. Kouro, R. Portillo, and M. Prats, "The age of multilevel converters arrives," *IEEE Industrial Electronics Magazine*, vol. 2, no. 2, pp. 28–39, jun 2008. [Online]. Available: https://doi.org/10.1109/mie.2008.923519

[4] S. A. Gonzalez, S. A. Verne, and M. I. Valla, *Multilevel Converters For Industrial Applications.* Taylor & Francis Ltd, 2017. [Online]. Available: https://bit.ly/3eN3PUc

[5] Y. Lei, C. Barth, S. Qin, W.-c. Liu, I. Moon, A. Stillwell, D. Chou, T. Foulkes, Z. Ye, Z. Liao, and R. C. N. Pilawa-Podgurski, "A 2 kW, single-phase, 7-level, GaN inverter with an active energy buffer achieving 216 w/in^3 power density and 97.6% peak efficiency," in *2016 IEEE Applied Power Electronics Conference and Exposition (APEC)*. IEEE, mar 2016. [Online]. Available: http://doi.org/10.1109/apec.2016.7468068

[6] D. Janik, T. Kosan, P. Kamenicky, and Z. Peroutka, "Universal precharging method for dc-link and flying capacitors of four-level flying capacitor converter," in *IECON 2013 - 39th Annual Conference of the IEEE Industrial Electronics Society*. IEEE, nov 2013. [Online]. Available: https://doi.org/10.1109/IECON.2013.6700175

[7] S. Thielemans, B. Reznikov, J. Melkebeek, and A. Ruderman, "Self-precharge for single-leg odd-level multilevel converter," in *5th IET International Conference on Power Electronics, Machines and Drives (PEMD 2010)*. Institution of Engineering and Technology, 2010. [Online]. Available: https://doi.org/10.1049/cp.2010.0142

[8] C. Feng, J. Liang, and V. G. Agelidis, "Modified phase-shifted PWM control for flying capacitor multilevel converters," *IEEE Transactions on Power Electronics*, vol. 22, no. 1, pp. 178–185, jan 2007. [Online]. Available: https://doi.org/10.1109/tpel.2006.886600

[9] M. Trabelsi and L. Ben-Brahim, "Experimental photovoltaic power supply based on flying capacitors multilevel inverter," in *2011 International Conference on Clean Electrical Power (ICCEP)*. IEEE, jun 2011. [Online]. Available: http://doi.org/10.1109/iccep.2011.6036314

[10] A. M. Y. M. Ghias, J. Pou, M. Ciobotaru, and V. G. Agelidis, "Voltage balancing method for the multilevel flying capacitor converter using phase-shifted PWM," in *2012 IEEE International Conference on Power and Energy (PECon)*. IEEE, dec 2012. [Online]. Available: http://doi.org/10.1109/pecon.2012.6450221

[11] G. Gateau, M. Fadel, P. Maussion, R. Bensaid, and T. A. Meynard, "Multicell converters: active control and observation of flying-capacitor voltages," *IEEE Transactions on Industrial Electronics*, vol. 49, no. 5, pp. 998–1008, oct 2002. [Online]. Available: http://doi.org/10.1109/tie.2002.803200

[12] R. W. Erickson and D. Maksimović, *Fundamentals of Power Electronics*. Springer US, 2001. [Online]. Available: http://doi.org/10.1007/b100747

[13] H. Miranda, V. Cárdenas, G. Espinosa-Pérez, and D. Noriega-Pineda, "Multilevel cascade inverter with voltage and current output regulated using a passivity - based controller," in *Conference Record of the 2006 IEEE Industry Applications Conference Forty-First IAS Annual Meeting*. IEEE, oct 2006. [Online]. Available: https://doi.org/10.1109/IAS.2006.256643

[14] J. A. Juárez-Abad, J. Linares-Flores, E. Guzman-Ramírez, and H. Sira-Ramírez, "Generalized proportional integral tracking controller for a single-phase multilevel cascade inverter: An FPGA implementation," *IEEE Transactions on Industrial Informatics*, vol. 10, no. 1, pp. 256–266, feb 2014. [Online]. Available: http://doi.org/10.1109/tii.2013.2242085

[15] F. J. Chavero Ramírez, H. J. C. López Tapia, and N. V. Nava, "Estrategia de control para inversor multinivel con capacitores flotantes," *Pistas educativas*, vol. 108, no. 35, 2014. [Online]. Available: https://bit.ly/3eNaVIk

[16] M. Caris, H. Huisman, J. Duarte, and E. Lomonova, "Nonlinear and vector closed-loop control methods for flying-capacitor power converters," *International Journal of Electronics*, vol. 104, no. 8, pp. 1298–1316, mar 2017. [Online]. Available: https://doi.org/10.1080/00207217.2017.1293739

[17] D. Bhattacharyya, S. Padhee, and K. C. Pati, "Modeling of DC–DC converter using exact feedback linearization method: A discussion," *IETE Journal of Research*, vol. 65, no. 6, pp. 843–854, may 2018. [Online]. Available: https://doi.org/10.1080/03772063.2018.1454345

[18] B.-Z. Guo and Z.-L. Zhao, *Active disturbance rejection control for nonlinear systems: An introduction*. John Wiley & Sons, 2016. [Online]. Available: https://doi.org/10.1002/9781119239932

[19] H. Kaeslin, *Top-down digital VLSI design : from architectures to gate-level circuits and FPGAs*. Waltham, MA: Morgan Kaufmann, 2015. [Online]. Available: https://bit.ly/36WnwGh

[20] E. Monmasson, L. Idkhajine, I. Bahri, M-W-Naouar, and L. Charaabi, "Design methodology and FPGA-based controllers for power electronics and drive applications," in *2010 5th IEEE Conference on Industrial Electronics and Applications*. IEEE, jun 2010. [Online]. Available: https://doi.org/10.1109/ICIEA.2010.5515585

[21] J. A. Juárez-Abad, A. P. Sandoval-García, J. Linares-Flores, J. F. Guerrero-Castellanos, P. Banuelos-Sanchez, and M. A. Contreras-Ordaz,

"FPGA implementation of passivity-based control and output load algebraic estimation for transformerless multilevel active rectifier," *IEEE Transactions on Industrial Informatics*, vol. 15, no. 4, pp. 1877–1889, apr 2019. [Online]. Available: https://doi.org/10.1109/tii.2018.2865445

[22] R. M. Lagunes, J. A. Juárez-Abad, B. A. A. López, J. L. B. Avalos, and J. L. Flores, "Control de velocidad de un motor síncrono de imanes permanentes accionado por un inversor trifásico multinivel," *Ingenius*, no. 23, pp. 97–108, dec 2019. [Online]. Available: http://doi.org/10.17163/ings.n23.2020.09

Elaboration of the cabuya fiber in flat fabric as reinforcement matrix for the construction of a rear-view mirror

Elaboración de la fibra de cabuya en tejido plano como matriz de refuerzo para la construcción de un retrovisor

Luis Pruna[1,*], Fabián Velasco[1], Fabián Chachapoya[1], Cristian Paredes[1]

Abstract

Natural fibers are becoming an efficient alternative for industrial applications. This is due to its easy accessibility in the market and for being a renewable raw material. The present work seeks to use the cabuya as reinforcement material with polyester matrix for automotive applications with low cost and weight. This is the case of the rearview mirrors of a vehicle, for which a base mold was manufactured. The applying and molding of the rearview mirror will be carried out on the mold, using cabuya fiber and a polyester resin. The mixtures of cobalt octoate and methyl-ethyl-ketone peroxide (MEKP) with the natural fiber significantly reduce the weight; the manufacturing cost is reduced by approximately 40% due to the easiness to handle this fiber and to obtain this material. The use of the cabuya is recommended for automotive applications (rearview mirror), as it presents a considerable reduction in its weight and relatively low cost compared to the original component.

Keywords: Applications, natural fiber, extraction, molding, process.

Resumen

Las fibras naturales se han convirtiendo en una excelente alternativa para usos industriales. Esto se debe a su fácil accesibilidad en el mercado y por ser una materia prima renovable. El presente trabajo busca usar la cabuya como material de refuerzo con matriz poliéster para aplicaciones automotrices con bajo costo y peso. Este es el caso de los retrovisores de un vehículo, para el cual se fabricó un molde base. Sobre el molde se realizará el aplicado y moldeado del retrovisor utilizando la fibra de cabuya y una resina poliéster. Las mezclas de octoato de cobalto y peróxido de metil-etilcetona (MEKP) con la fibra natural reducen considerablemente el peso; el costo de manufactura se ve reducido aproximadamente en un 40 % debido a la facilidad de manejo de la fibra y la adquisición de este material. Se recomienda la utilización de la cabuya para aplicaciones automotrices (espejo retrovisor) ya que presenta una reducción considerable en su peso y costo relativamente bajo en comparación con el componente original.

Palabras clave: aplicaciones, fibra natural, extracción, moldeado, proceso.

[1,*]Departamento de Ciencias de la Energía y Mecánica. Universidad de las Fuerzas Armadas ESPE, Latacunga, Ecuador. Corresponding author ✉: lrpruna@espe.edu.ec. ⬤ http://orcid.org/0000-0002-0651-9597, ⬤ http://orcid.org/0000-0003-0609-3853, ⬤ http://orcid.org/0000-0001-7015-664X, ⬤ http://orcid.org/0000-0001-5708-5883

1. Introduction

Natural fibers are one-dimensional, long and thin structures. They bend easily, and their main purpose is the manufacture of fabrics. They are classified based on their origin, vegetal, animal or mineral. Likewise, fibers of vegetal origin are classified according to the part of the plant from which they are extracted [1], which enables obtaining a better nomenclature of the fibers produced in new research works.

The cabuya is a plant very common in the central region of Ecuador, where it is used by the farmers to feed the beef cattle. The fiber is obtained through a process which consists of different stages: removal of stalks, crushing, cooking, drying and combing.

In Ecuador, the development of composite materials is at the initial stages, and thus the use of natural fibers is still limited. In general, the extraction of vegetal fibers is carried out manually, but this may change taking into account the great potential offered by the country. It is important to know the production of domestic natural fibers [2].

On the other hand, the need for materials more environmentally friendly has boosted the study of natural polymers for their use in disposable applications, with the purpose of having a material available in nature and also biodegradable [3].

These composite materials represent an important alternative for replacing the reinforced composites based on metal, aluminum, chromium, tungsten, etc.; in many opportunities their properties are comparable or even superior.

Reducing the vehicle weight has been considered as one of the more important solutions to improve fuel saving, reduce weight-power ratio and end up having little or no polluting emissions. It is believed that the weight of the vehicle body can be reduced with the use of multiple materials without cost increase [4].

From the wide variety of composite materials available in the market, they are described as constituted by organic matrices (epoxy, vinylester, polyester) and high resistance fibers (glass, carbon, natural fibers, etc.), considering them as the most developed and the most often used at an industrial level [5].

With respect to the fibers, they are polycrystalline and amorphous materials, with small diameters and great length. In general, the fiber materials are polymers or ceramics (for example, aramids, glass, carbon, boron, aluminum oxide and silicon carbide). There is also the use of natural fibers such as abaca, cabuya and coconut, incorporated as reinforcement elements in a polymeric matrix. This type of materials offer many advantages, among which it can be remarked the reduction of the manufacturing cost and the smaller environmental impact [6].

Traditionally, the weight of the vehicles that take part in automobile competitions is considerably low,

as it is the case of the Formula 1, enabling them to have a great performance, because they use lighter materials in the manufacturing of its components, and with characteristics similar to the originals.

According to the Ministry for Agriculture, Stockbreeding, Aquaculture and Fisheries (Ministerio de Agricultura, Ganadería, Acuacultura y Pesca, MAGAP) approximately 5400 tons of cabuya fiber were produced in Ecuador (2008). The Ecuadorian industries started to conduct tests to determine the resistance of this fiber [8], and thus its possible applications and development of new biodegradable composite materials.

The objective of using natural fibers in the manufacturing of a rearview mirror is facilitating that this element can be recycled, contributing to reduce the environmental impact caused by the automotive industry due to the use of different materials in the production of vehicles, as it is the case of plastics, and at the same time reduce the mass of its components [7, 8].

It is expected to obtain a lighter rearview mirror, with a considerable resistance to deformations due to impacts, as well as a considerable reduction of its manufacturing cost, taking into account a sustainability criterion in each production process; in addition, the possibility of introducing the cabuya fiber in the automotive industry of the country, enabling the development of new applications [9–11].

2. Materials and methods

2.1. Extraction of the cabuya fiber

It is necessary a correct selection of the cabuya plant to obtain stalks of greater size which, in turn, enable obtaining more fibers with less plants, thus improving the production efficiency. The approximate growth period is 5 years before removing the stalks, using a steel bar with sharp tip.

The following steps should be executed to extract the stalk:

1. Cut with a machete the stalk closer to the ground. 2. Chop the plant with the help of the bar in the place of the stalk that was cut (Figure 1), until reaching the center; once this is achieved a perpendicular force must be applied on the bar so that the plant opens (i.e., it is lifted), and all the stalks are freed. 3. Remove with the machete the thorns in each stalk. 4. Take the tip of the stalk with the hand and pull it performing a twisting motion until detaching it from its center. 5. Repeat step 4 with all the stalks. 6. Once all the stalks have been extracted, move them to the fiber extraction area.

Es necesaria una correcta selección de la planta de cabuya para contar con pencas de mayor tamaño que, a su vez, permitan obtener más fibra con menos

plantas, con lo cual mejoramos la eficiencia en la producción. El tiempo aproximado de crecimiento es de 5 años antes de ser despencada utilizando una barra de acero con punta filosa.

Para extraer la penca se deben seguir los siguientes pasos:

1. Cut with a machete the stalk closer to the ground.

2. Chop the plant with the help of the bar in the place of the stalk that was cut (Figure 1), until reaching the center; once this is achieved a perpendicular force must be applied on the bar so that the plant opens (i.e., it is lifted), and all the stalks are freed.

3. Remove with the machete the thorns in each stalk.

4. Take the tip of the stalk with the hand and pull it performing a twisting motion until detaching it from its center.

5. Repeat step 4 with all the stalks.

6. Once all the stalks have been extracted, move them to the fiber extraction area.

Figure 1. Extraction of the fiber.

In order to obtain the fiber, the stalks are crushed on a flat surface with the help of a mallet to extract all the water they have inside. Then, the greenish layer that covers the stalk is removed with a machete. With the help of a wooden board, the surface of the stalk is moved up and down to extract water residues and the protective layer, until obtaining the desired fiber, which may show a greenish white color in certain areas, see Figure 2.

Figure 2. Raw fiber.

Once the fiber is obtained, it is cooked for about 100 minutes; then it acquires an intense white color. It is put out to dry during four days in a wire, attaching it with the help of tweezers. It is important that the fiber does not get wet while it is hanged, since its quality may be harmed (Figure 3). When the fiber is completely dry it shows a pale yellow color; it is further combed using a table with nails to separate the smaller fibers, resulting in a uniform fiber, ready to use.

Figure 3. Cooking and drying of the fiber.

2.2. Weaving of the cabuya fiber

A wooden gridded board is used for weaving the cabuya fiber, in order to have the maximum precision when placing the fiber threads. In this case it was a used a weaving at 90 degrees: the cabuya fiber is placed horizontally at a spacing of 2 mm, while the vertical fibers are placed at a spacing of 10 mm; each of the sets should have a total of 4 threads (Figure 4). The final weaving has 40 cm in width x 30 cm in height.

Figure 4. Weaving of the fiber.

Then, the ends of each group of threads are tied, so that the weaving does not tend to deform during further manipulation.

2.3. Manufacturing process of the rearview mirror

The following process is implemented for manufacturing the rearview mirror:

1. Storage of the corresponding resin and fiber.

2. Preparation of the fiber.

3. Preparation of the mold.

4. Preparation of the mixture.

5. Placement of the matrix (cabuya).

6. Solidification.

7. Demoulding.

8. Sanding.

9. Inspection of the finish.

10. Verification of weights.

An integral cleaning of the original rearview mirror is carried out, and then the mirror is disassembled as well as the remaining accessories (Figure 5).
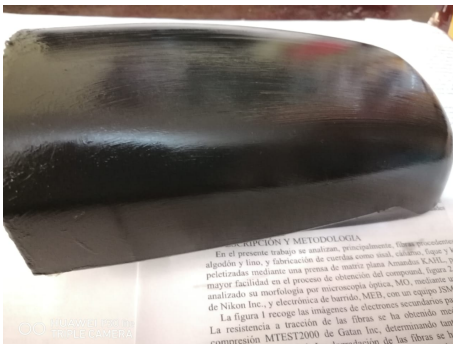
Figure 5. Cleaning of impurities from the original rearview mirror.

When the mold is clean of impurities, it is proceeded to place the mold release wax, as shown in

Figure 6, with the purpose of being able to release the rearview mirror from the mold at the end of the drying.

Figure 6. Application of the mold release wax.

The cabuya fiber is used as matrix; for curing of the resin cobalt octoate and methyl-ethyl-ketoneperoxide (MEKP) or catalyst, as a reinforcement two layers of cabuya fiber are used (Figure 7).
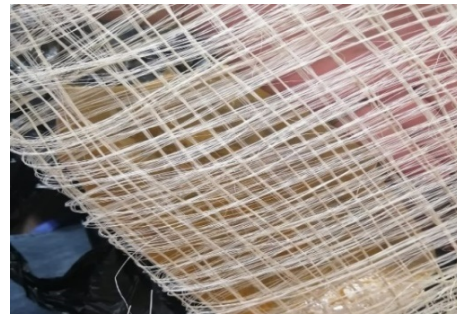
Figure 7. Handmade and hand woven cabuya fiber.

The proportions of resin, cobalt octoate and catalyst must be exact, since the composition shown in Table 1 must be met. A brush is used for applying the mixture, being careful of doing it uniformly to avoid the accumulation in particular areas.

Table 1. Quantities of resin, cobalt octoate, MEKP and cabuya fiber, used for the composite material of the rearview mirror

Description	Quantity
Thickness [mm]	2,5
Number of resin layers	2
Woven cabuya fiber [g]	25
Polyester resin [ml]	150
Cobalt octoate [ml]	0,75
MEKP [ml]	0,4

The parameters which with the rearview mirror will be made are specified in Table 1, as well as the quantity of chemical reagents necessary for a higher drying velocity of the resin. Each part of the rearview mirror is left to dry for three days to achieve better consistency and hardness. Following these recommendations, a rearview mirror with better characteristics

Pruna et al. / Elaboration of the cabuya fiber in flat fabric as reinforcement matrix for the construction of a rear-view mirror

85

of resistance and a significant weight reduction was obtained (Figure 8).

Figure 8. Rearview mirror with a cabuya fiber matrix.

2.4. Design of the mechanism for the 180° rotation

A hinge that continuously opens and closes, similar to the ones used in home doors, serves as the basis for this mechanism, because the rearview mirror should maintain its initial position and recover once it has withstood an impact and has been moved a certain angle from its origin. For this purpose, springs of the same characteristics are placed on the sides of the rearview mirror, so that if it is moved to one side one spring compresses and the other extends, and the mirror returns to its initial state once the application of the force stops. The mechanism is modeled in Autodesk Inventor (Figure 9); it should be analyzed the main points on which the greater stress is exerted when a force is applied on the mechanism. With this information, the necessary precautions are taken in its manufacturing to avoid possible failures during its operation (it may be necessary to reinforce certain areas).
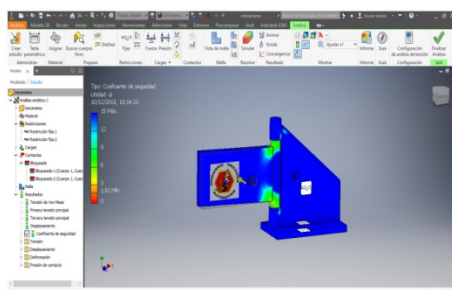
(a)
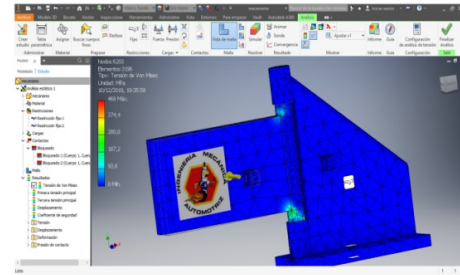
(b)

Figure 9. Analysis of the mechanism in Autodesk Inventor. a) Safety coefficient. b) Von Mises stress

Figure 10 shows the results of the rearview mirror analysis, which should comply with the NTE INEN 1323 Standard.
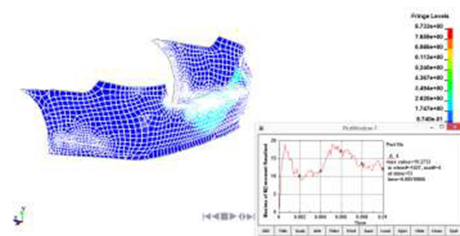
Figure 10. Rearview mirror analysis using the Ansys software.

3. Results and discussion

Table 2 summarizes the comparisons of the weights obtained when using cabuya fiber for manufacturing the rearview mirror, which may be considered as a total success because the measurements obtained show a significant reduction of its weight, thus helping to reduce the weight of the vehicles.

Table 2. Verification of the weights

Description	Weight (kg)
With cabuya fiber and mechanism	0,223
With cabuya fiber and without mechanism	0,1859
Original rearview mirror	0,227

Table 3 shows the behavior of the cabuya fiber rearview mirror when a force is applied on its surface, which enabled to verify the resistance of the 180° rotating mechanism; it was observed that the mounts of the recover springs should be reinforced to avoid the fracture of these small spring holders; similarly it could be visualized that when a larger force is applied on the surface of the rearview mirror it tends to peel off in a small area; the total surface of the rearview mirror is approximately 150 mm^2, on which the resistance analysis will be carried out.

After carrying out the analysis of each of the tests, it could be determined that the cabuya fiber and all

natural fibers have low mechanical resistance, and therefore the accessory to be constructed should not be subject to excessive loads.

Table 3. Impact resistance

	Force/area (MPa)	Force (N)
First test	0,039	5,86
Second test	0,019	2,9
Third test	0,01	1,45

The cabuya fiber has a flexible appearance, its manipulation is simple and it does not fracture easily. In contrast, other fibers are rather fragile, they break easily and are rigid, which results in a difficult manipulation. In the case of cane bagasse the length of its fibers is smaller than those of other specimens, which makes more complex its application in the automotive industry; in addition, these fibers have residues adhered to them that correspond to the ducts where the sucrose is stored, causing a less homogeneous structure.

4. Conclusions

The mixture of cobalt octoate and methyl-ethyl-ketone peroxide (MEKP) with the natural cabuya fiber tends to significantly reduce the weight of the rearview mirror and increase its hardness with respect to the traditionally manufactured rearview mirror. The manufacturing cost is reduced in almost 40 % when this fiber is used.

Due to the easiness to handle the fiber and to obtain the materials to be used, the manual stratification is one of the processes most commonly used for manufacturing equipment in the automotive industry.

The selection of the material or of the natural fiber to be used will depend on the particular requirements of the application. The results are encouraging to try to boost the use of domestic natural fibers in the development of other automotive elements (parts), helping to take care of the environment by obtaining biodegradable products.

References

[1] S. M. Velásquez Restrepo, G. J. Peláéz Arroyave, and D. H. Giraldo Vásquez, "Uso de fibras vegetales en materiales compuestos de matriz polimérica: una revisión con miras a su aplicación en el diseño de nuevos productos," *Informador Técnico*, vol. 80, no. 1, pp. 77–86, jun. 2016. [Online]. Available: https://doi.org/10.23850/22565035.324

[2] D. J. Moreano Moreano and D. A. Zambrano Romero, "Diseño y construcción de parachoques delantero y posterior de un vehículo chevrolet optra año 2008 a partir de fibra natural de la planta de abacá," 2016. [Online]. Available: https://bit.ly/2BuYpid

[3] O. A. Jiménez Arévalo, M. A. Sánchez-Soto, and M. Trujillo Barragán, "Impacto de baja energía en un compuesto almidón-fibra natural," in *XV Congreso Internacional anual de la SOMIM Sonora. México*, 2009, pp. 690–695. [Online]. Available: https://bit.ly/3eMDPrO

[4] H. Iza, L. Quiróz, and F. Salazar, "Aplicación de fibra de yute en la construcción de carrocerías para vehículos fórmula SAE," *Revista: Energía y Mecánica, Innovación y Futuro*, vol. 1, no. 4, pp. 102–111, 2015. [Online]. Available: https://bit.ly/36YdiFx

[5] A. Morales, D. Valenzuela, T. Lozano, and M. Ponce, "Materiales reforzados de poliolefinas recicladas y nanofibras de celulosa de henequén," *Revista Iberoamericana de Polímeros*, vol. 12, no. 5, pp. 255–267, 2011. [Online]. Available: https://bit.ly/2Y1sayy

[6] V. Guerrero, J. Dávila, S. Galeas, P. Pontón, N. Rosas, V. Sotomayor, and D. Valdivieso, *Nuevos Materiales: Aplicaciones Estructurales e Industriales.* Imprefep, 2011. [Online]. Available: https://bit.ly/3gU6Tjg

[7] S. Aguilar, J. Ramírez, and O. Malagón, "Extracción de fibras no leñosas Cabuya (*Furcraea andina Trel.*) y banano (*Musa Paradisiaca L.*) para estandarizar un proceso tecnológico destinado a la elaboración de pulpa y papel," *Revista Iberoamericana de Polímeros*, vol. 8, no. 2, pp. 89–98, 2007. [Online]. Available: https://bit.ly/2XW6LHh

[8] H. G. Villacís Salazar, "Obtención de materiales compuestos híbridos de matriz poliéster reforzados con fibra de vidrio y abacá mediante estratificación," 2011. [Online]. Available: https://bit.ly/306jQjF

[9] S. Kalia, B. S. Kaith, and I. Kaur, *Cellulose Fibers: Bio–and Nano–Polymer Composites.* Springer, Berlin, Heidelberg, 2011. [Online]. Available: https://doi.org/10.1007/978-3-642-17370-7

[10] F. R. Delgado Arcentales, S. G. Galeas Hurtado, and V. H. Guerrero Barragán, "Obtención de materiales compuestos híbridos de matriz poliéster reforzada con fibra de coco y de vidrio para la elaboración de tableros," *Revista Politécnica*, vol. 33, no. 1, 2014. [Online]. Available: https://bit.ly/3gMfO66

[11] A. Mohanty, M. Misra, and L. Drzal, *Natural fibers, biopolimers and biocomposites.* CRC Press, 2005. [Online]. Available: https://bit.ly/3gPyzpk

Monitoring Network to Automate the Cooling System of a Data Center

Red de monitorización para automatizar el sistema de enfriamiento de un centro de datos

José Ignacio Vega-Luna[1,*], Francisco Javier Sánchez-Rangel[1],
Gerardo Salgado-Guzmán[1], José Francisco Cosme-Aceves[1],
Víctor Noé Tapia-Vargas[1], Mario Alberto Lagos-Acosta[1]

Abstract

The objective of this work was to develop a monitoring network of temperature, humidity and air quality in a data center to automate the on and off switching of the cooling, ventilation and air filtering system using IoT (Internet of Things). A network with long-range wireless technology was implemented, consisting of five slave nodes, a master node and a user interface. The slave nodes periodically transmit the value of the three environment variables to the master node. The master node sends the information received from the slaves to a cloud server, so that it can be accessed from a user interface. When the value of any of the variables reaches the configured threshold, the cooling, ventilation and/or filtering system is activated as required. The tests showed that an accuracy of less than ±1.0 °C was obtained in the measurement of temperature, less than ±2 % in the measurement of humidity, less than ±8 μg/m³ in the measurement of air quality and a range of 11.5 kilometers with line of sight was achieved in data transmission over the network. Based on these results, the network can be implemented to monitor sensors and processes in other facilities with this scope.

Keywords: Automation, data center, IoT, monitoring, temperature, wireless.

Resumen

El objetivo de este trabajo fue desarrollar una red de monitorización de temperatura, humedad y calidad del aire en un centro de datos para la automatización del encendido y apagado del sistema de enfriamiento, ventilación y filtrado de aire usando Internet de las cosas (IoT-Internet of Things). Se puso en marcha una red con tecnología inalámbrica de largo alcance compuesta por cinco nodos esclavo, un nodo maestro y una interfaz de usuario. Los nodos esclavo transmiten periódicamente al nodo maestro el valor de las tres variables de ambiente. El nodo maestro envía la información recibida de los esclavos a un servidor en la nube para poder ser accedida desde una interfaz de usuario. Cuando el valor de alguna de las variables alcanza el umbral configurado se enciende el sistema de enfriamiento, ventilación y/o filtrado de aire, según sea el caso. Las pruebas mostraron que se logró una precisión menor a ±1.0 °C en la medida de temperatura, menor a ±2 % en la medida de humedad, menor a ±8 μg/m³ en la medida de la calidad del aire y un alcance de 11.5 kilómetros con línea de vista en la transmisión de datos en la red. Según estos resultados, la red puede ponerse en funcionamiento para la monitorización de sensores y procesos en otras instalaciones con este alcance.

Palabras clave: Automatización, centro de datos, inalámbrica, IoT, monitorización, temperatura.

[1,*]Área de Sistemas Digitales, Departamento de Electrónica, Universidad Autónoma Metropolitana-Azcapotzalco, Ciudad de México, México. Corresponding author ✉: vlji@azc.uam.mx.

 http://orcid.org/0000-0002-4226-2936, http://orcid.org/0000-0002-4182-5856,
 http://orcid.org/0000-0002-0581-7410, http://orcid.org/0000-0002-6875-5683,
 http://orcid.org/0000-0002-1160-2432, http://orcid.org/0000-0003-0455-007X.

1. Introduction

Cooling, ventilation and air filtering are the three critical systems in the operation of a data center or data processing center (DPC). A room temperature increase may cause that the equipment housed in the DPC either stop operating, automatically shut down or even get damaged. The productivity of companies and institutions depends on the access and availability of the computer and telecommunication equipment for clients and users [1], which should be guaranteed by the operation of the DPC. In other words, if the applications are not in operation, the clients and users will not be able to do their work.

Nowadays, the monitoring of environment variables in most DPCs is carried out locally. A computer installed in the control office of the DPC receives the information from the sensors, commonly using an Ethernet segment or 2-Wire technology, and shows it in a user interface [2, 3]. This exhibits the following drawbacks: 1) Not all the surface of the DPC is covered because the sensors are installed at specific places; due to the limitation in the reach of the communication technology being used, it is not possible to access some points from the control office. 2) If for any reason or contingency any variable achieves the threshold value and remains in it for a long time, the only way through which the DPC administrator may know about it is visualizing it in the user interface. There is no mechanism that enables the administrator to react promptly to this eventuality when he or she is not in the control office. 3) In order to carry out the monitoring, as demanded by the audits nowadays, important changes in the user interface must be carried out to enable invoking it from the Internet [4].

This work was carried out on request of a data center. It was required to put into operation a wireless network for sensor monitoring. The network must consist of five slave nodes, strategically installed in the DPC, in charge of periodically measuring the values of temperature, humidity and concentration of PM2.5 particles, and transmitting them to a master node.

The functions of the master node must be: A) Send to a server in the cloud, the information received from the slave nodes. B) Implement the user interface through a web server whose page enables to online visualize the values of the three environment variables. C) If any variable reaches the configured threshold value, activate the cooling, ventilation of air filtering system, as required. D) If the value of a variable is equal to or greater than the threshold during an established time, a WhatsApp alert message must be sent to a mobile phone. E) The control system must be ON/OFF.

The implementation of the network should not require additional wiring nor modifying the one existing in the DPC. The distance from the farthest slave node to the master node is 300 meters.

The periodic monitoring of the variables from the Internet is because it is thus required by the companies and institutions that audit and certify the security and maintenance systems of the data centers [5, 6].

With the latest technological advances, a variety of radiofrequency communication technologies of great geographic coverage, low cost and low energy consumption have arisen; some of them were candidates to be used in the development of this work [7]. Some of these technologies are WiFi, Bluetooth Low Energy (BLE), ZigBee and LoRa (Long Range) [8].

The main features of the four previously mentioned wireless technologies are presented in the following.

The WiFi technology uses low cost transceivers, has a reach between 15 and 25 meters with line of sight, provides a large bandwidth and consumes a relatively high amount of electric power [9].

The BLE technology has a nominal reach of 100 meters with line of sight, provides a medium bandwidth and has low energy consumption [10, 11].

Regarding the ZigBee transceivers, these are low cost devices, with a range of 100 meters, low energy consumption and low bandwidth [12].

On the other hand, the LoRa technology uses low cost transceivers, provides a range of various kilometers with line of sight, has small bandwidth and low energy consumption [13].

Considering the previously mentioned features, it was decided to use the LoRa technology and develop a Low Power Wide Area Network (LPWAN) [14]. Lora is an open protocol developed by the LoRa Alliance that enables creating LPWAN networks for the Internet of Things (IoT) market [15]. The LoRa protocol defines the physical layer of the OSI model or wireless modulation to carry out the long distance communication, using low power radio transceivers that transmit small amounts of information at low speed, achieving a longer life time of the batteries [16].

In addition to the technological advances in wireless communications, the advent of sensors, actuators, microcontrollers and Internet service providers, has strongly boosted the development of IoT applications. The growth of the data centers has been promoted by trends such as IoT, Big Data, e-commerce and cloud use [17].

The monitoring network developed in this work consists of an LPWAN constituted by six nodes, five slaves and one master. The nodes were implemented using the Huzzah32-ESP32 card, which was chosen because it can be programmed using free and open source libraries of functions available in the cloud, which simplified the programming development since a complex low level language was not used.

Recent research works about the use of the LoRa technology, where a long range is required, have resulted in important advancements in different ambits

of human life and process monitoring. For example, this technology has been applied in cities [18], smart homes [19] and buildings [20], farms and agricultural fields [21], healthcare [22] and hospitals, industrial processes [23], electric power consumption [24] and water [25], control of heating systems [26], security [27], fluids [28] and positioning [29], among others.

In parallel, a large number of sensor networks has been created during recent years for remote monitoring of environment parameters, mainly temperature, using IoT. Some of them have been applied in meteorology [30], smart buildings [31, 32], health systems [33], agriculture [34], industrial plants, thermoelectric plants [35] and steel production [36].

Similarly, an important number of applications has been implemented with networks of wireless sensors in data centers through IoT [37]. Most of them have concentrated in the monitoring and operation of cooling systems to achieve an efficient or reduced consumption of electric power [38] and water [39].

On the basis of the above, the benefits and contributions of the authors with the application developed are the following: 1) The monitoring of the variables is carried out remotely using recently developed IoT platforms in the cloud, which provide efficient, reliable and always available services for storing information and sending alert messages to a mobile phone. In most data centers this task is carried out locally, and they are migrating the monitoring to a solution similar to the one developed in this work. 2) It enables taking prompt actions before the occurrence of a contingency in the data center. 3) It fulfills a real need of the data center. 4) The network installation is non-intrusive, since it uses wireless communication and does not modify the wiring of the data center. 5) Its programming is based on free and open source libraries of functions, which reduces its installation time and complexity.

The following sections of this document describe the design, implementation and structure of the monitoring network, explain the tests carried out, as well as their purpose and the results achieved and, at last, present the conclusions obtained and the main recommendations.

2. Materiales y métodos

2.1. Materials and methods

The monitoring network is constituted by three elements: the slave nodes, the master node and the user interface. Figure 1 shows the functional diagram of the monitoring network.
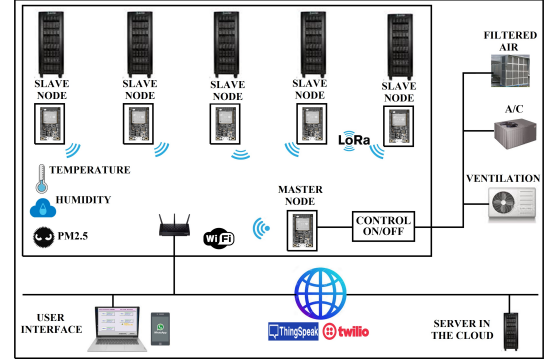
Figure 1. Functional diagram of the monitoring network.

2.2. The slave nodes

The five slave nodes were implemented using the architecture shown in Figure 2.
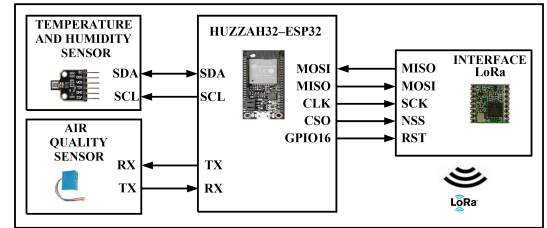
Figure 2. Architecture of the slave nodes.

The components used in each of these nodes were the Huzzah32-ESP32 card, the temperature and humidity sensor, the air quality sensor and the LoRa transceiver. The LoRa technology uses the functionalities of the physical layer, layer 1 of the OSI model, since it determines the type of modulation, the bandwidth and the frequency of the signal used in the network.

The used Huzzah32-ESP32 card has the resources required for the design of the slave nodes, thus reducing their size and cost. The main resources of the card are a Tensilica LX6 Microcontroller with two cores at 240 MHz, 4 MB of flash memory, 520 KB of RAM memory, WiFi 802.11b/g/n interfaces, classic and LE Bluetooth with integrated antenna, 3 UART ports, 3 SPI ports, 2 I^{2}C ports, 25 general purpose input/output (GPIO) and a lithium-ion battery charger.

The temperature and humidity sensor used in the slave nodes was the BME680 device. This digital device integrates four sensors, namely temperature, relative humidity, barometric pressure and gas, in a 3.0×3.0 mm^2 compact metallic packaging. It uses a supply voltage of 3.3 or 5 V, because the card on which it is mounted has a voltage regulator. It is used in automation applications in homes, offices, industries, IoT, weather forecast, air quality measurement and indoor navigation, among others. It has I^{2}C and SPI digital interfaces. The operating ranges are from –40 to +85 °C and from 0 to 100 % of relative humidity (RH). It

can measure temperature with a precision of ± 1.0 °C and humidity with an accuracy of ± 3 %.

In the slave nodes, the communication between the BME680 and the microcontroller of the Huzzah32 card was carried out through the I^{2}C ports. The BME680 works as slave using the 0×77 address of the I^{2}C bus, to provide the value of temperature with a resolution of 20 bits, and the value of humidity with 16 bits. The barometric pressure and gas sensors of the BME680 were disabled to achieve a current consumption of only 2.1 µA and measure only temperature and humidity.

The PMS5003 sensor was used to measure the air quality in the slave nodes. This device measures the number of particles suspended in the air, i.e., the concentration of particles resulting from the operation of internal combustion engine vehicles, from fire generated by wood burning or from industrial processes. It is capable of measuring particles in the environment with diameters of 1, 2.5 and 10 microns, known as PM1.0, PM2.5 y PM10, respectively. Its operation is based on the dispersion of laser light which irradiates the particles suspended in the air, to capture the dispersed laser light and measure the number of particles by unit volume using a processor. The PMS5003 sensor has a UART serial port to digitally transmit the measurement of particles every second. It consumes less than 100 mA in active state and less than 200 µA in passive mode. It operates in the temperature range from –10 to +60 °C and in the humidity range from 0 to 99 % of RH, making it a good candidate to be used in the environment conditions of a data center. In the slave nodes, this sensor was connected to a UART port of the Huzzah32 card, which was configured to operate at a speed of 9,600 bps and measure PM2.5 particles.

The RFM95 circuit is the LoRa transceiver used in the slave nodes. This device has an SPI interface and its main operating features are the following: supply voltage of 3.3 V, output power from +5 to +20 dBm up to 100 mW, current consumption of 100 mA during transmission and 30 mA during active listening, reach of 2 km with line of sight with tuned unidirectional antennas or up to 20 km using directional antennas, RF transmission speed from 0.018 to 37.5 Kbps and transmission speed of the SPI of up to 300 Kbps. The RFM95 transceiver may be configured to be controlled from an external host through the SPI port. The host implements the communication interface between both devices using a master/slave protocol. In this work, the external host is the controller of the Huzzah32 card, which performs as the master, and the RFM95 transceiver performs as the slave. The interface has two types of messages: command packages and response packages. The master always sends command packages, while the slave always transmits response packages. When the master sends a package it should wait until the slave sends a response package, before transmitting another command package. The RFM95 transceiver is a slave, and cannot initiate a transaction with the master. The command packages consist of the following fields: preamble (4 bytes), start of frame (1 byte), type of command (1 byte), number of message (1 byte), length of the message (2 bytes), message (up to 256 bytes) and checksum to verify the integrity of the package (2 bytes). In the slave nodes, the SPI port of the RFM95 transceiver was connected to the SPI port of the Huzzah32 card. To achieve the reach required by the network, the RFM95 transceiver of the nodes uses an external antenna of gain type Omni Lora of 915 MHz, with the following features: gain 8 dBi, female type N connector, impedance 50 ohms and length 1.145 mm.

Regarding the programming of the Huzzah32 card of the slave nodes, it was carried out using the Arduino IDE development environment. The programming is responsible for executing tasks such as configuring the GPIO terminals and the I2C, UART and SPI ports, and initializing the RFM95 transceiver. Afterwards it should perform the reading, every 60 seconds, of the temperature (T), relative humidity and concentration of particles (PM2.5) to transmit it, through the LoRa transceiver, to the master node.

Two open source libraries were utilized to carry out the previous tasks: Adafruit_BME680.h to communicate the Huzzah32 card with the temperature and humidity sensor; Serial.h software to communicate the card with the air quality sensor, and RH_RF95.h and SPI.h for transmitting the information to the master node through the LoRa transceiver and the SPI port, respectively.

2.3. The master node

In a way similar to the slave nodes, the master node was developed using the Huzzah32-ESP32 card and the LoRa RFM95 transceiver. In addition, the master node integrates an electric interface between the Huzzah32 card and the actuators of the air filtering, ventilation and cooling equipment, as shown in the block diagram of the node architecture in Figure 3.
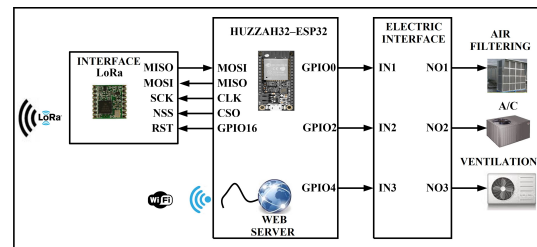
Figure 3. Architecture of the master node.

The functions of the master node were defined programming the Huzzah32 card so that it configures the GPIO terminals and the SPI port, and initializes the

RFM95 transceiver and the WiFi interface. Then, it invokes the function that starts the web server, which may be interrupted when receiving, through the SPI port, the information transmitted by the slave nodes.

The routine for serving the interruption is responsible for reading the information from the SPI port, and transmitting it to the server in the cloud. If the measured value of any of the environment parameters, T, RH or PM2.5 reaches the configured threshold, it activates the actuator of the corresponding equipment. For the case of the temperature the cooling or air conditioning (AC) equipment switches on; when the humidity reaches a maximum the air filtering mechanism is switched on, and when the concentration of particles is equal to or greater than 2.5 microns the ventilation equipment switches on. If the value of one or more of the previous parameters is equal to or greater than the threshold during a configured time, this routine transmits a WhatsApp alert message to the mobile phone through the Twilio service platform. When the value is again below the threshold, it switches off the equipment and transmits the corresponding WhatsApp message.

In addition to the open source libraries of functions used in the slave nodes, the following libraries were used in the programming of the master node: WiFi.h to carry out the communication with the WiFi interface and WebServer.h to implement the web server. Figure 4 illustrates the flow diagram used to develop the master node programming. The server in the cloud used in this work is available through the ThinkSpeak Internet service provider.

The electric interface between the Huzzah32 card and the A/C, air filtering and ventilation equipment was put into operation using a module of four channels of 3 V/125 VAC-250 VAC. This module integrates four SRD-03VDC-SL-C relays of one pole two throws and one optocoupler in each relay to isolate the digital circuit, in this case the Huzzah32 card, from the power circuit. The module relays are supplied with an input voltage of 3 V, and the input IN of each of them is activated from a GPIO terminal of the Huzzah32 card, configured as output, to switch on the equipment of the data center. The equipment actuators are connected to the normally open (NO) output of the corresponding relay, as shown in Figure 5.

2.4. The user interface

The user interface is a page developed with HTML, which is shown when the connection to the web server is established. Figure 6 shows the main page of the user interface through which the measured values of temperature, relative humidity and concentration of PM2.5 transmitted by each slave node, are visualized online.
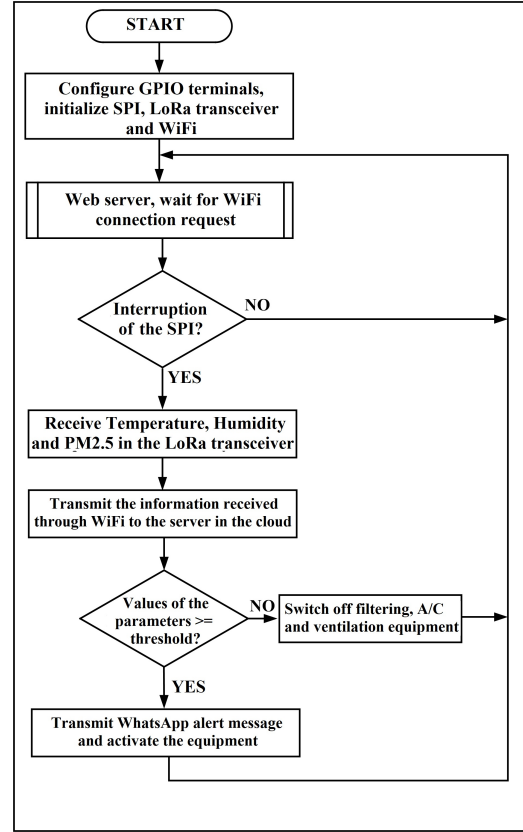
Figure 4. Flow diagram of the master node programming .
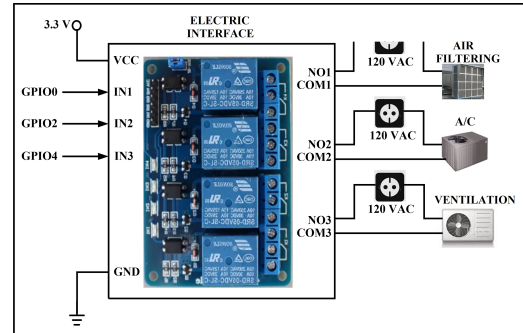
Figure 5. Electric interface of the master node .
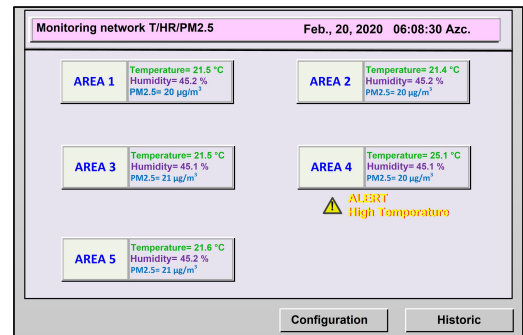
Figure 6. User interface.

For each slave node, there is a button in the interface under which an alert signal is indicated when the value of any of the parameters reach the threshold. When the button of one slave node is pressed, the user interface shows the real-time plot of the values obtained from ThinkSpeak, as shown in Figure 7.

Figure 8. Precision in the measurement of temperature.

Figure 7. Plots of temperature and humidity in ThinkSpeak.

In addition, the interface has two buttons: Configuration, which enables to establish the number of mobile phone and threshold values for T, RH and PM2.5, and Historic, which can be used to download, from ThinkSpeak, the historic measured values of the parameters during a selected period of time, and store them in a text file. In general, this is the file requested during the audits to the data centers.

3. Results and discussion

Three groups of tests were conducted. The first group had the objective of determining the precision of the temperature measured by the monitoring network. To carry out these tests, the temperature in the sensor of a slave node was artificially set to different values, using a heater. Then, the temperature was measured around the slave node with an analog thermometer, similar to the one employed in the audits, and used as reference, i.e., this value was compared with the value reported in the user interface. The manufacturer of the BME680 sensor indicates a nominal precision of ± 1.0 °C in the measured temperature [40]. The results of these tests showed that the real precision is smaller than ± 1.0 °C which was maintained up to 68 °C. When the temperature increases above this value, the difference between the value indicated in the thermometer and the one reported in the interface increased proportionally, as shown in Figure 8.

During the previous tests, there were no problems in the communication between the nodes of the network. The distance between the farthest slave node and the master node is 300 meters. However, a second group of tests was conducted to determine the reach of this network.

The signal transmitted by the nodes is subject to interferences, and is diffracted or absorbed in the medium; the reach of the network depends on the value of power established in the LoRa transceiver, environmental factors and obstacles in the signal route. The previous tests were carried out under the following conditions: with line of sight between the nodes, the RF transmission power in the RFM95 transceiver was configured to 20 dBm-100 mW, RF frequency 915 MHz, bandwidth BW 125 KHz and the temperature and relative humidity of the environment were 21.5 °C and 45.1 %, respectively.

When carrying out the second set of tests, a slave node was located at different distances from the master node with line of sight. The measurements reported in the user interface were verified at each location. The results of these tests indicated that the reach of the network is 11.5 kilometers with line of sight. At larger distances, the link between the slave node and the master node was lost. In this group of tests a program was developed and executed in the master node, to show the value of the Received Signal Strength Indication (RSSI) in the Arduino IDE. Results indicated that the attenuation of the RSSI value is significantly reduced after 9.2 kilometers, and continues to reduce constantly until the communication is lost at 11.5 kilometers, as indicated in Figure 9. In case of using this network in a place with different environmental conditions, it is recommended to conduct these tests to determine the reach limitations.
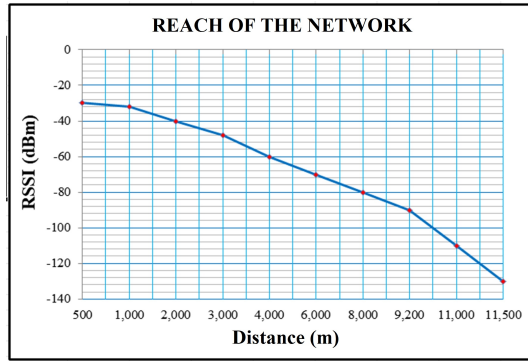
Figure 9. Reach of the network.

The purpose of the third group of tests was to verify the sending of WhatsApp alert messages. In these tests, smoke was artificially generated burning a piece of wood in the five slave nodes, to produce particles greater than 2.5 microns. The slave nodes reported the event in the user interface, and the message was correctly transmitted and received in the mobile phone with an approximate delay time of 1.75 seconds after the occurrence of the event. In both this set and in the first set of tests, one of the slave nodes reached the temperature threshold, as shown in Figure 10.
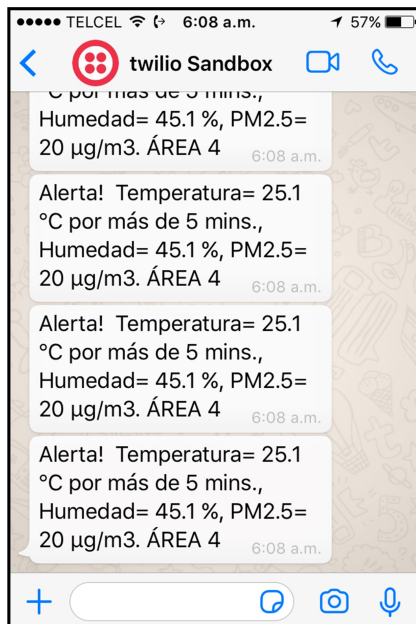
Figure 10. Alert message sent to the mobile phone.

4. Conclusions

Based on the results obtained it is concluded that the installation of the monitoring network is non-intrusive, since it is not necessary to install additional wiring for its operation; the reach of 11.5 kilometers is greater than the reach that can be achieved using traditional wireless technologies, sensors may be added to the slave nodes to access the information of other type of variables making slight changes in the programming.

The application developed here may be easily replied in other data centers or in other type of facilities, where it is necessary to remotely monitor processes using an IoT solution whose programming is based on free and open source software. It is recommended that a ThinkSpeak license is used if the monitoring time of the variables or processes is smaller than 30 seconds, because the amount of messages sent will exceed the maximum amount established in the software used in this work which has no cost.

In the short term, it is planned to work in two aspects of the system: to increase the reach of the network by integrating slave nodes configured as repeaters, and to develop a user interface which executes in mobile devices.

References

[1] X. Ma, Z. Zhang, and S. Su, "Cost-aware multi-domain virtual data center embedding," *China Communications*, vol. 15, no. 12, pp. 190–207, 2018. [Online]. Available: https://bit.ly/2XT3VUB

[2] C. Sun, Y. Wen, P. Li, W. Ye, J. Yang, J. Qiu, and J. Wen, "Self-contained wireless hall current sensor applied for two-wire zip-cords," *IEEE Transactions on Magnetics*, vol. 52, no. 7, pp. 1–4, 2016. [Online]. Available: https://doi.org/10.1109/TMAG.2016.2524671

[3] S. Baig, W. Iqbal, J. L. Berral, A. Erradi, and D. Carrera, "Real-time data center's telemetry reduction and reconstruction using markov chain models," *IEEE Systems Journal*, vol. 13, no. 4, pp. 4039–4050, 2019. [Online]. Available: https://doi.org/10.1109/JSYST.2019.2918430

[4] G. Zhabelova, M. Vesterlund, S. Eschmann, Y. Berezovskaya, V. Vyatkin, and D. Flieller, "A comprehensive model of data center: From cpu to cooling tower," *IEEE Access*, vol. 6, pp. 61 254–61 266, 2018. [Online]. Available: https://doi.org/10.1109/ACCESS.2018.2875623

[5] SEGOB, *Declaratoria de vigencia de la Norma Mexicana NMX-C-506-ONNCCE-2015*. Diario Oficial de la Federación. Secretaría de Gobernación. México., 2015. [Online]. Available: https://bit.ly/2BYWOS1

[6] TIA. (2019) Tia launches ansi/tia-942 accreditation scheme for certification of data centers, selects certac to manage program. [Online]. Available: https://bit.ly/2XTtgxB

[7] Q. Ren, L. Wang, J. Huang, C. Zhang, and Q. Huang, "Simultaneous remote sensing of temperature and humidity by lc-type passive wireless sensors," *Journal of Microelectromechanical Systems*, vol. 24, no. 4, pp. 1117–1123, 2015. [Online]. Available: https://doi.org/10.1109/JMEMS.2014.2384591

[8] C. Jiang, Y. Qiu, H. Gao, T. Fan, K. Li, and J. Wan, "An edge computing platform for intelligent operational monitoring in internet data centers," *IEEE Access*, vol. 7, pp. 133 375–133 387, 2019. [Online]. Available: https://doi.org/10.1109/ACCESS.2019.2939614

[9] M. Ayaz, M. Ammad-uddin, I. Baig, and E. M. Aggoune, "Wireless sensor's civil applications, prototypes, and future integration possibilities: A review," *IEEE Sensors Journal*, vol. 18, no. 1, pp. 4–30, 2018. [Online]. Available: https://doi.org/10.1109/JSEN.2017.2766364

[10] S. Yu, P. Feng, and N. Wu, "Passive and semi-passive wireless temperature and humidity sensors based on epc generation-2 uhf protocol," *IEEE Sensors Journal*, vol. 15, no. 4, pp. 2403–2411, 2015. [Online]. Available: https://doi.org/10.1109/JSEN.2014.2375180

[11] D. Morrison, T. Ablitt, and J. Redouté, "Miniaturized low-power wireless sensor interface," *IEEE Sensors Journal*, vol. 15, no. 9, pp. 4731–4732, 2015. [Online]. Available: https://doi.org/10.1109/JSEN.2015.2442235

[12] J. Chou, J. Chen, Y. Liao, C. Lai, R. Chen, Y. Tsai, C. Lin, J. Chen, M. Huang, and H. Chou, "Wireless sensing system for flexible arrayed potentiometric sensor based on xbee module," *IEEE Sensors Journal*, vol. 16, no. 14, pp. 5588–5595, 2016. [Online]. Available: https://doi.org/10.1109/JSEN.2016.2570285

[13] T. Wang, Z. Su, Y. Xia, and M. Hamdi, "Rethinking the data center networking: Architecture, network protocols, and resource sharing," *IEEE Access*, vol. 2, pp. 1481–1496, 2014. [Online]. Available: https://doi.org/10.1109/ACCESS.2014.2383439

[14] O. Georgiou and U. Raza, "Low power wide area network analysis: Can lora scale?" *IEEE Wireless Communications Letters*, vol. 6, no. 2, pp. 162–165, 2017. [Online]. Available: https://doi.org/10.1109/LWC.2016.2647247

[15] Q. Zhou, K. Zheng, L. Hou, J. Xing, and R. Xu, "Design and implementation of open lora for iot," *IEEE Access*, vol. 7, pp. 100 649–100 657, 2019. [Online]. Available: https://doi.org/10.1109/ACCESS.2019.2930243

[16] T. Elshabrawy and J. Robert, "Interleaved chirp spreading lora-based modulation," *IEEE Internet of Things Journal*, vol. 6, no. 2, pp. 3855–3863, 2019. [Online]. Available: https://doi.org/10.1109/JIOT.2019.2892294

[17] B. Buurman, J. Kamruzzaman, G. Karmakar, and S. Islam, "Low-power wide-area networks: Design goals, architecture, suitability to use cases and research challenges," *IEEE Access*, vol. 8, pp. 17 179–17 220, 2020. [Online]. Available: https://doi.org/10.1109/ACCESS.2020.2968057

[18] M. Sidorov, P. V. Nhut, Y. Matsumoto, and R. Ohmura, "Lora-based precision wireless structural health monitoring system for bolted joints in a smart city environment," *IEEE Access*, vol. 7, pp. 179 235–179 251, 2019. [Online]. Available: https://doi.org/10.1109/ACCESS.2019.2958835

[19] G. Premsankar, B. Ghaddar, M. Slabicki, and M. Di Francesco, "Optimal configuration of lora networks in smart cities," *IEEE Transactions on Industrial Informatics*, pp. 1–1, 2020. [Online]. Available: https://doi.org/10.1109/TII.2020.2967123

[20] W. Xu, J. Y. Kim, W. Huang, S. S. Kanhere, S. K. Jha, and W. Hu, "Measurement, characterization, and modeling of lora technology in multifloor buildings," *IEEE Internet of Things Journal*, vol. 7, no. 1, pp. 298–310, 2020. [Online]. Available: https://doi.org/10.1109/JIOT.2019.2946900

[21] S. Benaissa, D. Plets, E. Tanghe, J. Trogh, L. Martens, L. Vandaele, L. Verloock, F. A. M. Tuyttens, B. Sonck, and W. Joseph, "Internet of animals: characterisation of lora sub-ghz off-body wireless channel in dairy barns," *Electronics Letters*, vol. 53, no. 18, pp. 1281–1283, 2017. [Online]. Available: https://doi.org/10.1049/el.2017.1344

[22] F. Wu, J. Redouté, and M. R. Yuce, "We-safe: A self-powered wearable iot sensor network for safety applications based on lora," *IEEE Access*, vol. 6, pp. 40 846–40 853, 2018. [Online]. Available: https://doi.org/10.1109/ACCESS.2018.2859383

[23] J. P. Shanmuga Sundaram, W. Du, and Z. Zhao, "A survey on lora networking: Research problems, current solutions, and open issues," *IEEE Communications Surveys Tutorials*, vol. 22, no. 1, pp. 371–388, 2020. [Online]. Available: https://doi.org/10.1109/COMST.2019.2949598

[24] A. Javed, H. Larijani, and A. Wixted, "Improving energy consumption of a commercial building

with iot and machine learning," *IT Professional*, vol. 20, no. 5, pp. 30–38, 2018. [Online]. Available: https://doi.org/10.1109/MITP.2018.053891335

[25] O. Khutsoane, B. Isong, N. Gasela, and A. M. Abu-Mahfouz, "Watergrid-sense: A lora-based sensor node for industrial iot applications," *IEEE Sensors Journal*, vol. 20, no. 5, pp. 2722–2729, 2020. [Online]. Available: https://doi.org/10.1109/JSEN.2019.2951345

[26] L. Zhao, W. Wu, and S. Li, "Design and implementation of an iot-based indoor air quality detector with multiple communication interfaces," *IEEE Internet of Things Journal*, vol. 6, no. 6, pp. 9621–9632, 2019. [Online]. Available: https://doi.org/10.1109/JIOT.2019.2930191

[27] P. Kulkarni, Q. O. A. Hakim, and A. Lakas, "Experimental evaluation of a campus-deployed iot network using lora," *IEEE Sensors Journal*, vol. 20, no. 5, pp. 2803–2811, 2020. [Online]. Available: https://doi.org/10.1109/JSEN.2019.2953572

[28] L. Leonardi, F. Battaglia, and L. Lo Bello, "Rt-lora: A medium access strategy to support real-time flows over lora-based networks for industrial iot applications," *IEEE Internet of Things Journal*, vol. 6, no. 6, pp. 10 812–10 823, 2019. [Online]. Available: https://doi.org/10.1109/JIOT.2019.2942776

[29] K. Lam, C. Cheung, and W. Lee, "Rssi-based lora localization systems for large-scale indoor and outdoor environments," *IEEE Transactions on Vehicular Technology*, vol. 68, no. 12, pp. 11 778–11 791, 2019. [Online]. Available: https://doi.org/10.1109/TVT.2019.2940272

[30] R. I. S. Pereira, S. C. S. Jucá, P. C. M. Carvalho, and C. P. Souza, "Iot network and sensor signal conditioning for meteorological data and photovoltaic module temperature monitoring," *IEEE Latin America Transactions*, vol. 17, no. 06, pp. 937–944, 2019. [Online]. Available: https://doi.org/10.1109/TLA.2019.8896816

[31] X. Zhang, M. Pipattanasomporn, T. Chen, and S. Rahman, "An iot-based thermal model learning framework for smart buildings," *IEEE Internet of Things Journal*, vol. 7, no. 1, pp. 518–527, 2020. [Online]. Available: https://doi.org/10.1109/JIOT.2019.2951106

[32] L. Zhao, W. Wu, and S. Li, "Design and implementation of an iot-based indoor air quality detector with multiple communication interfaces," *IEEE Internet of Things Journal*, vol. 6,

no. 6, pp. 9621–9632, 2019. [Online]. Available: https://doi.org/10.1109/JIOT.2019.2930191

[33] M. M. Alam, H. Malik, M. I. Khan, T. Pardy, A. Kuusik, and Y. Le Moullec, "A survey on the roles of communication technologies in iot-based personalized healthcare applications," *IEEE Access*, vol. 6, pp. 36 611–36 631, 2018. [Online]. Available: https://doi.org/10.1109/ACCESS.2018.2853148

[34] J. Ruan, Y. Wang, F. T. S. Chan, X. Hu, M. Zhao, F. Zhu, B. Shi, Y. Shi, and F. Lin, "A life cycle framework of green iot-based agriculture and its finance, operation, and management issues," *IEEE Communications Magazine*, vol. 57, no. 3, pp. 90–96, 2019. [Online]. Available: https://doi.org/10.1109/MCOM.2019.1800332

[35] Q. Wan, Y. Teh, Y. Gao, and P. K. T. Mok, "Analysis and design of a thermoelectric energy harvesting system with reconfigurable array of thermoelectric generators for iot applications," *IEEE Transactions on Circuits and Systems I: Regular Papers*, vol. 64, no. 9, pp. 2346–2358, 2017. [Online]. Available: https://doi.org/10.1109/TCSI.2017.2708763

[36] Y. Han, C. Zhang, L. Wang, and Y. Zhang, "Industrial iot for intelligent steelmaking with converter mouth flame spectrum information processed by deep learning," *IEEE Transactions on Industrial Informatics*, vol. 16, no. 4, pp. 2640–2650, 2020. [Online]. Available: https://doi.org/10.1109/TII.2019.2948100

[37] C. Yang, D. Puthal, S. P. Mohanty, and E. Kougianos, "Big-sensing-data curation for the cloud is coming: A promise of scalable cloud-data-center mitigation for next-generation iot and wireless sensor networks," *IEEE Consumer Electronics Magazine*, vol. 6, no. 4, pp. 48–56, 2017. [Online]. Available: https://doi.org/10.1109/MCE.2017.2714695

[38] K. Kaur, S. Garg, G. Kaddoum, E. Bou-Harb, and K. R. Choo, "A big data-enabled consolidated framework for energy efficient software defined data centers in iot setups," *IEEE Transactions on Industrial Informatics*, vol. 16, no. 4, pp. 2687–2697, 2020. [Online]. Available: https://doi.org/10.1109/TII.2019.2939573

[39] L. Yang, Y. Deng, L. T. Yang, and R. Lin, "Reducing the cooling power of data centers by intelligently assigning tasks," *IEEE Internet of Things Journal*, vol. 5, no. 3, pp. 1667–1678, 2018. [Online]. Available: https://doi.org/10.1109/JIOT.2017.2783329

[40] Bosch, "Gas sensor measuring relative humidity, barometric pressure, ambient temperature and gas (VOC) BME680," Bosch Sensortec GmbH 2020, Tech. Rep., 2017. [Online]. Available: https://bit.ly/2YlAvNS

Numerical Analisys of a Water Heating System Using a Flat Plate Solar Collector

Análisis numérico de un sistema de calentamiento de agua utilizando un colector solar de placa plana

William Quitiaquez[1,*], José Estupiñán-Campos[2], C. A. Isaza-Roldán[1],

Fernando Toapanta-Ramos[2], Andrés Lobato-Campoverde[2]

Abstract

The objective of the present research work was to carry out a numerical analysis by means of CFD of a flat plate solar collector, in addition to a comparison with experimental results. The working fluid reached a maximum outlet temperature of 20.16 °C at 12:00, the value of solar radiation was determined for the geographical coordinates latitude -0.2252 and longitude -77.84; similarly, at this time it was possible to obtain a temperature of 27.12 °C on the collector surface, as peak value. The lowest performance of the heat transfer device was determined at 10:00 with an outlet water temperature and maximum temperature on the collector surface of 18.65 and 20.48 °C, respectively. The experimental results showed a maximum temperature of 20.93 °C and a minimum temperature of 19.4 °C, resulting in a 4.01 % error between the computational simulation and the experimental data.

Keywords: Collector, solar energy, temperature, CFD simulation.

Resumen

El objetivo de la presente investigación fue realizar un análisis numérico mediante CFD de un colector solar de placa plana; además, se realizó una comparación con resultados experimentales. El fluido de trabajo alcanzó una temperatura máxima de salida de 20.16 °C a las 12:00, el valor de la radiación solar se determinó para las coordenadas geográficas latitud -0.2252 y longitud -77.84; de forma similar, en este horario fue posible obtener una temperatura de la superficie del colector de 27.12 °C, como valor pico. Se determinó el menor rendimiento del dispositivo de transferencia de calor a las 10:00 con un valor de temperatura de salida del agua y temperatura máxima en la superficie del colector de 18.65 y 20.48 °C, respectivamente. Los resultados experimentales mostraron una temperatura máxima de 20.93 °C y una temperatura mínima de 19.4 °C, derivando en un error de 4.01 % entre la simulación computacional y los datos experimentales.

Palabras clave: colector, energía solar, temperatura, simulación CFD

[1,*]Centro de Investigación en Refrigeración y Aire Acondicionado, Universidad Pontificia Bolivariana, Colombia.
Corresponding author ✉: william.quitiaquez@upb.edu.co.
 https://orcid.org/0000-0001-9430-2082, https://orcid.org/0000-0002-5902-6411
[2]Carrera de Ingeniería Mecánica / GIERIMP, Universidad Politécnica Salesiana, Quito, Ecuador.
 https://orcid.org/0000-0003-2286-5737, https://orcid.org/0000-0002-0838-4702,
 https://orcid.org/0000-0002-6073-3439 .

1. Introduction

At present, it has been observed how the scientific community has become aware about the use of energy renewable sources, due to many studies about the damages produced by the burning of fossil fuels for the generation and use of energy. For this reason, in recent years there has been an increase in the research and experimental works about the use of solar energy for increasing the temperature of fluids using thermal solar collectors; among them there are the concentrating solar collectors which have determined that the operating range varies between 50 and 300 °C [1].

Taking advantage of this virtually renewable resource has more impact in places with an appropriate geographic location to optimize the performance of heat transfer devices with the assistance of solar energy, due to the appropriate and invariant angle of incidence by the influence of the seasons, as it is the case of countries in the equatorial region such as Ecuador [2].

Ayompe and Duffy [3], in their research work about the thermal performance of a water heating solar system with flat plate collectors applied along one year at a forced circulation household scale system, show that the obtained results corresponded to a yearly average of collected daily energy of 19.6 MJ/day, a solar fraction of 32.2 %, and, in addition, a collector and system efficiency of 37.8 and 45.6 %, respectively.

There are various external agents involved in the operation of a solar collector, namely the ambient temperature, irradiation, geographic position, among others, as stated by Hashim *et al.* [4]. In their work they show the influence of the volumetric flow in the temperature that the working fluid may reach when leaving the solar collector; in their experimental research they conducted two tests with flow rates of 5.3 and 6.51 L·min^{-1}, respectively, obtaining as results output temperatures of 51.4 and 49 °C, reaching the conclusion that as the volumetric flow rate decreases a greater temperature may be reached at the outlet of the collector.

The Computational Fluid Dynamics (CFD) is of great help in studies that seek to improve the performance of heat transfer devices. For this reason it is regularly used to develop improved designs of various mechanisms that require energy transfer, such as solar

air heaters, and to evaluate the potential of power generation [5].

In their research, Marroquín *et al.* [6] use the AN-SYS simulation software, specifically its library for fluid dynamics (CFD). The CFX-Mesh is utilized for the meshed, where it is considered a face space in the elements between 0.004 and 0.08 m, a resolution angle of 30°; regarding the simulation, it is carried out under the k-epsilon energy model due to the turbulent flow, obtaining a result that varies 5% with respect to the experimentation.

It is possible to perform a comparative analysis to validate the results of the CFD analysis with experimental results seeking to find a permissible error margin as stated by Mohamed *et al.* [7], who in their study of a Direct Expansion Solar Assisted Multifunctional Heat Pump (DX-SAMHP) take real parameters such as external ambient temperature during winter from –1 to 5 °C, solar radiation of 0, 57, 100 and 200 W·m^{-2} to enter them in the simulator, obtaining larger values in the modeling compared to the experimental results, with average deviations of ± 4 %.

Similarly, the research work by Duarte *et al.* [8] presents a comparative study to validate the results of the mathematical model with experimental values, where a heat pump is utilized with a collector/evaporator of 1.65 m^2, ambient temperature between 27.1 and 31.6 °C, solar radiation between 0 and 811 W·m^{-2}, among other parameters, thanks to which the simulation generates a difference in the COP of 1.6 %, smaller than the experimental uncertainty of 5 %.

Likewise, the efficiency of the flat plate solar collectors may vary by the influence of other conditions such as the cross sections through which the working fluid circulates, as shown by Andrade *et al.* [9], who validate their research work by means of a CFD simulation; in addition, they show a final temperature of 330 K at the outlet of the pipe, and an efficiency of 68 %.

There are many research works about the use of solar collectors in heating systems, which are carried out in different countries, as shown in Table 1, where simulation proposals are validated experimentally for a more precise development.

Similarly, some works seek to numerically validate experimental proposals to find limitations in the design, which shows the importance of the complementarity between the simulation and experimental parts.

Table 1. Research works carried out in different systems with flat plate solar collectors

	Ji *et al.* [10]	Mohamed *et al.* [7]	Duarte *et al.* [8]	Fathabadi [11]	Rabelo *et al.* [12]	Kong *et al.* [13]
1. Type of solar collector						
Flat plate with cover	x	x	x	x		
Flat plate without cover					x	x
2. Aplication						
Hot sanitary water		x	x	x	x	x
Space heating	x					
3. Country	China	Sudán	Brasil	Grecia	Brasil	China
4. Area of the collector (m^2)	4	4.22	1.65	2.42	1.57	2.1
5. Length of the collector (m)	2	-	-	1.981	-	1.448
6. Validation	Experimental	Experimental and numerical	Experimental and numerical	Experimental	Experimental	Experimental

1.1. Description of the solar collector

The design of the equipment utilized for carrying out the present work consists of a tube, in which the energy exchange to the working fluid (water) takes place, covered with a metallic plate with two wings, as illustrated in Figure 1.

Figure 1. Schematic diagram of the solar collector

In pursuit of improving the heat transfer in the device, and thus considerably increasing its efficiency, the material considered in the model of the solar collector is copper for the metallic cover with the wings and the tube through which the working fluid circulates, with the dimensions specified in Table 2, taking into account the variables that directly impact on the temperature increase in the fluid, between the inlet and the outlet of the collector.

Table 2. Detailed specifications of the solar collector

Description	Specification
Length of the absorbing plate	0.960 m
Thickness of the absorbing plate	0.001 m
Thermal conductivity of the plate	387.6 W·m^{-1}·K^{-1}
Density of the plate material	8978 kg·m^{-3}
Thickness of the plate	0.001 m
Diameter of the conductive tube	0.0165 m
Thickness of the incremental and conductive tube	0.002 m
Total area	1.728 m^2

1.2. Operating principle of the system

The working fluid begins its circulation through the system entering at ambient temperature (T_{amb}) in the solar collector, where as a result of the heat transferred by the solar energy (Q_E) it reaches a temperature at the outlet (T_1) larger than at the inlet, then enters a tank where it losses part of the heat gained (Q_{P1}) until entering the pump where it gains work (W) to move to a second tank where it losses the remaining heat gained in the solar collector (Q_{P2}) and then reenters the solar collector at ambient temperature, as detailed in Figure 2.
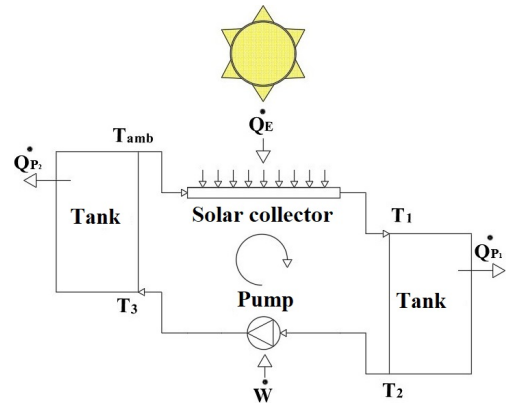
Figure 2. Cycle of the working fluid in the solar collector

2. Materials and methods

In a solar collector heat is transferred in three different ways: conduction, convection and radiation, which occur due to the solar radiation striking the device, and the temperature difference between the working fluid and the ambient air T_∞, as seen in Figure 3.

Figure 3. Heat transfer in a solar collector

Convection and radiation are due to the heat transfer through the ambient air up to the device surface, and to the solar energy received by the collector, respectively. On the other hand, conduction occurs due to the heat transfer between the solar collector surface, as shown in Figure 4.

Figure 4. Network of thermal resistances in a solar collector

The heat transfer by conduction (q), explained by Fourier's law, is proportional to the temperature gradient (dT/dx) multiplied times the area (A) through which the energy is transferred; the relationship between the local temperature (T), the distance in the direction of heat flow (x) and the thermal conductivity (k) is shown in Equation (1) [14].

$$q = -k \cdot A \cdot \frac{dT}{dx} \qquad (1)$$

The heat exchange by convection (Q_{cv}) for a model can be expressed as the process of heat convection between the internal and external surfaces of the envelope of a surface as expressed in Equation (2) [15].

$$\dot{Q}_{cv} = h \cdot A_S \cdot (T_S - T_\infty) \qquad (2)$$

Where (h) represents the convection heat transfer coefficient, (A_S) the surface area, (T_S) the temperature of the surface and (T_∞) the temperature of the fluid at a certain distance of the surface. It should be considered that the temperature of the fluid is equal to the temperature on the surface of the solid in the contact area [16]. Regarding convection, it is important to classify it in two types: natural or free and forced.

The intensity of natural convection is measured by the Grashof (Gr) and Prandtl (Pr) number, which is shown in Equation (3), these dimensionless numbers are characteristic of free convection, since when they increase, the transition of the flow regime becomes insignificant as stated by Meyer and Everts [17].

$$Gr = \frac{g \cdot \partial \cdot \beta \cdot (T_2 - T_1) \cdot L^3}{\mu^2} \qquad (3)$$

Where (g) represents the gravity, (∂) the density, (β) the volumetric expansion coefficient, (T_2 y T_1) are the temperatures at the boundary, (L) the wall length and (μ) the dynamic viscosity [18]. The free convection heat transfer can be quantified by means of the Nusselt number, which varies as a functio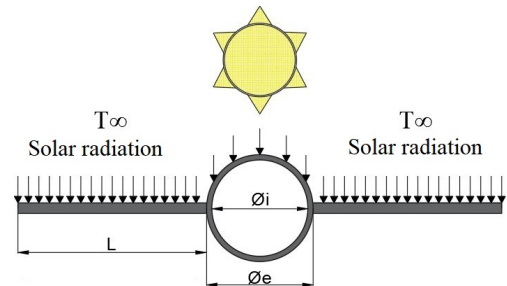n of the conditions in which the heat exchange takes place, in this case of free convection, it is related to the dimensionless Rayleigh (R_a) number shown in Equation (4), which results from the product of the Grashof and Prandtl numbers [19].

$$Ra = \frac{g \cdot \beta \cdot (T_2 - T_1) \cdot R^3}{\nu \cdot \alpha} \qquad (4)$$

For correct calculation of the Rayleigh number it is necessary to take into account the volumetric expansion coefficient, the temperature of the fluid (T_2), the temperature of the enclosure wall (T_1), the radius of the enclosure (R), the cinematic viscosity (ν) and the thermal diffusivity (α) [20]. The thermal radiation is the energy emitted by any type of matter which is at a temperature greater than zero and whose energy diffusion is shown in Equation (5), where it is presented [21].

$$q = k_a \cdot 4\sigma \cdot T^4 \qquad (5)$$

Equation (5) presents the heat transfer of the radioactive source (q), the thermal conductivity (k_a), the Stefan-Boltzmann constant ($\sigma = 5.67 \times 10^{-8}\ W \cdot m^{-2} \cdot K^{-4}$) in units of the International System (SI) and the temperature distribution due to the limit of the physical media (T) [22].

2.1. Parameters of the fluid at the inlet of a flat solar collector

Some important conditions of the working fluid at the inlet of a flat solar collector were: velocity, mass flow, gauge pressure, ambient temperature, among others, as seen in Table 3, which have been collected from different research works that show the conditions at the inlet of a solar collector.

Table 3. Conditions of the fluid at the inlet of the solar collector

Properties	Cetina-Quiñones *et al.* [23]	Pang *et al.* [24]	Visa *et al.* [25]
Temperature	45 °C	27 °C	20 °C
Volumetric flow	$0.0167 \ \text{L} \cdot \text{s}^{-1}$	$0.05 \ \text{L} \cdot \text{s}^{-1}$	——
Pressure	——	——	300 kPa
Mass flow	——	$0.1 \ \text{kg} \cdot \text{s}^{-1}$	$0.02 \ \text{kg} \cdot \text{s}^{-1}$
Internal diameter	0.0254 mm	——	0.008 m
Working fluid	Water	Water	Water
Material of the pipe	——	Copper	Aluminum

2.2. Meshed and modeling

To correctly analyze the different properties of the solids, liquids and gases with the simulation software, it is necessary to construct an efficient computational mesh, which may be constituted by pyramidal, tetrahedral or hexahedral cells that divide the body in various smaller subsets [26]. To generate a correct mesh of the fluid section it is recommended to use tetrahedral cells due to their adaptability with the curved regions crossed by the fluid.

The independence of the meshed is important to determine the optimal mesh number, which means that the solution is independent of the mesh resolution. In the 3D CFD analysis it is common to carry out simulations using different mesh sizes to compare the results, despite this it is possible to find variations smaller than 0.5 % in the temperatures, which indicates that this does not have a significant impact on the results [27].

In the current case study it was required a differentiated meshed as illustrated in Figure 5. To obtain the mesh, a patch conforming tetrahedral method was utilized in the curved figures of the working fluid and of the tube that contains it, edge sizing along the joints between the wings and the arc in the collector wall with an angle of curvature of 5°, which is shown in Table 4 as mesh 1; in this way, typical hexahedrons and tetrahedrons are utilized in the CFD analysis of the solar collectors, heterogeneous distribution of its elements and different number of neighboring elements, which represent an unstructured meshed to improve the convergence of the result [28].

Due to the search for high reliability results it was necessary to establish an efficient meshed and, consequently, with a proper number of nodes and elements. However, a comparative analysis was carried out between a variety of meshes with different qualities and number of elements, as shown in Table 4, to verify the efficiency of the meshed in this work; as a result, the mesh 1 model was taken with the excellent ratings of quality previously pointed out.
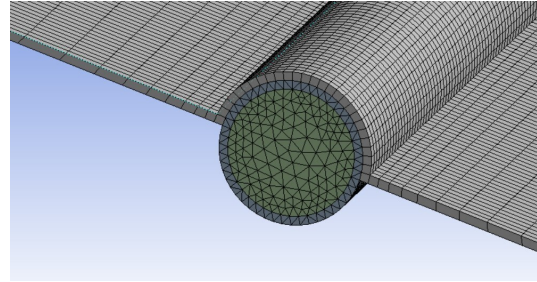

Figure 5. Mesh of the solar collector

Table 4. Types of meshes

Mesh	Number of elements	Skewness average
1	2272823	0.23763
2	149286	0.32162
3	92901	0.42708
4	192792	0.30576
5	247324	0.27664

With the help of the mesh quality, it can be seen in Figure 6 the different types of trends generated by the variability of results of the CFD simulation, which leads to the final selection of a particular meshed.
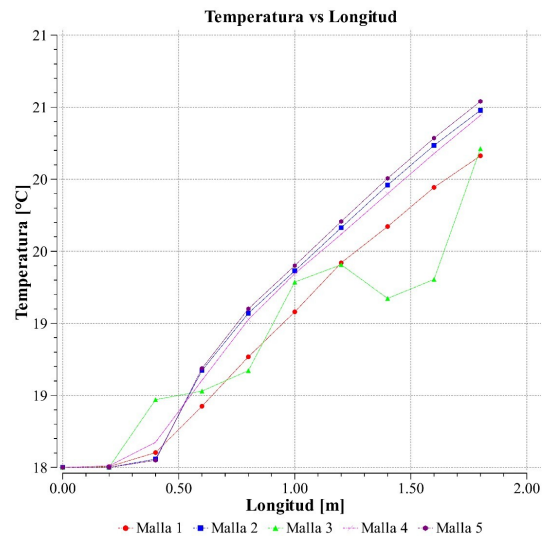
Figure 6. Variation of results with different meshed

To model the dynamic fluids, the CFD simulation software employs the Navier-Stokes equations, which

take into account the continuity, momentum and energy conservation, as shown in Equations (6), (7) and (8), respectively [29].

$$\frac{\partial \rho}{\partial t} + \nabla \cdot (\rho \vec{v}) = S_m \qquad (6)$$

$$\frac{\partial \rho}{\partial t}(\rho \vec{v}) + \nabla \cdot (\rho \vec{v} \vec{v}) = \nabla p + \nabla \cdot \left[\mu \times (\nabla \vec{v} + \nabla \vec{v}^T)\right] +$$
$$+ \rho \vec{g} + \vec{F}$$
$$(7)$$

$$\frac{\partial \rho}{\partial t}(\rho E) + \nabla \cdot [\vec{v} \cdot (\rho E + p)] = \nabla \cdot (k_{eff} \cdot \nabla T) + S_h \quad (8)$$

When carrying out the validation of the CFD simulation results, it is important to know the permissible range of the variation that such results may exhibit with respect to the experimental values of the same study; this range can be measured with the percentage error presented in Equation 9, and according to different authors the maximum permissible value is 5.2 % [30].

$$Error \% = \frac{|X_{sim} - X_{exp}|}{X_{sim}} \qquad (9)$$

3. Results and discussion

The radiation module of the CFD simulation software, solar calculator, enabled the analysis of the flat plate solar collector with parameters of latitude (–0.225219), longitude (–78.5248) and different hours to determine parameters such as surface temperature of the heat transfer device, as shown in Figure 7 (a and b) with hours from 11:00 to 12:00, respectively, where it is possible to observe a greater temperature distribution due to the radiation peak existing at 12:00 with a maximum value of 27.12 °C; this temperature attenuates as time goes on as it is indicated by a smaller value of 24.63 °C on the wing surface at 13:00.

The radiation striking on the collector is directly related with the hours at which the test is conducted, as can be observed in Figure 8 (a and b), generating peak values between 12:00 and 13:15 with available radiation values between 650 and 800 W·m^{-2}, respectively, influencing in a similar manner on the ambient temperature, a very important parameter in the heat transfer to the device and in its performance.
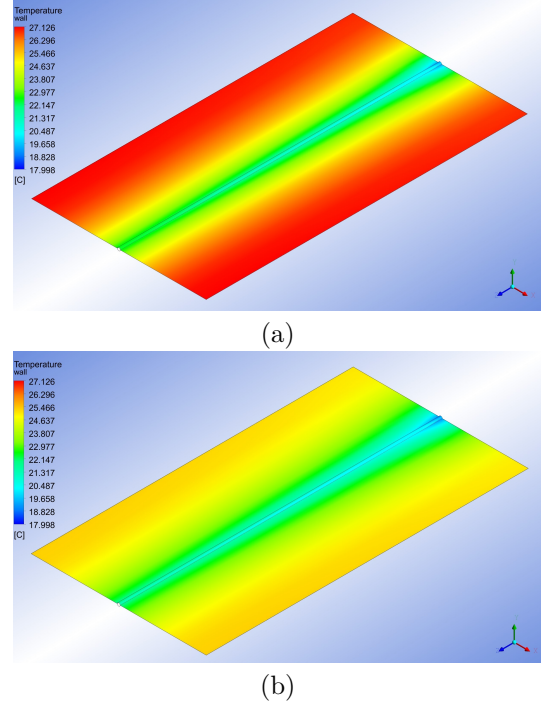

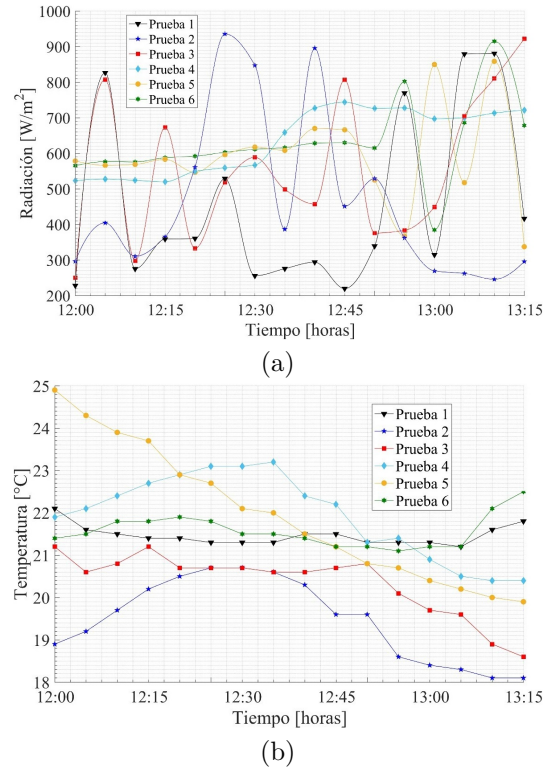**Figure 7.** Temperature in the external wall of the solar collector

Figure 8. Variation of a) Radiation, b) Temperature

Due to the common variations of the radiation levels that fluctuate between 350 and 800 W·m^{-2} in the zone with the previously established latitude and longitude, along with the temperature and heat flow

change on the surface of the heat transfer device, it is possible to observe a greater temperature at the center of the working fluid along the center of the tube in the solar collector at specific times, as illustrated in Figure 9, and due to this it is determined that the largest temperature at the outlet of the collector will occur at 12:00 with a value of 20.2 °C and with the smallest value of 18.65 °C at 10:00 when going across the total length of the flat plate heat exchanger.
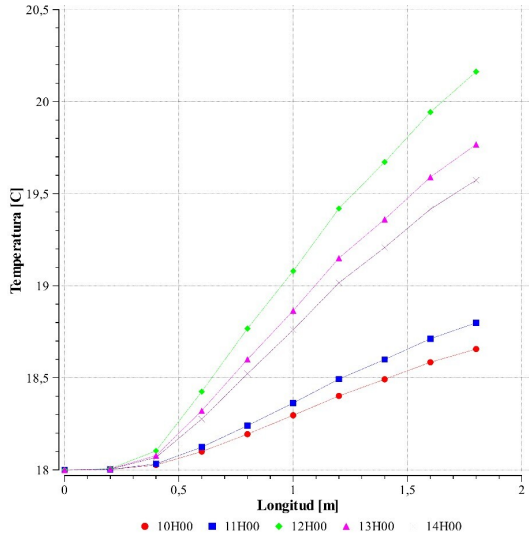

Figure 9. Comparative diagram of temperature vs. length at the center of the collector

It is possible to observe a greater temperature increase as the fluid approaches the tube wall in the heat exchanger, as it is appreciated in Figure 10(a), where the temperature is measured along the solar collector in an intermediate space between the wall and the center of the tube, and additionally Figure 10(b) illustrates the temperature variation in the collector wall.
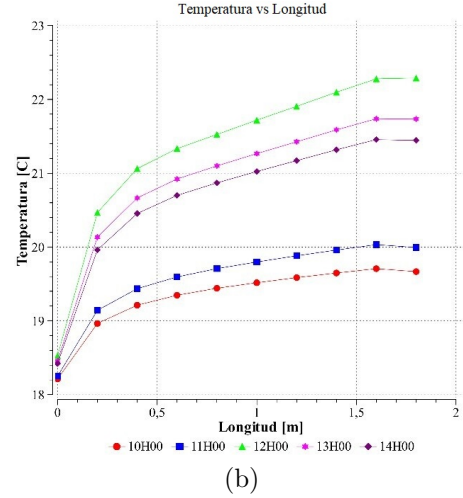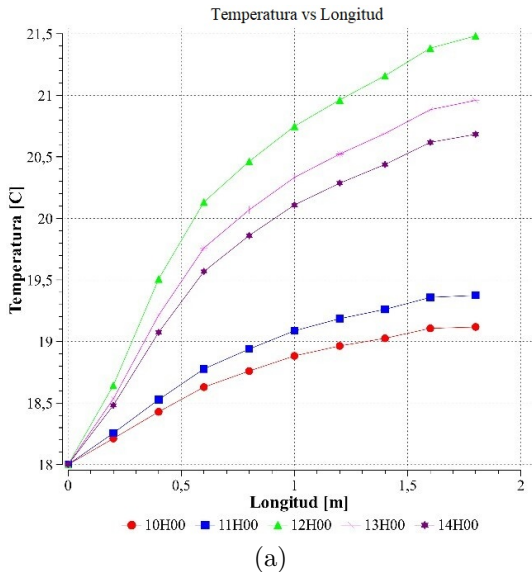

(a)

(b)

Figure 10. Comparative diagrams of temperature *vs.* length at a) ¼ of the surface, b) surface

The results of the CFD simulation presented in Figure 9 show the same trend that the experimental results, as can be observed in Figure 11, validating the results within an error margin of 4.01 % in the analysis at the center of the solar collector at the different hours.
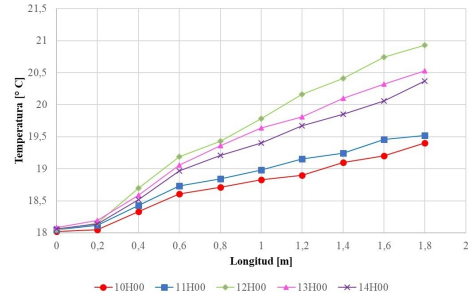

Figure 11. Comparative diagrams of temperature *vs.* length with experimental results

When carrying out the comparative analysis between the experimental results and the results of the numerical simulation, it is possible to find a similar trend in both cases as shown in Figure 12. Similarly, it is possible to appreciate a maximum percentage error of 4.01 %, thus validating the experimental and simulation data.
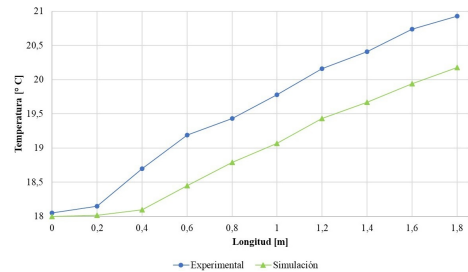

Figure 12. Comparative diagram in the experimental and numerical analysis at 12:00

4. Conclusions

In the present study an analysis of the performance of a flat plate solar collector was performed by means of a CFD simulation software, where the solar radiation at different hours has been utilized in several simulations carried out; such radiation directly influences the transfer of thermal energy to the working fluid, showing various results.

The maximum value of fluid temperature at the outlet of the solar collector is 20.16 °C at 12:00, while the smallest fluid temperature at the outlet was obtained at 10:00 with 18.65 °C, due to the low solar radiation at that time; these values represent a favorable trend for the utilization of the fluid in different processes, all this without ruling out the use of independent fluid heating processes to reach a specific temperature in the search for fulfilling a particular need.

The radiation peak occurring at 12:00 generates a maximum heat flow of 96.02 W·m^{-2} to the working fluid, thus achieving the maximum amount of energy transfer in all the analysis range considered in the research. It is possible to appreciate a temperature variation on the external surface of the heat transfer device in accordance with the typical radiation levels at the different hours under study, obtaining a maximum value of 27.12 °C and a minimum value of 20.48 °C at 12:00 and 10:00, respectively. At last, it can be verified that the simulation and experimental data differ 4.01 % when compared to each other.

Acknowledgment

References

[1] L. Evangelisti, R. D. L. Vollaro], and F. Asdrubali, "Latest advances on solar thermal collectors: A comprehensive review," *Renewable and Sustainable Energy Reviews*, vol. 114, p. 109318, 2019. [Online]. Available: https://doi.org/10.1016/j.rser.2019.109318

[2] J. Calle-Sigüencia and O. Tinoco-Gómez, "Obtención de ACS con energía solar en el cantón Cuenca y análisis de la contaminación ambiental," *Ingenius*, no. 19, pp. 89–101, 2018. [Online]. Available: https://doi.org/10.17163/ings.n19.2018.09

[3] L. M. Ayompe and A. Duffy, "Analysis of the thermal performance of a solar water heating system with flat plate collectors in a temperate climate," *Applied Thermal Engineering*, vol. 58, no. 1, pp. 447–454, 2013. [Online]. Available: https://doi.org/10.1016/j.applthermaleng.2013.04.06

[4] W. M. Hashim, A. T. Shomran, H. A. Jurmut, T. S. Gaaz, A. A. H. Kadhum, and A. A. Al-Amiery, "Case study on solar water heating for flat plate collector," *Case Studies in Thermal Engineering*, vol. 12, pp. 666–671, 2018. [Online]. Available: https://doi.org/10.1016/j.csite.2018.09.002

[5] E. Arteaga-López, C. Ángeles-Camacho, and F. Bañuelos-Ruedas, "Advanced methodology for feasibility studies on building-mounted wind turbines installation in urban environment: Applying CFD analysis," *Energy*, vol. 167, pp. 181–188, 2019. [Online]. Available: https://doi.org/10.1016/j.energy.2018.10.191

[6] A. Marroquín-De Jesús, J. M. Olivares-Ramírez, O. Jiménez-Sandoval, M. A. Zamora-Antuñano, and A. Encinas-Oropesa, "Analysis of flow and heat transfer in a flat solar collector with rectangular and cylindrical geometry using CFD," *Ingeniería, Investigación y Tecnología*, vol. 14, no. 4, pp. 553–561, 2013. [Online]. Available: https://doi.org/10.1016/S1405-7743(13)72265-0

[7] E. Mohamed, S. Riffat, S. Omer, and R. Zeinelabdein, "A comprehensive investigation of using mutual air and water heating in multi-functional dx-samhp for moderate cold climate," *Renewable Energy*, vol. 130, pp. 582–600, 2019. [Online]. Available: https://doi.org/10.1016/j.renene.2018.06.075

[8] W. M. Duarte, T. F. Paulino, J. J. G. Pabón, S. Sawalha, and L. Machado, "Refrigerants selection for a direct expansion solar assisted heat pump for domestic hot water," *Solar Energy*, vol. 184, pp. 527–538, 2019. [Online]. Available: https://doi.org/10.1016/j.solener.2019.04.027

[9] A. X. Andrade Cando, W. Quitiaquez Sarzosa, and L. F. Toapanta, "CFD analysis of a solar flat plate collector with different cross sections," *Enfoque UTE,*, vol. 11, no. 2, pp. 95–108, 2020. [Online]. Available: https://doi.org/10.29019/enfoque.v11n2.601

[10] W. Ji, J. Cai, J. Ji, and W. Huang, "Experimental study of a direct expansion solar-assisted heat pump (dx-sahp) with finned-tube evaporator and comparison with conventional dx-sahp," *Energy and Buildings*, vol. 207, p. 109632, 2020. [Online]. Available: https://doi.org/10.1016/j.enbuild.2019.109632

[11] H. Fathabadi, "Novel low-cost parabolic trough solar collector with tpct heat pipe and solar tracker: Performance and comparing with commercial flat-plate and evacuated tube solar collectors," *Solar Energy*, vol. 195, pp. 210–222, 2020. [Online]. Available: https://doi.org/10.1016/j.solener.2019.11.057

[12] S. N. Rabelo, T. de F. Paulino, W. M. Duarte, S. Sawalha, and L. Machado, "Experimental analysis of the influence of water mass flow rate on the performance of a co2 direct-expansion solar assisted heat pump," *International Journal of Chemical and Molecular Engineering*, vol. 12, no. 7, pp. 327–331, 2018. [Online]. Available: https://doi.org/10.5281/zenodo.1317384

[13] X. Kong, P. Sun, S. Dong, K. Jiang, and Y. Li, "Experimental performance analysis of a direct-expansion solar-assisted heat pump water heater with r134a in summer," *International Journal of Refrigeration*, vol. 91, pp. 12–19, 2018. [Online]. Available: https://doi.org/10.1016/j.ijrefrig.2018.04.021

[14] J. Lee and T.-H. Song, "Conduction/radiation combined heat transfer with contact resistance for application to vacuum insulation," *International Journal of Heat and Mass Transfer*, vol. 129, pp. 380–388, 2019. [Online]. Available: https://doi.org/10.1016/j.ijheatmasstransfer.2018.09.085

[15] F. Jiang, Z. Li, Q. Zhao, Q. Tao, S. Lu, and K. Zhao, "The influence of exterior louver blinds' geometric and thermal attributes on the convective heat transfer at building facades," *Solar Energy*, vol. 193, pp. 654–665, 2019. [Online]. Available: https://doi.org/10.1016/j.solener.2019.09.074

[16] Y. Zhang, J. Wang, W. Liu, and Z. Liu, "Heat transfer and pressure drop characteristics of r134a flow boiling in the parallel/tandem microchannel heat sinks," *Energy Conversion and Management*, vol. 148, pp. 1082–1095, 2017. [Online]. Available: https://doi.org/10.1016/j.enconman.2017.06.067

[17] J. P. Meyer and M. Everts, "Chapter three - a review of the recent developments in laminar, transitional, quasi-turbulent and turbulent forced and mixed convective flow through horizontal tubes," in *Advances in Heat Transfer*, ser. Advances in Heat Transfer, E. M. Sparrow, J. P. Abraham, J. M. Gorman, and W. Minkowycz, Eds. Elsevier, 2019, vol. 51, pp. 131–205. [Online]. Available: https://doi.org/10.1016/bs.aiht.2019.07.001

[18] S. MOJUMDER, S. A. H. A. Sourav, S. A. H. A. Sumon, and M. A. H. MAMUN, "Combined effect of reynolds and grashof numbers on mixed convection in a lid-driven t-shaped cavity filled with water-al2o3 nanofluid," *Journal of Hydrodynamics, Ser. B*, vol. 27, no. 5, pp. 782–794, 2015. [Online]. Available: https://doi.org/10.1016/S1001-6058(15)60540-6

[19] P. Sánchez-Palencia, N. Martín-Chivelet, and F. Chenlo, "Modelización del coeficiente de transmitancia térmica de módulos fotovoltaicos para integración en edificios," in *XVI Congreso Ibérico y XII Congreso Iberoamericano de Energía Solar*, 2018. [Online]. Available: https://bit.ly/2C4petH

[20] N. Rahbar, J. A. Esfahani, and E. Fotouhi-Bafghi, "Estimation of convective heat transfer coefficient and water-productivity in a tubular solar still - CFD simulation and theoretical analysis," *Solar Energy*, vol. 113, pp. 313–323, 2015. [Online]. Available: https://doi.org/10.1016/j.solener.2014.12.032

[21] C.-H. Wang, Y.-Y. Feng, K. Yue, and X.-X. Zhang, "Discontinuous finite element method for combined radiation-conduction heat transfer in participating media," *International Communications in Heat and Mass Transfer*, vol. 108, p. 104287, 2019. [Online]. Available: https://doi.org/10.1016/j.icheatmasstransfer.2019.104287

[22] B. P. Jelle, S. E. Kalnes, and T. Gao, "Low-emissivity materials for building applications: A state-of-the-art review and future research perspectives," *Energy and Buildings*, vol. 96, pp. 329–356, 2015. [Online]. Available: https://doi.org/10.1016/j.enbuild.2015.03.024

[23] A. J. Cetina-Quiñones, A. Bassam, G. Hernández-Chan, I. Hernández Benítez, J. Hernández Reyes, and D. Lugo Chávez, "Modelación térmica de un colector solar de canal parabólico mediante el método de elementos finitos," *Ingeniería*, vol. 21, no. 1, pp. 1–12, 2017. [Online]. Available: https://bit.ly/2MYMg7D

[24] W. Pang, Y. Cui, Q. Zhang, G. J. Wilson, and H. Yan, "A comparative analysis on performances of flat plate photovoltaic/thermal collectors in view of operating media, structural designs, and climate conditions," *Renewable and Sustainable Energy Reviews*, vol. 119, p. 109599, 2020. [Online]. Available: https://doi.org/10.1016/j.rser.2019.109599

[25] I. Vişa, M. Moldovan, and A. Duţă, "Novel triangle flat plate solar thermal collector for facades integration," *Renewable Energy*, vol. 143, pp. 252–262, 2019. [Online]. Available: https://bit.ly/30Jsxkr

[26] D. H. Lobón, E. Baglietto, L. Valenzuela, and E. Zarza, "Modeling direct steam generation in solar collectors with multiphase CFD," *Applied Energy*, vol. 113, pp. 1338–1348, 2014. [Online]. Available: https://doi.org/10.1016/j.apenergy.2013.08.046

[27] A. Aghagoli and M. Sorin, "Thermodynamic performance of a CO_2 vortex tube based on 3d CFD flow analysis," *International Journal of Refrigeration*, vol. 108, pp. 124–137, 2019. [Online]. Available: https://doi.org/10.1016/j.ijrefrig.2019.08.022

[28] Z. Badiei, M. Eslami, and K. Jafarpur, "Performance improvements in solar flat plate collectors by integrating with phase change materials and fins: A CFD modeling," *Energy*, vol. 192, p. 116719, 2020. [Online]. Available: https://doi.org/10.1016/j.energy.2019.116719

[29] L. Zhou, Y. Wang, and Q. Huang, "CFD investigation of a new flat plate collector with additional front side transparent insulation for use in cold regions," *Renewable Energy*, vol. 138, pp. 754–763, 2019. [Online]. Available: https://doi.org/10.1016/j.renene.2019.02.014

[30] D. G. Gunjo, P. Mahanta, and P. S. Robi, "CFD and experimental investigation of flat plate solar water heating system under steady state condition," *Renewable Energy*, vol. 106, pp. 24–36, 2017. [Online]. Available: https://doi.org/10.1016/j.renene.2016.12.041

Guidelines for publication in Ingenius Journal

1. General Information

INGENIUS is a scientific publication of the *Universidad Politécnica Salesiana* of Ecuador, published since January 2007, with a fixed biannual periodicity, specialized in Mechanical Engineering, Electrical Engineering, Electronics, Computer Science and its integration in what is now known as Mechatronics; these lines of action strengthen areas such as automation, control, robotics, among others..

It is a scientific journal, which uses the peer-review system, under double-blind review methodology, according to the publication standards of the Institute of Electrical and Electronics Engineers (IEEE). Compliance with this system allows authors to guarantee an objective, impartial and transparent review process, which facilitates the publication of their inclusion in reference databases, repositories and international indexing.

INGENIUS is indexed in the directory and selective catalog of the Regional Online Information System for Scientific Journals of Latin America, the Caribbean, Spain and Portugal (Latindex), in the Directory of Journals of Open Access DOAJ, In the Information Matrix for the Analysis of Journals, MIAR, In the Ibero-American Network of Innovation and Scientific Knowledge, REDIB and in repositories, libraries and specialized catalogs of Latin America.

The journal is published in a double version: printed (ISSN: 1390-650X) and digital (e-ISSN: 1390-860X), in Spanish, each work being identified with a DOI (Digital Object Identifier System. The articles sent to INGENIUS magazine must comply with the following criteria:

2. Scope and policy

2.1. Theme

Original contributions in Mechanical Engineering, Electrical and Electronic Engineering, Computer Science and its integration in what is now known as Mechatronics, as well as related areas: Automation, Control, Domotics, Robotics in their different fields of action and all those related disciplines with the same central theme.

All the work carried out by national or foreign researchers may be published once they meet the required scientific quality criteria.

2.2. Contributions

INGENIUS Journal preferably publishes articles related to empirical research, and also reports of technological development, proposals for models and innovations, products for the elaboration of graduate and postgraduate thesis that contribute to the field of science and technology, as well as select revisions of literature. (state-of-the-art).

- **Research:** 5,000 to 6,500 words of text, including title, abstracts, descriptors, charts and references.
- **Reports:** 5,000 to 6,500 words of text, including title, abstracts, charts and references.
- **Reviews:** 6,000 to 7,000 words of text, including charts and references. Current, selective and justified references, would be specially valued from among 40 works

The INGENIUS Journal publishes original and unpublished works written in Spanish and English, they may not have been published

through any printed or electronic media, nor be in the process of arbitration or publication.

Every article will be subjected to a rigorous arbitration process; the evaluation of the article will be made according to criteria of originality, relevance, relevance, contributions, scientific rigor and compliance with established editorial guidelines.

Being an arbitrated publication, the Editorial Board approves its publication based on the concept of specialized pairs. The reception of a document does not imply commitment of publication.

It is essential to present a letter of presentation and grant of rights which can be downloaded from: < urlhttps://goo.gl/ZNkMRD>.

Contributions must be exclusively sent and through the OJS (Open Journal Sys-tem) <https://goo.gl/JF7dWT>. In which all authors must previously register as a user. For any consultation of the procedure you should contact:

<revistaingenius@ups.edu.ec>,
<jcalle@ups.edu.ec> ó
<mquinde@ups.edu.ec>.

3. Presentation and structure of the manuscripts

For those works that are empirical investigations, the manuscripts will follow the IMRDC structure (Introduction, Materials and Methods, Results and Discussion and Conclusions), being optional the Notes and Supports. Those papers that, on the contrary, deal with reports, studies, proposals and reviews may be more flexible in their epigraphs, particularly in material and methods, analysis, results, discussion and conclusions. In all typologies of works, references are mandatory.

Articles may be written on Microsoft Word (.doc or .docx) or LATEX(.tex). The template to

be used can be downloaded from the journal's website, a, <https://goo.gl/gtCg6m>, while for LATEX in <https://goo.gl/hrHzzQ>, it is necessary that the file be anonymised in Properties of File, so that the author(s) ID is not displayed.

Figures, Graphs and/or Illustrations, as well as Charts shall be numbered sequentially including an explanatory description for each. The equations included in the article must also be numbered; the figures, charts and equations must be cited in the text.

Use space after point, commas and question marks.

Use "enter" at the end of each paragraph and title heading. Do not use .ᵉⁿter.ᵃnywhere else, let the word processor program automatically break the lines.

Do not center headings or subheadings as they should be aligned to the left.

Charts must be created in the same program used for the document body, but must be stored in a separate file. Use tabs, not spaces, to create columns. Remember that the final size of printed pages will be 21 x 28 cm, so the tables must be designed to fit the final print space.

3.1.   Structure of the manuscripts

3.1.1. Presentation and cover letter

1. **Título (español) / Title (inglés):** Concise but informative, in Spanish on the front line and in English on the second, when the article is written in Spanish and vice versa if it is written in English.

2. **Authors and affiliations:** Full name and surname of each author, organized by order of priority and their institutional affiliation with reference to the end of the first sheet, where it must include:

Dependency to which belongs within the institution, Institution to which he/she belongs, country, ORCID. A maximum of 5 authors will be accepted, although there may be exceptions justified by the complexity and extent of the topic.

3. **Abstract (Spanish) / Abstract (English):** It will have a maximum extension of 230 words, first in Spanish and then in English. : 1) Justification of the topic; 2) Objectives; 3) Methodology and sample; 4) Main results; 5) Main conclusions.

4. **Keywords (Spanish) / Keywords (English):** 6 descriptors must be presented for each language version directly related to the subject of the work. The use of the key words set out in UNESCO's Thesaurus will be positively valued.

5. **Presentation (Cover Letter):** A statement that the manuscript is an original contribution, not submission or evaluation process in another journal, with the confirmation of the signatory authors, acceptance (if applicable) of formal changes in the manuscript according to the guidelines and partial assignment of rights to the publisher, according to the format established in: <https://goo.gl/ZNkMRD>

3.1.2. Manuscript

1. **Título (español) / Title (inglés):** Concise but informative, in Spanish on the front line and in English on the second, when the article is written in Spanish and vice versa if it is written in English.

2. **Authors and affiliations:** Full name and surname of each author, organized by order of priority and their institutional affiliation with reference to the end of the first sheet, where it must include: Dependency to which belongs within the institution, Institution to which he/she

belongs, country, ORCID. A maximum of 5 authors will be accepted, although there may be exceptions justified by the complexity and extent of the topic.

3. **Abstract (Spanish) / Abstract (English):** It will have a maximum extension of 230 words, first in Spanish and then in English. : 1) Justification of the topic; 2) Objectives; 3) Methodology and sample; 4) Main results; 5) Main conclusions.

4. **Keywords (Spanish) / Keywords (English):** 6 descriptors must be presented for each language version directly related to the subject of the work. The use of the key words set out in UNESCO's Thesaurus will be positively valued.

5. **Introduction:** It should include the problem statement, context of the problem, justification, rationale and purpose of the study, using bibliographical citations, as well as the most significant and current literature on the topic at national and international level.

6. **Material and methods:** It must be written so that the reader can easily understand the development of the research. If applicable, it will describe the methodology, the sample and the form of sampling, as well as the type of statistical analysis used. If it is an original methodology, it is necessary to explain the reasons that led to its use and to describe its possible limitations.

7. **Analysis and results:** It will try to highlight the most important observations, describing, without making value judgments, the material and methods used. They will appear in a logical sequence in the text and the essential charts and figures avoiding the duplication of data.

8. **Discussion and Conclusions:** It will summarize the most important findings,

relating the observations themselves to relevant studies, indicating contributions and limitations, without adding data already mentioned in other sections. It should also include deductions and lines for future research.

9. **Supports and acknowledgments (optional):** The Council Science Editors recommends the author (s) to specify the source of funding for the research. Priority will be given to projects supported by national and international competitive projects.

10. **The notes (optional):** will go, only if necessary, at the end of the article (before the references). They must be manually annotated, since the system of footnotes or the end of Word is not recognized by the layout systems. The numbers of notes are placed in superscript, both in the text and in the final note. The numbers of notes are placed in superscript, both in the text and in the final note. No notes are allowed that collect simple bibliographic citations (without comments), as these should go in the references.

11. **References:** Bibliographical citations should be reviewed in the form of references to the text. Under no circumstances should references mentioned in the text not be included. Their number should be sufficient to contextualize the theoretical framework with current and important criteria. They will be presented sequentially in order of appearance, as appropriate following the format of the IEEE.

3.2. Guidelines for Bibliographical references

Journal articles:

[1] J. Riess, J. J. Abbas, "Adaptive control of cyclic movements as muscles fatigue using functional neuromuscular stimulation". IEEE Trans. Neural Syst. Rehabil. Eng vol. 9, pp.326–330, 2001. [Onine]. Available: https://doi.org/10.1109/7333.948462

Books:

[1] G. O. Young, "Synthetic structure of industrial plastics" in Plastics, 2nd ed., vol. 3, J. Peters, Ed. New York: McGraw–Hill, 1964, pp. 15–64.

Technical reports:

[1] M. A. Brusberg and E. N. Clark, "Installation, operation, and data evaluation of an oblique–incidence ionosphere sounder system," in "Radio Propagation Characteristics of the Washington–Honolulu Path," Stanford Res. Inst., Stanford, CA, Contract NOBSR–87615, Final Rep., Feb. 1995, vol. 1

Articles presented in confeences (unpubished):

[1] Vázquez, Rolando, Presentación curso "Realidad Virtual". National Instruments. Colombia, 2009.

Articles of memories of Conferences (Published):

[1] L. I. Ruiz, A. García, J. García, G. Taboada. "Criterios para la optimización de sistemas eléctricos en refinerías de la industria petrolera: influencia y análisis en el equipo eléctrico," IEEE CONCAPAN XXVIII, Guatemala 2008.

Thesis:

[1] L.M. Moreno, "Computación paralela y entornos heterogéneos," Tesis doctoral, Dep. Estadística, Investigación Operativa y Computación, Universidad de La Laguna, La Laguna, 2005.

Guidelines:

[1] IEEE Guide for Application of Power Apparatus Bushings, IEEE Standard C57.19.100–1995, Aug. 1995.

Patents:

[1] J. P. Wilkinson, "Nonlinear resonant cir-

cuit devices," U.S. Patent 3 624 125, July 16, 1990.

Manuals:

[1] Motorola Semiconductor Data Manual, Motorola Semiconductor Products Inc., Phoenix, AZ, 1989.

Internet resources:

[1] E. H. Miller, "A note on reflector arrays" [Online]. Available. https://goo.gl/4cJkCF

3.3. Epigraphs, Figures and Charts

The epigraphs of the body of the article will be numbered in Arabic. They should go without a full box of capital letters, neither underlined nor bold. The numbering must be a maximum of three levels: 1. / 1.1. / 1.1.1. At the end of each numbered epigraph will be given an enter to continue with the corresponding paragraph.

The charts must be included in the text according to order of appearance, numbered in Arabic and subtitled with the description of the content, the subtitle should go at the top of the table justified to the left.

Figures can be linear drawings, maps or black and white halftone or color photographs in 300 dpi resolution. Do not combine photographs and line drawings in the same figure.

Design the figures so that they fit eventually to the final size of the journal 21 x 28 cm. Make sure inscriptions or details, as well as lines, are of appropriate size and thickness so that they are not illegible when they are reduced to their final size (numbers, letters and symbols must be reduced to at least 2.5 mm in height After the illustrations have been reduced to fit the printed page). Ideally, the linear illustrations should be prepared at about a quarter of their final publication size.

Different elements in the same figure should be spelled a, b, c, etc.

Photographs should be recorded with high contrast and high resolution. Remember that photographs frequently lose contrast in the printing process. Line drawings and maps should be prepared in black.

The text of the figures and maps must be written in easily legible letters.

If the figures have been previously used, it is the responsibility of the author to obtain the corresponding permission to avoid subsequent problems related to copyright.

Each figure must be submitted in a separate file, either as bitmap (.jpg, .bmp, .gif, or .png) or as vector graphics (.ps, .eps, .pdf).

4. Submission process

The manuscript must be sent through the OJS system of the journal, <`https://goo.gl/JF7dWT`>,the manuscript should be uploaded as an original file in .pdf without author data and anonymized according to the above; In complementary files the complete manuscript must be loaded in .doc or .docx (Word file), that is to say with the data of the author (s) and its institutional ascription; Also the numbered figures should be uploaded in independent files according to the corresponding in the manuscript (as bitmap .jpg, .bmp, .gif, or .png or as vector graphics .ps, .eps, .pdf). It is also obligatory to upload the cover letter and grant of rights as an additional file.

All authors must enter the required information on the OJS platform and only one of the authors will be responsible for correspondence.

Once the contribution has been sent the system will automatically send the author for correspondence a confirmation email of receipt of the contribution.

5. Editorial process

Once the manuscript has been received in OJS, a first check by the editorial team of the following points:

- The topic is in accordance with the criteria of the journal.
- Must have the IMRDC structure.
- Must be in the INGENIUS format.
- Must use the IEEE citation format.
- All references should be cited in the text of the manuscript as well as charts, figures and equations.
- The manuscript is original; for this, software is used to determine plagiarism.

The assessment described above can take up to 4 weeks.

If any of the above is not complete or there is inconsistency, an email will be sent to the author to make the requested corrections.

The author will make the corrections and resend the contribution through an email in response to the notification and will also upload the corrected manuscript into OJS supplementary files.

The editorial team will verify that the requested corrections have been incorporated, if it complies, the manuscript will start the second part of the process that may be followed by the author through OJS, otherwise the author will be notified and the manuscript will be archived.

The second phase of the process consists of the evaluation under the methodology of double-blind review, which includes national and foreign experts considering the following steps:

- The editor assigns two or more reviewers for the article.
- After reviewing the article, the reviewers will submit the evaluation report with one of the following results.
  - Publishable
  - Publishable with suggested changes
  - Publishable with mandatory changes
  - Non publishable
- The editor once received the evaluation by the reviewers will analyze the results and determine if the article is accepted or denied.
- If the article is accepted, the author will be notified to make corrections if required and the corresponding editorial process will be continued.
- If the article is denied, the author will be notified and the manuscript will be archived.
- In the two previous cases the result of the evaluation of the reviewers and their respective recommendations will be sent.

The second phase of the process lasts at least 4 weeks, after which they will be notified to the author giving instructions to continue with the process.

6. Publication

The INGENIUS Journal publishes two issues per year, on January 1st and July 1st, so it is important to consider the dates for sending the articles and their corresponding publication. Articles received until October will be considered for the January publication and those received until April for the July publication.

OTHER PERIODIC PUBLICATIONS OF THE UNIVERSITY

UNIVERSITAS, Journal of Social and Human Sciences.

LA GRANJA, Journal of Life Sciences.

ALTERIDAD, Journal of Education.

RETOS Journal of Administration Sciences and Economics.

UTOPÍA, University Youth Ministry Magazine.

SOPHIA, Collection of Philosophy of Education.